Numerical Modeling of Extreme Hydrodynamic Loading and Pneumatic Long Wave Generation: Application of a Multiphase Fluid Model

Steven Douglas

A thesis submitted to the
Faculty of Graduate and Postdoctoral Studies
in partial fulfillment of the requirements for the degree of
Master of Applied Science in Civil Engineering

University of Ottawa, Canada
Department of Civil Engineering

January 2016

Abstract

In this study, a three-dimensional two-phase (air and water) numerical solver is applied to investigate free surface flows. The first component aims to improve the overall understanding of the underlying physical mechanisms that occur during the interaction between turbulent hydraulic bores and simple structures. Data collected during large-scale physical experiments based on generating dam-break waves in a horizontal rectangular channel is used for comparing to the numerical results. An extensive sensitivity analysis on numerical parameters including spatial discretization and turbulence models is presented. Quantitative comparisons of numerical and experimental time series of water surface elevations, pressure, and net streamwise force exerted on the structure are used to validate the model. In the in-depth analysis, it is demonstrated that the model is able to simulate the pertinent aspects of the flow behaviour that occur during the interaction with good agreement. The numerical impulsive force generated at initial impact shows excellent agreement with the experimental results, particularly for the larger magnitudes bores considered. Since the numerical model treats the air as an incompressible media, the level of agreement observed between the experimental and numerical results suggests that the compressibility of the air in the leading edge of the bore during the physical testing had no significant effect on the measured impulsive force. The two-phase model was also able to capture the occurrence of a second transient spike in the force exerted on the structure when the initial runup collapsed back onto the incoming flow, trapping a pocket of air in the process. The model was further applied to investigate the effect of an initially quiescent layer of water in the downstream channel section on bore propagation characteristics and the subsequent interaction with the structure. It is demonstrated that for small nonzero values of initial downstream depth a substantial increase in bore depth occurs. However, further increases in the downstream depth did not appear have any significant effects. For the greatest downstream depth simulated, a considerable reduction in the hydrodynamic force is observed as a result of a more rapid closing of the wake that develops on the leeside of the structure.

The second component of the study applies the same numerical solver to investigate a novel long wave generation technique for producing laboratory-scale tsunami waves. The concept is based on removing the air from the inside of a tank with a submerged outlet at the upstream end of the basin and releasing the water in a controlled manner. A similar procedure as described above was used to calibrate the numerical parameters to experimentally-measured wave heights and periods. To model the influence of the pneumatic valves mounted on top of the upstream chamber, time-varying pressure boundary conditions are developed to regulate and control the pressure inside the tank. Quantitative and qualitative comparisons of the numerical and experimental results show good agreement and a high potential for the solver to be used for similar investigations. An analysis is performed to improve the existing understanding of the wave formation process. The model is also applied to modify test configurations that influence the waveform for which the results may be used to aid in making operating decisions for future tests or in the design of similar wave generating devices.

Acknowledgements

My utmost appreciation goes out to my academic supervisor, Dr. Ioan Nistor, for his unbelievable amount of support that he has shown since day one. His willingness to advance the interest of his own students, even when it goes against his own, shows a level of selflessness which is difficult for me to express my admiration for in words.

Over the course of completing this work, I had an incredible and unique opportunity to complete two internships at the Oceans, Coastal, and River Engineering Laboratory at the National Research Council of Canada (NRC-OCRE). There, the numerical modeling knowledge I had been gaining while completing my Master's was augmented with a once-in-a-life-time chance to help build and operate large-scale physical models for coastal processes. I would also like to extend my thanks to everyone I came into contact with there, most notably, Paul Knox, Scott Baker, Dr. Andrew Cornett, Nathalie Brunette, John Marquardt, Alistair Rayner, David Hnatiw, and Yvan Brunet for sharing their immense knowledge and making that experience possible.

Lastly, I wish to express my gratitude to my family back home and abroad. My parents, whom with their material and moral support over the years ultimately made this effort possible. My sister, whose dedication and work ethic has spilled over and inspired me to take my studies as far as I have. And finally, my brother, who out of all people understands me the most and has made my experience here vastly more enjoyable. Combined, they have helped foster my passion for the pursuit of knowledge and, for that, I am forever indebted.

Table of Contents

List of Figures

List of Tables

List of Symbols

Latin Characters

Symbol	Description	Unit
C_α	compression coefficient	-
Co	Courant number	-
d	distance	m
f	Darcy-Weisbach friction factor	-
F	mass fluid flux	kg/s
g	acceleration due to gravity	m/s^2
h_u	upstream depth	m
k	turbulent kinetic energy	m^2/s^2
$\boldsymbol{n}$	unit normal vector	-
p	pressure	Pa
p^*	modified pressure	Pa
$\boldsymbol{S_f}$	cell-face surface-normal vector	m^2
$\mathbf{d}$	distance vector	m
t	time	seconds
U^*	dimensional wave front celerity	-
$\mathbf{U}$	velocity vector	m
$\mathbf{U_c}$	compression velocity vector	m/s
V	volume	m^3
X_s^*	dimensional location of wave front	-
$\boldsymbol{x}$	position vector	m
x	x-component of position vector	m
y	y-component of position vector	m
z	z-component of position vector	m

Greek Characters

Symbol	Description	Unit
α	phase fraction	-
ϵ	turbulent dissipation	m^2/s^3
κ	curvature	1/m
λ	Damping coefficient	-
ρ	density	Kg/m^3
ϕ	Generalized conservative physical quanitity	-
Γ	diffusivity	-
σ	surface tension coefficient	N/m
$\boldsymbol{\tau}$	Stress tensor	Pa
μ_{eff}	effective dynamic viscosity	Ns/m^2
μ_t	turbulent dynamic viscosity	Ns/m^2
μ	dynamic viscosity	Ns/m^2
ω	specific turbulent dissipation	m^2/s^3

Superscripts and Subscripts

Symbol	Description
a	fluid 1
b	fluid 2
$'$	at the interface
T	transpose
n	next (new) time step
o	previous (old) time step
f	at the cell face

Mathematical Operators

Symbol	Description
∇	gradient
$\nabla\cdot$	divergence
$\delta(\,)$	Dirac delta function
$\otimes$	tensor product
$\lvert\ \rvert$	absolute value
Δ	change of quantity

Special Symbols

Symbol	Description
$\perp$	Normal component

Abbreviations

Symbol	Description
CCH	City and County of Honolulu
CFD	Computational Fluid Dynamics
CSF	Continuous Surface Force
DOF	Degrees Of Freedom
ECM	Electromagnetic Current Meter
FEMA	Federal Emergency Management Agency
FV	Finite Volume
HDF	High Discharge Flume
IOT	Indian Ocean tsunami
LHS	Left-Hand Side
MPI	Message Passing Interface
OpenFOAM	Open Field Operation And Manipulation
pBC	Pressure Boundary Condition
PT	Pressure Transducer
RAM	Random-Access Memory
RANS	Reynolds-Averaged Navier-Stokes
RC	Reinforce Concrete
RHS	Right-Hand Side
SPH	Smoothed Particle Hydrodynamics
SWL	Still Water Level
TWB	Tsunami Wave Basin
VOF	Volume Of Fluid
WG	Wave Gauge
WSE	Water Surface Elevation

1 Introduction

1.1 Background and Motivation

Tsunamis are series of extremely long waves generated by a rapid displacement of a large volume of water. These displacements are usually due to impulsive disturbances such as the uplift or subsidence of the seafloor during submarine earthquakes, landslides, volcanic eruptions, underwater explosions, or asteroid impacts. As a consequence of their extremely long wavelengths the energy becomes distributed through the entire water column, even in the deepest parts of the ocean. Once generated, they propagate outward in all directions from the source. The wavelength, amplitude and period are all dependent upon the generating mechanism and size of the source.

In deep water, the amplitude of a tsunami wave may only be on the order of centimeters up to approximately one meter. The wave celerity can reach speeds of up to 800 km/hr in the open ocean and can travel across entire ocean basins with loss of very little energy. Given the extremely mild steepness of tsunami waves in the deep ocean, it may pass underneath ships without anyone onboard noticing.

Tsunamis arrive at the coast as either a trough-lead or crest-lead wave, with a typical period of 10 to 45 minutes between successive waves. In coastal regions, the wave speed can slow down to as little as 30 km/hr due to friction induced by the motion of the water particles interacting with the seafloor. Since the incoming wave behind the first will be travelling at a much higher speed, the wavelengths compress as they travel closer to the shore. As this occurs, the wave energy dispersed throughout the column is forced upwards and the wave heights grow. The tsunami height at the shore tend to be highly correlated with the coastal bathymetry and can vary significantly in the longshore direction. Depending on the tsunami characteristics and the underwater topography, the leading edge of the wave may break before advancing inland as a turbulent bore, as depicted in Figure 1.1. In other instances, when the conditions are conducive, the tsunami may move inland in the manner of a fast moving tide.

Figure 1.1: Photograph of the surge created from the first tsunami wave arriving at Rikuzentakata (roughly 1.5 km inland from the bayfront) in the Iwate Prefecture, Japan during the 2011 Tohoku tsunami (Hagen, 2014).

A comprehensive emergency management system to protect coastal communities against the effects of tsunamis consists of pre- and post-event considerations. The former can be further subdivided into categories aimed at increasing public awareness and preparedness, and directly mitigating the effects by establishing zoning bylaws and soft- and hard-engineering solutions. The greater majority of past efforts have been devoted to the development of more effective early warning systems, accurate inundation maps, and efficient evacuation plans. Although these are all essential elements to having a comprehensive system of protection, damage caused to critical infrastructure necessary for restoring a community back to normal operation still remains unaddressed. The conclusions from a field survey conducted in the aftermath of the December 26th, 2004 Indian Ocean tsunami (IOT), reported by Ghobara et al. (2006), highlight the devastating consequences of this. Damages to bridges and roadways throughout the Aceh province of Indonesia were reported to severely delay rescue and relief efforts by first responders. The loss of several port facilities due to the damage from the tsunami prevented relief supplies, equipment, and materials from reaching inland. To add to the complicated situation, the collapse of several transmission and communications towers disrupted cellular network service and access to power across large expanses. Even despite early warning systems and evacuation plans, all of these reported damages that hinder the ability for a quick recovery from such disasters would not be avoided.

In the case of near-source tsunamis or where the distance to high ground is too great, horizontal evacuation may become impractical. In these instances, resilient refuge structures capable of withstanding the effects of earthquakes and tsunamis may be a viable alternative. Reconnaissance missions carried out in Thailand and Indonesia shortly after the 2004 IOT showed that several reinforced concrete (RC) buildings remained intact, despite not being designed to withstand the effects of tsunamis. Other reports, such as that of Yeh et al. (2013) have shown examples of remarkable failure of RC structures under the influence of tsunamis. While the structures as a whole were still largely intact, through a combination of hydrodynamic force, buoyant force, and reduced


(a) (b)

Figure 1.2: Destruction of nearshore structures during the 2011 Tohoku tsunami: (a) collapsed seawall at Ryoishi in Kamaishi (Takahasi et al., 2011) and (b) overturned concrete structure in Oganawa City, Myagi Prefecture (Couresy of Dr. Ioan Nistor).

soil stability, several RC structures were completely overturned (see Figure 1.2). Other types of damages to structures such as the failure of RC shear walls due to hydrodynamic and hydrostatic forces exerted by tsunami-induced flooding are reported by Chock et al. (2013). Motivated by similar findings from previous field investigations, an extensive review of design guidelines for cities and districts in tsunami prone areas was conducted by Nistor et al. (2009). Unlike earthquake loading, they discovered that tsunami-induced forces are not properly quantified and accounted for in existing codes. As coastal cities around the globe continue to increase in population and as mitigation strategies based solely on horizontal evacuation become less feasible, the demand to construct resilient refuges and infrastructure capable of withstanding extreme wave events is certain to follow. As a prerequisite, a practical understanding of bore-structure interaction will be necessary before establishing reliable design guidelines for tsunami-resistant structures.

1.2 Study Objectives

The principle topic of this work is related to the computation and analysis of the complex free surface flows that occur in bore-structure interaction and pneumatic long wave generation problems. The main objectives of the study are subdivided into these two major sections and proposed as follows:

1.2.1 Bore-Structure Interaction

- assess the capabilities of the two-phase volume of fluid (VoF) solver *interFoam* to reproduce a set of physical experiments concerned with bore-structure interaction;
- perform a qualitative analysis on observed flow behaviour in the vicinity of the structure and relate them to the quantitative results;
- investigate the performance of recent design guidelines for tsunami-resistant structures by comparing validated numerical results to analytical predictions; and
- examine the influence of water of varying depths residing on the channel bed on bore propagation characteristics and how that influences the interaction with structures.

1.2.2 Pneumatic Long Wave Generation

- assess the capabilities of the two-phase volume of fluid (VoF) solver *interFoam* to reproduce a set of physical experiments concerned with a novel experimental long wave generation technique;
- perform a step-by-step analysis during wave formation to improve the understanding of the generation process;
- monitor sensitivity of the results to changes in the test setup to aid in future operating considerations or in the design of similar wave generation devices.

1.3 Scope

The performance evaluation of the numerical solver will be conducted through a quantitative and qualitative comparison of experimental, analytical and numerical results. The items of primary relevance considered for the comparisons include: (i) time series of water surface elevation, (ii) temporal evolution of waveforms and water surface profiles, (iii) time-histories of pressure, (iv) flow velocity and (v) net force acting on rigid objects. An in-depth analysis of the generated data is performed to help improve the overall understanding of the underlying physical mechanisms.

Once the numerical model is validated against experimental data and analytical predictions, it is applied to investigate sensitivity of the results to changes in test configuration and domain geometry. In the case of the bore-structure interaction section, water layers of varying thickness are considered in the downstream section of the channel to gauge its influence on bore propagation characteristics. It is expected that the subsequent interaction with structures will be heavily influenced by the bore profile and its temporal evolution. Since tsunamis occur as series of waves, the ones arriving after the first may interact with structures residing on a partially-flooded terrain. Thus, elucidating the effects of downstream depths on how bores interact with structures may have practical relevance to tsunami design problems.

In the case of the pneumatic long wave generation simulations, the validated model is applied to investigate the influence of the outlet dimensions connecting the storage tank and propagation section on wave characteristics. Various still water depths are also considered to gauge its effect on the latter. The findings presented in this section may be used to aid in decisions for future test configurations or in the design of similar wave generation devices.

1.4 Novelty and Contribution of the Study

In the past, investigations of bore-structure interaction have typically been limited to the realm of physical modelling. In comparison, the number of examples found in the literature of experimental studies dwarfs that of related numerical ones. In light of them all, the novelty of the present work is primarily contained with the treatment of the fluids involved and type of analysis conducted. Although similar simulations have been performed using single-phase numerical models (such as SPH), the present study is one of the first to apply a two-phase model that captures the effect of entrained and entrapped air in bore-induced loading processes. Further, the model scales employed in the current numerical work (set by the physical experiments that the model is validated to) is one of closest to prototype conditions found in the literature. The primary benefit of this that was exploited in the current study is that comparison of the results to existing design guidelines become more useful. Although this type of comparison has been done at smaller scales, the results in the present study help to reveal the scale effects that were present in past investigations that went largely unnoticed. Another aspect of the novelty contained in this work is related to investigating the effect of downstream depths on dam-break waves. Although there are examples of notable experimental studies in the literature, this is the first numerical study to investigate the effect of a number of different downstream depths. St-Germain et al. (2012) was the first to attempt a numerical investigation of these effects, however, due to difficulties with the boundary conditions it was not possible to simulate a thin layer of water residing on the channel bed. Rather, only one relatively deeper downstream depth was considered.

Finally, with pneumatic long wave generation being a relatively new concept applied in laboratories for generating tsunamis, very little knowledge has been disseminated on operating or designing such facilities. This is the first study to use a validated numerical model to study how different test configurations affect the generated waveform and subsequent overland flow characteristics.

1.5 Thesis Outline

The work presented in this thesis has been divided into six components which form the whole. Chapter 1 provides a brief background on the topics that are discussed in this thesis and outlines some of the perspectives that provided the basic motivation for this work.

In order to uncover the gaps in existing knowledge on the topic considered in this work, a review of related scientific literature is presented in Chapter 2. This provides not only the necessary technical background to contextualize the analysis that will be presented in later sections, but also establishes the scientific merit of the problem at hand.

In Chapter 3, the numerical tool used as the vehicle for the investigations performed in this work is described. The governing equations for the two-phase flow are introduced along with brief descriptions of the discretization process and solution procedure.

Forming the core of this thesis, Chapter 4 and 5 are the results sections for the two major topics that make up this thesis: bore-structure interaction and pneumatic long wave generation. Each of these two chapters are subdivided into descriptions of the physical experiments, calibration of numerical parameters, comparison to the experimental results, and results of the numerical experiments.

Finally, the general conclusions of this work are presented in Chapter 6 along with recommendations for future work

2 Literature Review

The development of numerical models to study fluid dynamics often relies on data derived from physical modeling studies for validation purposes. Further, since physical models are driven by the same laws as the prototype phenomenon being studied (as opposed to a human-constructed mathematical model), they often serve as a first-basis for scientific investigation. However, the potential amount of data that can be produced from a validated numerical model offers an opportunity to perform analysis that would not be possible with physical results on their own. Although both have their own merits, this literature review will primarily focus on past contributions made possible through the application of laboratory experiments. In instances where particularly noteworthy findings are documented, or where they may have implications for the novelty of the work presented in this thesis, attention will also be given to past numerical studies.

This chapter is divided into three main components. The first deals with a number of methods that have been devised for generating tsunami waves in laboratory basins and flumes. Here, a review of the various techniques for generating the initial wave in deeper water as well as methods for generating hydraulic bores in a more direct fashion will be conducted. The second section of the literature review is devoted to exploring previous experimental work aimed at advancing the current understanding of the physical interactions occurring between bores and structures. Finally, a brief review of numerical studies related to bore-structure interaction problems is presented.

2.1 Physical Modeling of Tsunami Waves and Hydraulic Bores

Depending on the precise objective of the work and the facilities available to researchers over the past several decades, numerous methods for generating tsunami waves and hydraulics bores in the laboratory have been developed. Although the propagation of tsunamis across large ocean expanses is not the focus of this study, many previous works have relied on generating waves in deeper water which, in turn, is used to propagate the wave and inundate coastal regions. Furthermore, since the wave characteristics prior to shoaling and arriving at the coast can affect the onshore hydrodynamics, the method for generating waves, even in deep water, is relevant to the current work.

2.1.1 Solitary waves

The solitary wave paradigm for the physical modeling of tsunami waves has roots in the milestone work presented by Hammack (1973). In his work, it was demonstrated that a positive initial surface disturbance (generated by volume displacement) will eventually decay into an oscillatory wave train with leading solitary waves. Since the initial suggestion of this idea, the solitary wave has been frequently applied to model some of the important features of tsunamis approaching and inundating the coast. Examples from the literature are numerous and include those such as Goring (1978), Synolakis (1987), Ramsden (1996), Tonkin et al. (2003), and Robertson et al. (2011) to name a few. Briggs et al. (1995) conducted a series of laboratory experiments to better understand the physical parameters involved in three-dimensional tsunami runup. In what later became more widely known as the *conical island* experiments, solitary waves with maximum amplitudes of 0.042m were generated in still water depths of 0.32 and 0.42m by the single forward motion of a wave paddle (often called a piston-type wavemaker). In some instances, the refraction of the wave around the island caused constructive addition of the two waves converging at the leeward side, resulting in relatively high runup values.

By the sheer number of precedents found in the literature, the impression left on the reader is that the solitary wave is a preferred model for tsunamis. More recently, however, Madsen et al. (2008) investigated the geophysical relevance of the solitary wave paradigm. Using a numerical model as the vehicle for their investigation, Madsen et al. (2008) set out to determine the threshold distances required for the effects of wave nonlinearity and dispersion to manifest for a given initial surface disturbance. In one scenario, using geophysically realistic parameters for a tsunami in the deep ocean, they found that the threshold distance for disintegration into a train of solitons was magnitudes large than the width of any ocean basin on the Earth. The authors conclude that existing geophysical scales do not allow for the formation of leading solitons for typical tsunamis propagating in the deep ocean or even over flat continental shelfs.

In a study aimed at developing analytical solutions for estimating long wave runup on a beach, Chan and Liu (2012) further examine the statements made on the solitary wave paradigm. To validate their model to field observations made during the 2011 Japan Tohoku tsunami, they compare several theoretical waveforms to that of the tsunami captured by a GPS buoy located 13km offshore (200m water depth). In Figure 2.1, it is observed the solitary wave (dotted line) with a comparable height to the leading wave falls short in terms of wavelength by a substantial margin. The authors estimate from the field observations that the tsunami had a wave period of T = 17 minutes at the Iwate South GPS station. The solitary wave, on the other hand, had an effective wave period of just T = 3 minutes, much shorter than the observed data. The results of the study provide further support that solitary waves lack in comparability to the length and time scales observed during real tsunami events.

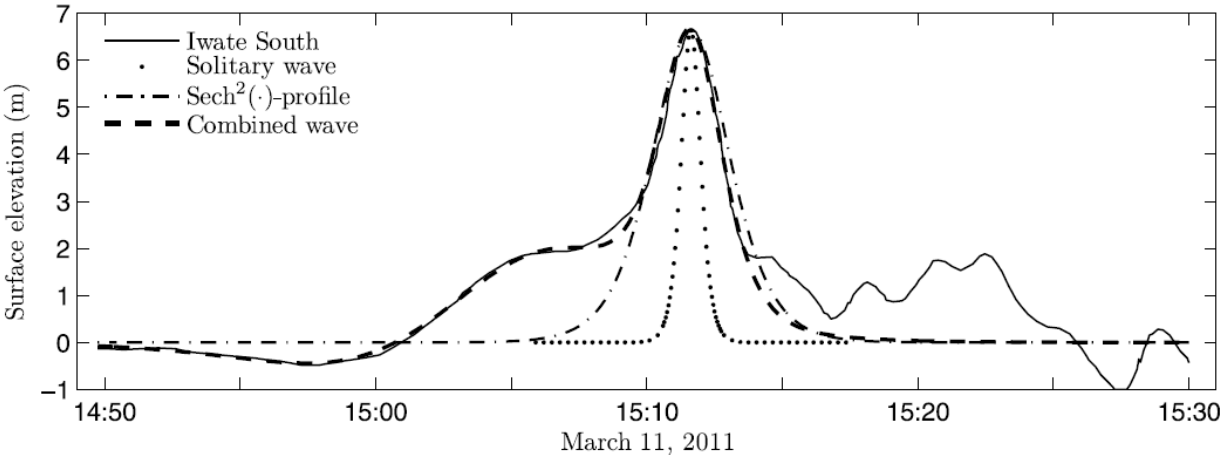

Figure 2.1: Time record of surface elevation at the Iwate South GPS buoy during the 2011 Japan Tohoku tsunami (Chan and Liu, 2012).

2.1.2 Volume-driven wave generation

A new concept for tsunami wave generation at laboratory scales is presented by Rossetto et al. (2011). The primary ambition of the project was to develop a new wave generating device capable of producing tsunamis at a wide range of model scales consistent with the characteristics of earthquake-generated tsunamis. This entails the ability to create extremely long wave lengths and leading depressions waves often observed during real events.

The process behind the tsunami wave generation is said to be adapted from the Pneumatic Tide Generation concept originally developed to add tidal effects to large area coastal models (Wilkie and Young, 1952). The operating principle of this device is to withdraw a volume of water from the basin before releasing it again in a controlled manner. The extracted water is stored in a sealed tank (referred to as the tank or chamber) at the offshore end of the basin with a submerged inlet/outlet directed shoreward. A high-powered fan (pneumatic pump) extracts air from the chamber and in turn draws water from the basin. A safety and control valve are located at the top of the chamber to regulate the internal pressure while the pump evacuates the air. The safety valve is manually operated and remains at a fixed setting to ensure that the water level never reaches the tank roof. The control valve is computer-operated and receives time series of valve setting to produce the desired wave shape. A generalized illustration of the setup is provided in Figure 2.2.

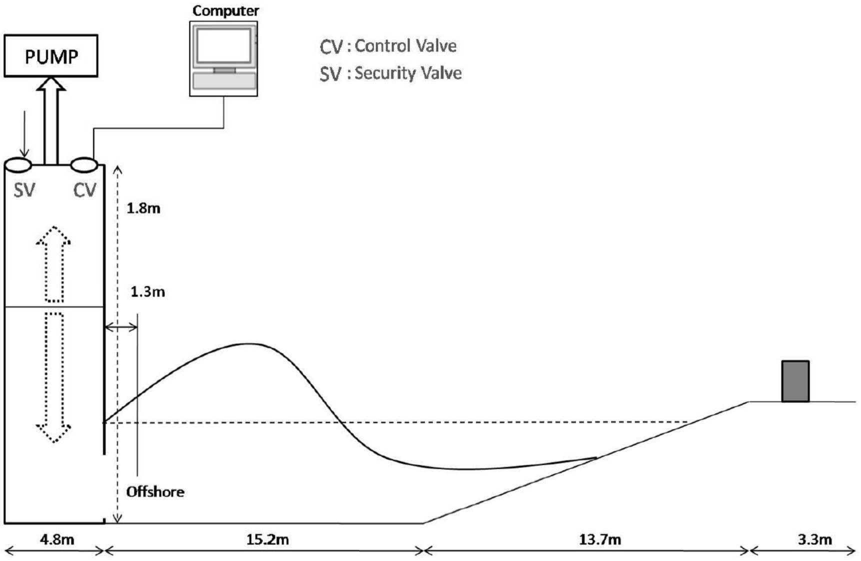

Figure 2.2: Schematic diagram of the pneumatic long wave generator (Rossetto et al., 2011).

Using the setup described, the researchers were able to reproduce the tsunami trace signal derived from the echo-sounder onboard the Belgian “Mercator” Yacht during the 2004 Indian Ocean tsunami. At the time of event the yacht was located on the continental shelf at a water depth of 12-13m. At this distance from the shore, the trace no longer represented the offshore waveform but a shoaled tsunami wave. Although significantly more challenging to reproduce, Allsop et al. (2014) used the tsunami generator to reproduce the Tohoku tsunami signal recorded by an ocean-bottom pressure gauge at a water depth of approximately 1000m, 40km offshore. Relative to the solitary wave comparison performed by Chan and Li (2012), a substantial leap in progress is observed towards replicating the length and time scales of real tsunami events in scaled laboratory models. The comparisons are given in Allsop et al. (2014) and provided here in Figure 2.3.

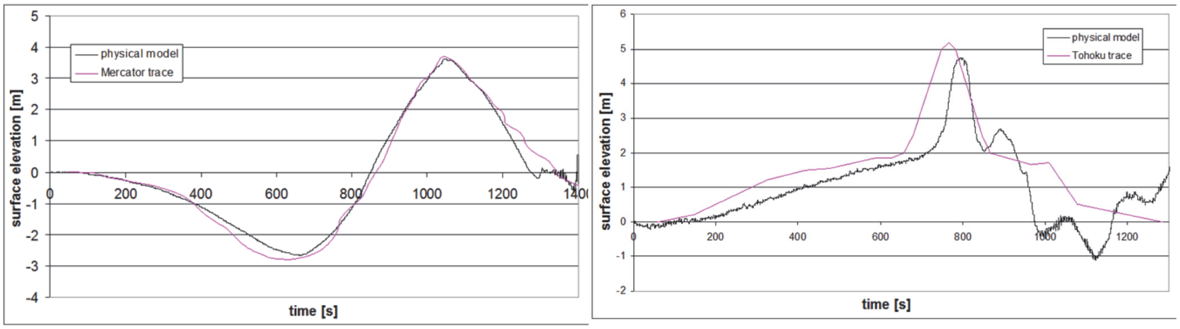

Figure 2.3: Experimental reproduction of the Mercator (2004 Indian Ocean tsunami) and TM2 (2011 Japan Tohoku tsunami) tsunami signals using the pneumatic wave generator described by Rossetto et al. (2012). (Allsop et al., 2014).

During preliminary testing to gauge the capability of the device to generate other types of waves, Allsop et al. (2014) note a potential limitation of generator to produce solitary waves (or solitary-like waves). With regard to the maximum height the generated wave could attain, they found that increasing the target height (by making appropriate adjustments to the control valve) did not necessarily result in increases in wave amplitude. Instead, as the steepness of the wave increased, the initial wave tended to separate into a series of sharp peaks.

In a study performed at Oregon State University, Lukkunaprasit et al. (2009) utilized a similar wave generating principle to investigate tsunami-induced hydrodynamic loading on structures. An inverted water tank with a submerged control gate covering the outlet was installed at the upstream end of a 40m-long x 1m-wide channel. Upon opening of the control gate, an elevated mound of water was generated in 0.475m of still water depth which proceeded to shoal and break over a compound-slope beach. The authors note that this wave generation mechanism “hardly creates a clean solitary wave” but is justified with reference to the fact that real tsunamis seldom form solitary waves. Although the authors did not venture to provide further detail, it is hypothesized that they observed a similar disintegration of the main wave into a train of two or more elevated waves.

While still falling within the category of volume-driven methods, a comparably different approach to long wave generation is described by Goseberg et al. (2013). To address identified deficiencies in other state-of-the-art long wave generation techniques, the authors discuss the inner workings of the so-called pump-driven wavemaker. In a closed-circuit wave flume located at the Franzius-Institute for Hydraulic, Waterways, and Coastal Engineering experimental facilities, numerous tests were devised to conduct a performance analysis of the rig. Situated at the midsection of one its straight segments (see Figure 2.4 for technical drawing), the variable-speed high-capacity pipe pumps accelerate water in either positive (deposit) or negative (withdraw) directions to create elevated or depression waves. A proportional-integral-derivative (PID) controller is used in a controlled feedback system, adjusting the pump speeds to reduce the error between measured and target values

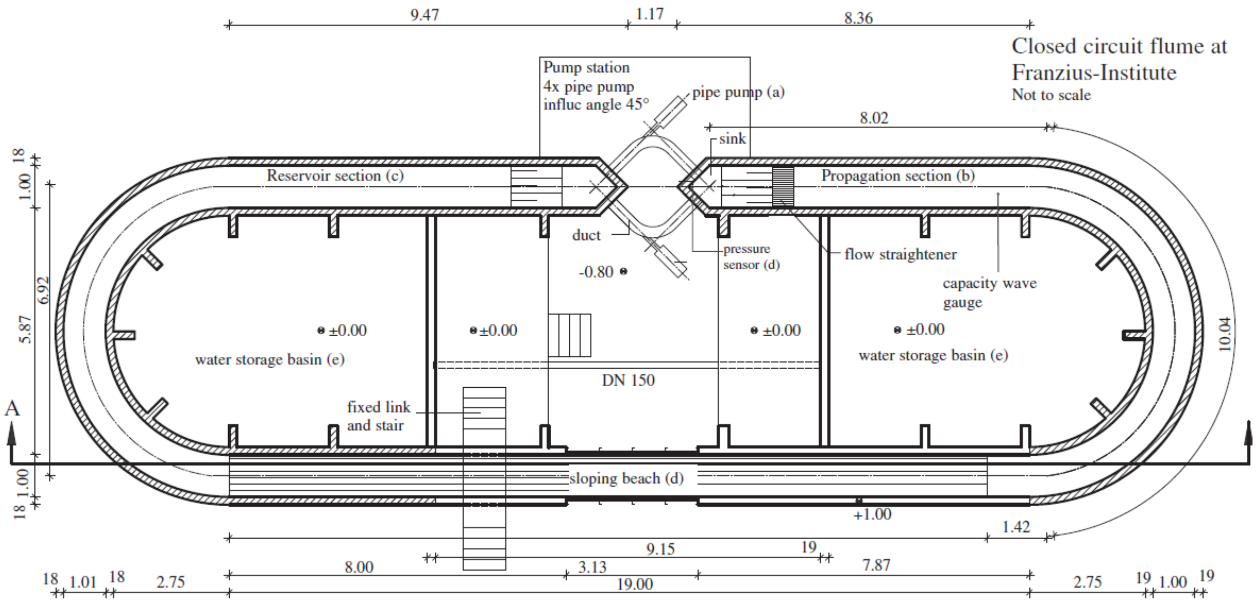

Figure 2.4: Schematic diagram of the closed-circuit flume and its components: (a) pump station, (b) propagation section, (c) reservoir section, (d) sloping beach, and (e) storage reservoir (Goseberg et al., 2013).

for wave height. The tactic is analogous to active wave absorption methods commonly applied to piston-type wavemakers to account for the influence of the reflected waves on the wave generation process.

As one of the main components of the performance analysis, Goseberg et al. (2013) test the PID controller setup to reproduce a numerical account of surface elevation near the shores of Padang, Indonesia during the 2004 Indian Ocean tsunami. As depicted in Figure 2.5, the waveform produced in the closed-circuit flume exhibits good agreement with the target signal. In this particular case, the root mean square error is even smaller than that observed in the previously mention study of Allsop et al. (2014) using the pneumatic long wave generator. This may be in part due to the direct benefits

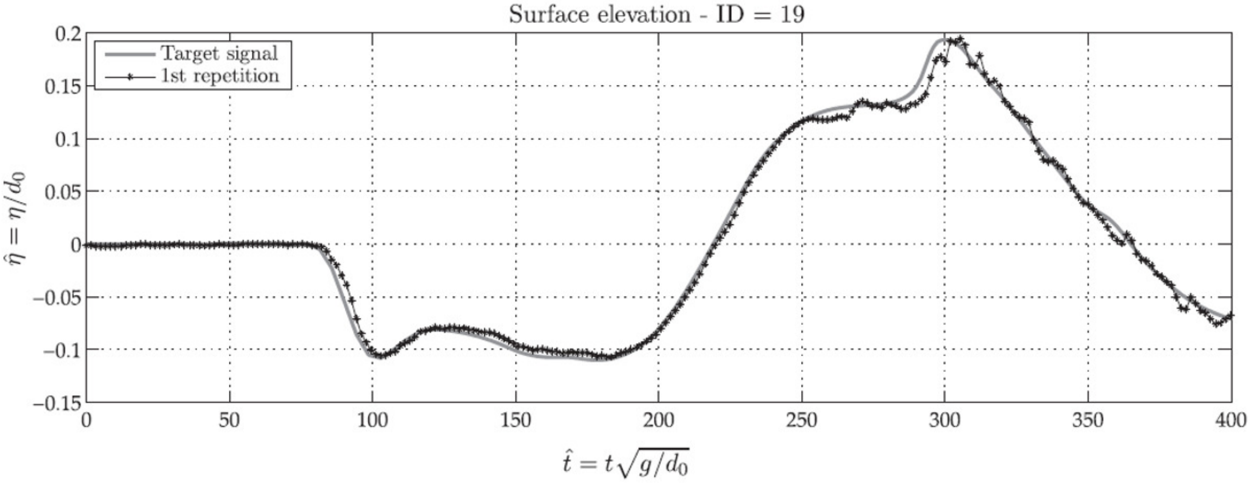

Figure 2.5: Pump-driven wavemaker reproduction of a tsunami trace deduced from a numerical model of the 2004 Indian Ocean tsunami at the City of Padang (Goseberg et al., 2013).

of implementing a real-time feedback system which would be more difficult in the case of the pneumatic long wave generator (longer response time between pressure inside chamber and formation of wave). Given careful calibration of the valve setting time series, however, the two techniques show comparable capacities to generate trough lead tsunami signals with realistic length and time scales.

2.1.3 Dam-break waves

A common method for the experimental reproduction of the surge flow associated with near or onshore propagation of long waves is to generate a dam-break wave. In this approach, a body of water residing in an upstream reservoir with an initial depth h_u is suddenly released and allowed to collapse under its own weight. An elevated wave is generated in the downstream section as the reservoir depletes. The leading edge of the resulting surge propagates through a channel section with an initial downstream depth h_d. The motion is typically initialized by the rapid removal of a control gate separating the upstream and downstream section. The initial condition of a dam-break scenario with associated parameters is depicted in Figure 2.6.

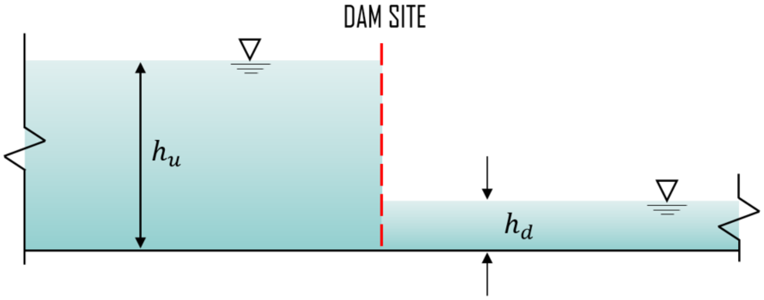

Figure 2.6: Generalized schematic for the initial condition of a dam-break scenario

Cross (1967) was among the first to employ the dam-break approach and to directly link his conclusions to tsunami-related phenomenon. Since control of the time and length scales of inundation could be easily controlled by altering the geometry of the reservoir, the dam-break approach became one of the favoured models to study long waves with a turbulent leading edge. Despite their practical relevance, it was not until Chanson (2006) who showed that a tsunami surges over dry or inundated coastal plains in a way similar to a dam-break wave. A frame-by-frame video analysis was performed on footage captured in the streets of Banda Aceh during the 2004 Indian Ocean tsunami. By identifying visual markers in the footage and using them to make reasonable inferences about the distances involved, Chanson was able to reconstruct the free surface profile and surge front celerity. In comparing this data to theoretical developments that describe dam-break wave properties, a reasonable level of agreement was observed. Thus, Chanson (2006) provides a strong physical analogy between tsunami surges and dam-break flows.

For an initially dry, horizontal channel segment, Chanson (2009) presents a simple analytical solution to the shallow water equations (SWE). The work extends that of Ritter (1892) to describe the free surface profile in the ideal fluid (viscosity and friction is be neglected) region as well as the friction-dominated surge front of a dam-break wave. As one of the more advanced analytical tools for solving dam-break waves, the solutions will be used later in thesis as a step to validate the numerical model. Figure 2.7 defines the individual components of the dam-break wave which are handled separately in the analytical solution. Zone 1 represents a region of undisturbed fluid contained inside the reservoir. Zone 2 is treated as an ideal fluid and connects the undisturbed upstream fluid to Zone 3, representing the friction-dominated wave tip region.

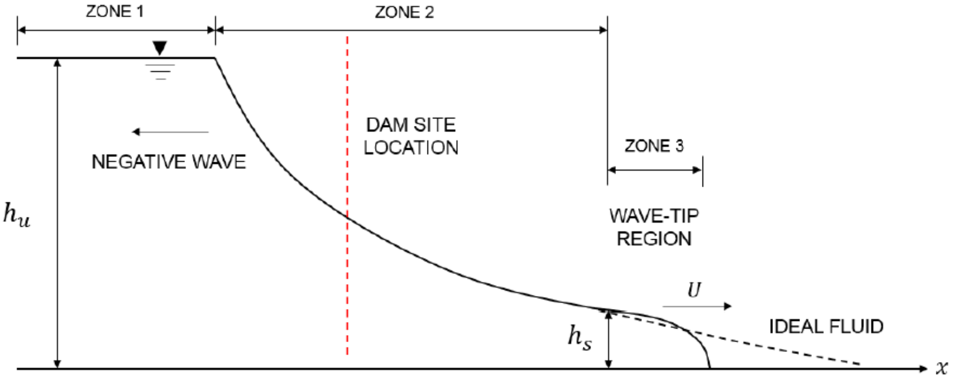

Figure 2.7: Sketch of a dam-break wave in a dry horizontal channel (adapted from Chanson, 2009).

By applying the method of characteristics to solve the SWE, the depth (d) at any point between the leading edge of the negative wave and the start of the friction-dominated wave tip in a horizontal channel can be calculated as

$$d = h_u \left(\frac{2}{3} - \frac{x}{3t\sqrt{gh_u}} \right)^2 \tag{2.1}$$

where x is the streamwise distance with an origin at the gate location and t is the time elapsed after gate removal.

To approximate the shape of the flow-resistance dominated wave tip region the same one-dimensional SWE are applied albeit with a different set of starting assumptions. For this, friction is maintained while inertial and acceleration terms are neglected. Applying these assumptions to the SWE and integrating over time yields the time-averaged diffusive wave equation, where the depth (d) is given as (Chanson, 2009)

$$d = \sqrt{\frac{f}{4} U^{*2} \left(X_s^* - \frac{x}{h_u} \right)}, \tag{2.2}$$

f is the Darcy-Weisbach friction coefficient, U^* is the dimensionless wave front celerity, X_s^* is the dimensionless location of the wave front, and X^* is the dimensionless location at which the depth is being evaluated. In order to evaluate equation (3.3), the dimensionless wave front celerity must be solved for such that it satisfies the following expression

$$\frac{8}{3f}\frac{\left(1-\frac{U^*}{2}\right)^3}{U^{*2}} = t\sqrt{gh_u}\,. \tag{2.3}$$

Once the dimensionless wave front celerity U^* is acquired, the dimensionless location of the wave front (X_S^*) can be computed as

$$X_S^* = t\sqrt{gh_u}\left(\frac{3}{2}U^* - 1\right) + \frac{4}{fU^{*2}}\left(1-\frac{U^*}{2}\right)^4 \tag{2.4}$$

which can then be substituted into equation (2.2) to solve the shape of the wave tip region at any time t. The transition from the ideal fluid region to the friction-dominated wave tip region occurs where the depths calculated from equation (2.1) and (2.2) are equal. This particular formulation ensures that the mass of fluid held inside the ideal wave tip region is equal to that held inside friction-dominated wave tip region, as well as ensuring continuous fluid velocity across the boundary separating the two regions.

2.2 Physical modeling of Bore-Structure Interaction

This section of the literature review pertains to past experimental investigations that aim to elucidate the physical mechanisms underlying the interaction between hydraulic bores and surface piercing structures. Since there is pertinent distinctions to be made in the behaviour of the flow in front of or around two- and three-dimensional structures, the review is subdivided into these parts. Wherever applicable, the contrasts observed between the two cases will be discussed.

For clarity in the discussions that follow, Figure 2.8 illustrates a typical time-history of force exerted on a structure resulting from the impact and passage of a hydraulic bore. In laboratory scale bore-structure interactions, there are three discernible features that can be identified in the force signal. The impulsive force, otherwise known as the slamming or surge force, is generated at the initial impact of the bore with the structure. The impulsive load is characterized by a sudden and sharp rise in the force and is thought to be highly influenced by the steepness of the bore front (Yeh, 2007). The high pressures generated during the sudden slam of the bore front results in the ejection of a volume of water which becomes the splash or initial runup. A second transient peak in the force occurs when

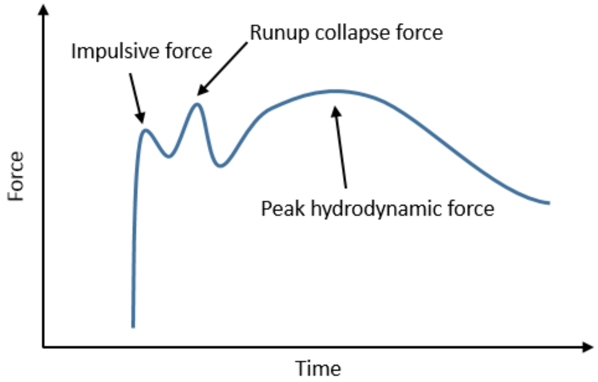

Figure 2.8: Generalized time-history of bore-induced forces exerted on a structure

the initial runup collapses back onto the incoming flow. Sometime thereafter, the third and final defining feature of the signal is observed. The peak hydrodynamic force occurs when the flow velocity and inundation depth work together to produce the peak momentum flux $(hu^2)_{max}$ at the structure location. It is important to note that the relative values of the three peaks depicted in Figure 2.8 is meant to represent a generalized case. That is to say, depending on a variety of conditions, the height of the peaks in relation to each are subject to change. One of the objectives of the following review is to examine the conditions that exert influence in the process that results in these changes.

2.2.1 Two dimensional studies

As one of numerous physical experiments carried out by Ramsden (1993), a comparative analysis was conducted on dry (h_d = 0) and wet (h_d = 0.28m) bed bores impacting a vertical wall. In a 36.6m-long x 0.396m-wide x 0.61m-deep flume, dam-break bores were generated by releasing the upstream reservoir into a channel section by the rapid opening of a pneumatic gate. The waves were reflected off an instrumented wall extending entirely across the width of the flume. In order to keep the celerity of the two bores approximately equal, the dry bed surge was created by using an initial impoundment depth of h_u = 0.48m while the wet bed bore was generated using h_u = 0.502m. In the case of the wet bed condition, Ramsden noted that not only was the bore front steeper (Figure 2.9-a), the bore depth substantially exceeded that of the dry bed bore at any point behind the leading edge. With increasing distance from the bore tip, however, the discrepancy between the two decreases and the profiles converge. It is interesting to note that with only a 4.4% difference between the initial impoundment depths used for the dry and wet bed bores, Ramsden was able to maintain a constant bore front celerity. This seems to suggest that the bed condition did not have as large of an influence on the front celerity as others have found (e.g., Leal et al., 2000 and St-Germain et al., 2012). Further, the initial runup tongue generated at impact was observed to be approximately 50% higher in the case of the wet bed bore (Figure 2.9-b). The higher runup observed during the initial splash was attributed by Ramsden to the larger volume of water contained in the bore tip. In terms of pressure exerted on the wall at 1.8cm above the channel bed (Figure 2.9-c), the impulsive pressure generated by the wet bed bore attains a value approximately 50% greater than the relatively constant values (quasi-steady) that occur after t = 1.0 second. In contrast, the impulsive pressure generated by the dry bed surge was approximately equal to the later quasi-steady values. For both conditions, the time record of force exerted on the wall (Figure 2.9-d) shows no evidence of an impulsive force corresponding to the initial peak observed in the pressures. The force is, however, higher during the initial stage of interaction in the case of the wet bed bore up until approximately t = 1.0 second. At around t = 0.75 seconds, a transient spike in the force is observed corresponding to the initial runup tongue collapsing onto the incoming flow. The dry bed case, however, did not display the same propensity, likely owing to the smaller volume of water ejected upwards to smaller heights, resulting in a reduced collapse force.

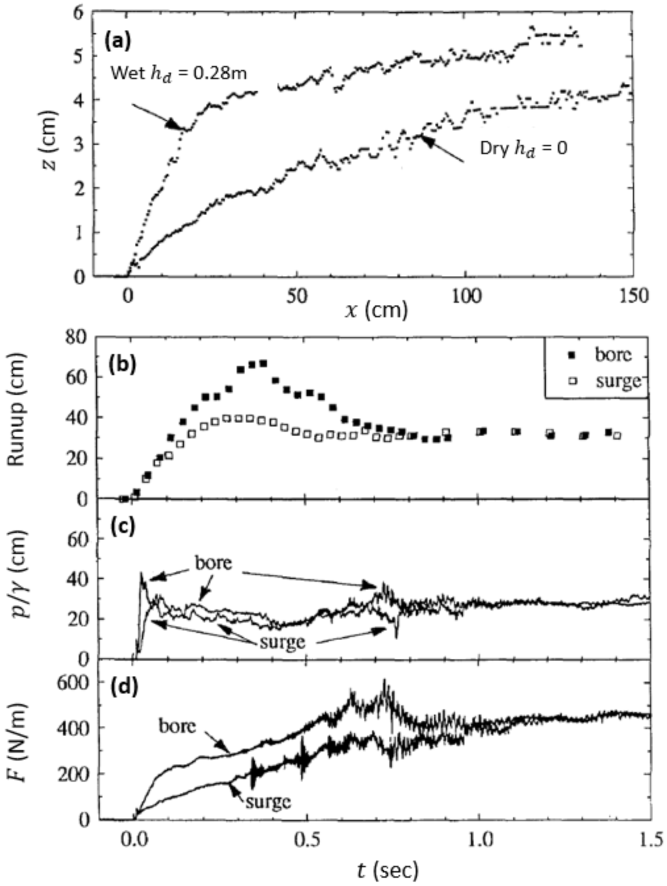

Figure 2.9: Comparison of experimental (a) water surface profiles before impact, (b) runup on the wall, (c) pressure head on the wall at z = 0.018m, and (d) force on the wall for a dry (h_d = 0) and wet bed bore (h_d = 0.28cm). (Ramsden, 1993).

In a 106m-long x 3.66m-wide flume, experiments were performed by Linton et al. (2013) whereby a piston-type wavemaker was used to generate solitary waves with heights ranging from 0.10-0.93m. The flume bathymetry consisted of a 26m-long flat section in front of the wavemaker, transitioning into a 1:12 slope up to an elevation of 2.36m. A false floor was constructed in the final 7.3m segment, representing a flat reef. The still water depth was set to 2.29m such that the reef was exposed to the air (dry bed condition) before being inundated by the surging bore created by the broken solitary wave. The bores were then reflected off of an instrumented wood frame wall extending across the flume width.

In their discussion, the authors make note that no impulsive forces (defined as the sudden and sharp rise and fall of the force when the bore front slams into the wall) were observed during any of the tests. However, in their time record of force provided in Figure 2.2, the maximum impulsive force can be identified as the brief plateau that is seen early on in the signal before the "transient force" occurs, highlighted in the red circle. The transient force described by Linton et al. (2013), which also happens to be the maximum force observed in the time records of force collected, is related to the collapse of the runup tongue onto the incoming flow after impact (previously defined as the runup collapse force in Figure 2.8). Interestingly, Ramsden (1993) had only found the runup collapse force to be the governing load in the case of wet bed bores. The key difference that lead to the contrasting findings is likely related to the model scales employed. Because the wave heights and flow velocities were substantially higher in the case of Linton et al. (2013), the initial runup height and volume of water ejected were larger, causing a higher collapse force.

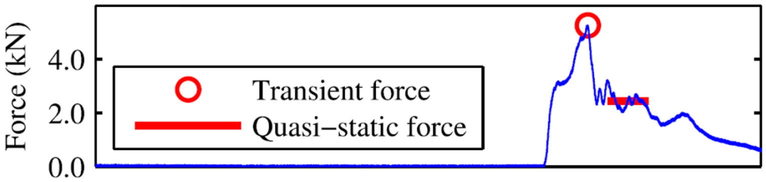

Figure 2.10: Time-history of bore-induced force acting on a wood frame wall (Linton et al., 2013).

Using an almost identical experimental configuration in the same flume described by Linton et al. (2013), Robertson et al. (2011) performed tests with a higher still water level as to submerge the reef with a layer of water 0.30m deep. Although no direct comparisons of the pressures or forces were made, the results of the wet bed bores of Robertson (2011) appear to follow similar trends as the dry bed bores of Linton et al. (2013). In both cases, the impulsive load ranged from 50 – 66% of the later runup collapse force. Furthermore, the impulsive force tended to be slightly higher than the quasi-static loads (or peak hydrodynamic force) occurring at later times. However, due to the fact the bores are fully reflected off of the wall, the incoming flow velocity starts to diminish shortly after initial impact as a result of interacting with the reflected wave.

2.2.2 Three dimensional studies

A series of physical modeling tests were carried out by Arnason (2005) to investigate the interaction between bores and three-dimensional structures of varying cross-sections. Initial reservoir depths ranging from h_u = 0.10 – 0.30m were used to generate dam break bores propagating over an initial downstream depth of h_d = 0.02m. For the square structure with side dimensions of 0.12m, Arnason observed that the transient force occurring near the beginning of the force signal was higher than the hydrodynamic force only in cases when $h_u \leq 0.175$m. Although Arnason refers to this transient force as “the force during impact”, the distinct spike occurring early on in the time-histories plotted in Figure 2.11 is in fact the runup collapse force. As the initial impoundment depth is increased, the actual impulsive force occurring during the collision of the bore front with the structure becomes more distinct. Only in the case of h_u = 0.30m does the impulsive load clearly display its own small peak. For the smaller impoundment depths, the impulsive load tends to blend in with the increasing force up until the collapse force is observed, appearing in the force signal as more of shoulder than a peak. It is clear, especially for the higher impoundment depths employed, that the hydrodynamic forces are relatively greater compared to the collapse force than that observed by Linton et al. (2013). In fact, for the impoundment depths tested by Arnason (2005) that were greater than $h_u \geq 0.20$m, the peak hydrodynamic force was consistently higher than both the impulsive or collapse force. This key difference observed between Linton et al. (2013) and Arnason (2005) is likely associated with two- and three-dimensional effects incorporated into each, respectively. Since a much larger portion

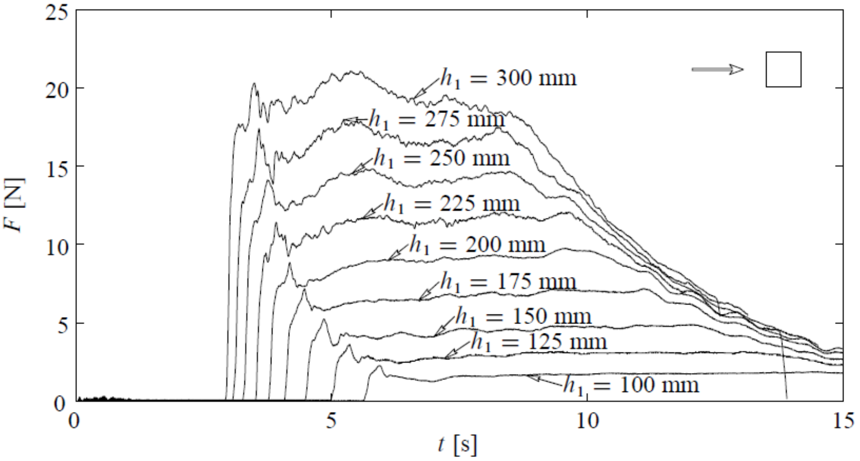

Figure 2.11: Time-history of force acting on the square structure with side dimensions of 0.12m for various initial impoundment depths (Arnason, 2005).

of the wave energy is diverted around the structure sides rather than being reflected upstream, the reflected energy does not interfere with the incident and allows the hydrodynamic force to reach higher values.

In the study Chinnarasri et al. (2013) solitary-like waves were generated by releasing the water stored in a head tank located offshore of a compound-sloping beach. To produce different magnitudes of coastal inundation, the head tank was filled to varying degrees. The generated waves would break as it arrived at the offshore end of the mildly sloping beach and eventually advance onto dry land where it would impact a square structure with side dimensions of 0.15m. Although no offshore wave heights were given, the maximum inundation depth at the structure location ranged from 0.03 – 0.08m. The maximum pressure was observed to occur simultaneously with the impact of the bore front at the lowest pressure transducer mounted on the seaward facing side of the structure. However, due to the relatively shallow water depths at the leading edge, the overall force tended to reach higher values when the pressure was lower and the water depths greater.

Using the same experimental facilities, Lukkunaprasit et al. (2009) apply their collected data to perform a validation of a method to predict tsunami-induced forces stipulated by FEMA P646 (2012). In their analysis they find that, in general, the FEMA P646 predictions using the recommended value for drag coefficient C_D = 2.0 agrees reasonably well with the experimental force measurements. It is conceded, however, that the drag force equation used to produce the estimates fail to predict the measurements taken during the initial impact (impulsive load). Despite the reasonable agreement noted at other times, scaling effects are likely to play a role in the degree to which the predicted and measured values align. For instance, Arnason (2005) found that the required drag coefficient to predict the peak hydrodynamic load ranged from C_D = 2.09 to 2.26. The larger values for C_D tended to correspond to smaller initial impoundment depths. This result suggests that as the model scale is reduced (*i.e.*, becomes closer to prototype scale), a smaller value for C_D may be used. At the moment, no threshold has been defined as to how low small of a model scale is required for C_D to become independent from it.

With regard to the relative magnitude of the impulsive force in comparison to the collapse and hydrodynamic load, Al-Faesly et al. (2012) reports contrasting results. In Figure 2.12, the net streamwise force acting on a square column with side dimensions of 0.30m as a result of the impact and passage of a dam break wave (h_u = 0.55m) is depicted for a dry (Figure 2.12-a) and wet bed (Figure 2.12-b) scenario. The measured impulsive load in the case of the dry bed appears to be 60% greater than the hydrodynamic load. Contrarily, in the case of the wet bed, the impulsive force appears to be damped to a value lower than both the collapse force and peak hydrodynamic load. To the author's knowledge, this behaviour reported by Al-Faesly et al. (2012) in particular to the dry bed scenario is the first to be reported and seems to be at odd with previous studies. For example, Linton et al. (2013) performed his experiments on a dry bed at a similar scale and found the impulsive load to be approximately half of the runup collapse force. Although Linton et al.'s (2013) experiments were two-dimensional, the effects of dimensionality are not expected to manifest until after the impulsive load when the bore reflects off the wall. Furthermore, Linton et al.'s (2013) tests were shown to be repeatable at multiple scales. The results shown in Figure 2.12-a, on the other hand, were not shown to be repeatable and was only reported for a single impoundment depth (h_u = 0.55m). Since this result appears to go against the grain of several others (e.g. Ramsden, 1993; Linton et al., 2013; and Chinnarasri et al., 2013) and was not shown to be repeatable, subjecting it to further scrutiny would certainly not be harmful.

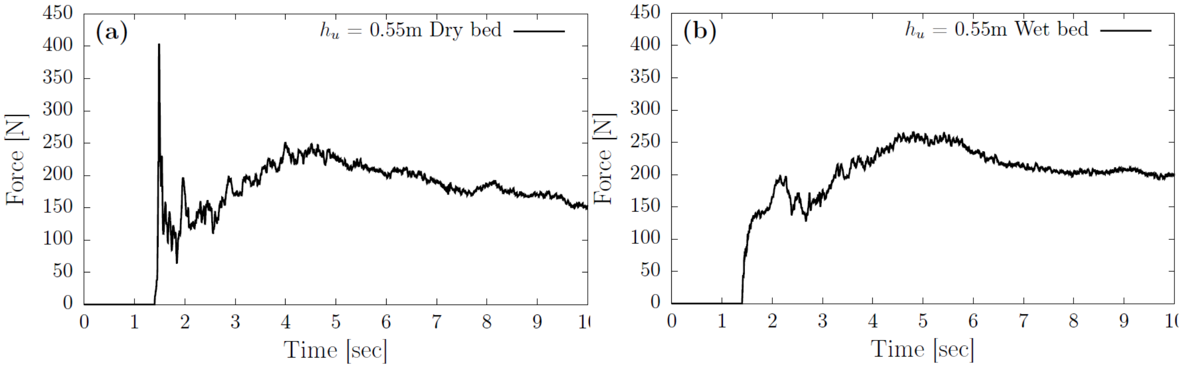

Figure 2.12: Time-histories of streamwise force acting on a square structure from bores generated from an initial impoundment depth h_u = 0.55m propagating on a (a) dry bed (h_d = 0) and (b) wet bed ($h_d \approx$ 0.005m). (Experimental results of Al-Faesly et al., 2012).

2.3 Numerical modeling of Bore-Structure Interaction

Paczkowski et al. (2011) performed a set of numerical tests to reproduce the physical experiments of Robertson et al. (2011) conducted in the Large Wave Flume (LWF) at Oregon State University. The experimental configuration and test conditions have been described in section 2.2.1. Computations were performed with a two-phase volume of fluid solver available within the framework of OpenFOAM. The sensitivity analysis revealed that, in general, the $k - \omega$ SST turbulence model performed the best with regard to simulating the shoaling and breaking of the solitary wave. It was noted, however, that the resulting flow conditions after wave breaking had different characteristics than those observed during the tests. As a result, the authors were not able to obtain satisfactory agreement with the forces exerted on the vertical wall. In response, rather than using the solitary wave to produce the coastal inundation, a constant inflow boundary on the reef using measured velocities and water depths as well as a dam-break scenario was developed. Although both bore generation mechanisms showed better agreement than the broken solitary wave, the dam-break wave produced the highest agreement with the physical results.

A single-phase weakly compressible smoothed particle hydrodynamics (WCSPH) model was used by St-Germain et al. (2012) to investigate the interaction of bores propagating over dry and wet beds with simple three-dimensional structures. Due to the repulsive force of the boundary particles acting on the fluid particles, it was not possible to achieve an initial downstream depth of smaller than h_d = 0.08m for the wet bed scenario. A qualitative comparison of the propagation characteristics before impact for each case is given by in Figure 2.13. It is clear from the image that the additional resistance imposed by the single layer of fluid particles near the channel bottom has several important effects. First, the wet bed bore required 0.56 seconds more to arrive at the same location, indicating a substantial reduction in bore front celerity. In the light of Ramsden's (1993) physical experiments where comparisons of bores propagating over dry (h_u = 0m) and wet beds (h_d = 0.28m) were made, a reduction in celerity of this magnitude would not have been expected. Interestingly, even though the wet bed bore displayed a significantly smaller front celerity, the overall force acting on the square structure at initial impact was reported to be larger than the dry bed condition. This result was attributed by St-Germain et al. (2012) to the deeper and steeper surge front owing to the additional resistance imposed layer of water covering the bottom. This appears to be at odds with the result discussed in the previous section where Al-Faesly et al. (2012) had found the impulsive force to be larger for dry bed scenarios.

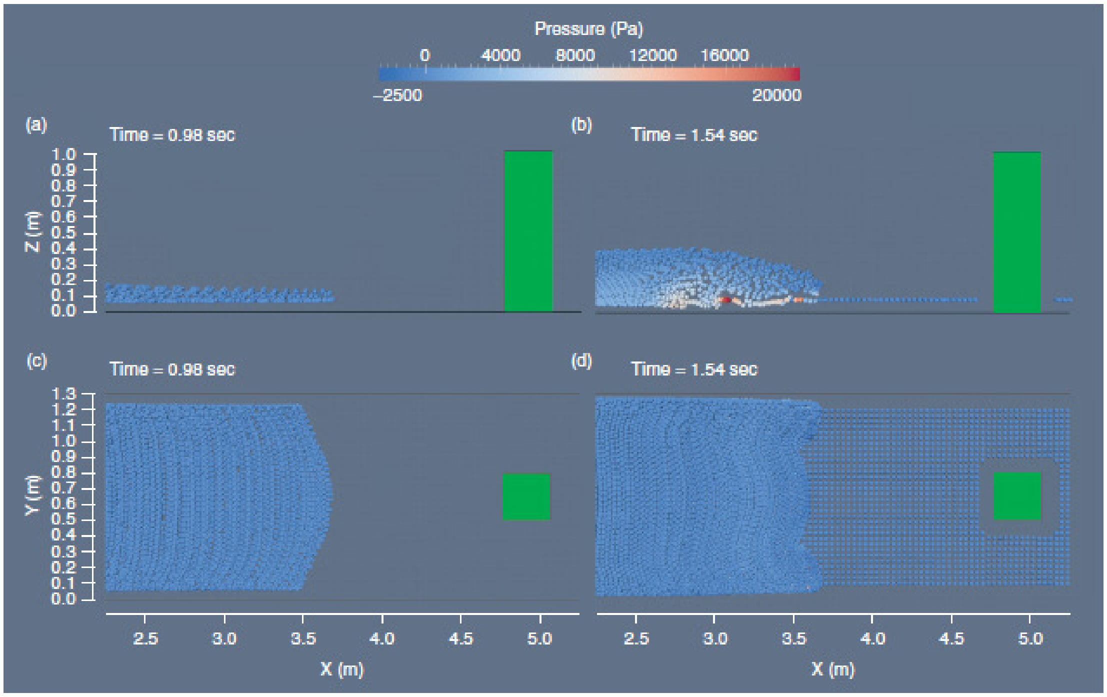

Figure 2.13: Side view (top) and top view (bottom) of the bore front for a dry (left, h_u = 0) and wet bed (right, $h_u \approx$ 0.08m) condition. (St-Germain et al., 2012).

2.4 Discussion

From the literature review presented here, it is clear that a number of challenges still remain in both the modeling of tsunami waves and understanding their interactions with the built environment. With regard to the modeling of tsunami waves from deeper water to onshore, the ability to create realistic shoaling processes and wave steepness are critical issues. The factors that influence the interaction between tsunami-induced bores and nearshore structures (inundation depth, flow velocity, and the length and time scales of the inundation) are intrinsically linked to these issues. Despite their widespread application to serve as a model for tsunamis, errors on the order of a magnitude in terms of spatial and temporal scales occur between solitary waves and real tsunamis close to the shore (e.g., Madsen et al., 2008 and Chan and Liu, 2012). Several new long wave generation techniques are reported in the literature (Rossetto et al. 2011 and Goseberg et al., 2013) and appear to overcome some of these challenges. However, owing to the unique occurrences of these new devices in the laboratory, knowledge about their design and operation is still in its nascent stages. Lukkunaprasit et al. (2009) recognized in their volume displacement generation method that the waves hardly assumed a stable form while propagating through the deeper water. Allsop et al. (2013) also notes a potential limitation to the pneumatic wave generator in terms of producing steeper elevated waves which sometimes separated into a series peaks. Analysis of these types of reported limitations are still far and few in between, and often only a sentence or two is devoted to exposing them. Before the proliferation of these new promising modeling techniques, more work related to the design and operation of the experiments could aid in allowing researchers to produce realistic tsunami waveforms. Some investigation into this matter and modifications to a new basin utilizing similar principles will be performed in Chapter 5 of this thesis.

In terms of understanding the loading process that occurs during the impact and passage of a hydraulic bore with nearshore structures, a number of apparent gaps in existing knowledge has been uncovered. In the case of the first tsunami wave arriving at the coast, the generated bore front will propagate over dry land, also known as a dry bed condition. If the inundating waters do not have time to fully recede before subsequent waves, they will propagate over land already-flooded land. Furthermore, extreme bores occurring during tropical and subtropical storms like that reported by Bricker and Roeber (2015) may encounter similar circumstances when considering the storm surge. This realization has sparked a number of studies to investigate the effect of the bed condition on bore propagation characteristics and the resulting loading process on structures.

Ramsden (1993) had found that with only a minor 4.4% increase in initial impoundment depth (h_u), a wet bed bore propagating over an initial downstream depth of h_d = 0.28m had a bore front celerity equivalent to that of a dry bed bore (h_d = 0). This result appears to suggest that although the initial downstream water does act to hinder the advancement of the bore, it may not be as drastic as that suggested in other studies (e.g., Leal at al., 2006 and St-Germain et al., 2012). With regard to the net force exerted on the wall, his comparison of the dry and wet bed bores revealed that in neither case could an impulsive load be discerned. Combining the results of Robertson et al. (2011) and Linton et al. (2013), further evidence was provided that the dry versus wet bed condition had no substantial influence on the net force acting on the wall. In fact, in both cases, the runup collapse force was the governing load. In three dimensional cases, however, the hydrodynamic force appears to attain higher values (relative to the collapse force) due to less energy being reflected upstream. The physical experiments of Arnason (2005) revealed that as the magnitudes of the depth and velocity increased (and so the scale of the event), the hydrodynamic force tended to be the governing load. Both Arnason (2005) and Lukkunaprasit et al. (2009) investigate the drag force coefficients which can be used to estimate the peak hydrodynamic load. The results appeared to suggest that as the model scale became closer to a full scale event, a smaller drag coefficient could be used to predict the force. However, the model scales employed by both were too large to be able to define a threshold at which point C_D becomes independent of the model scale. Lastly, a relatively recent study by Al-Faesly et al. (2012) reports that in the dry bed case the impulsive load was observed to overshoot that later-occurring hydrodynamic load, casting some uncertainty on the relative magnitudes of the force components displayed in Figure 2.8. An investigation into some of these discussed issues that still stand in the way to attaining a practical understanding of the mechanisms underlying bore-structure interaction will be performed in Chapter 4 of this thesis.

3 The Numerical Method

3.1 Description of OpenFOAM – the Open Source CFD Toolbox

All numerical simulations conducted as part of the present study were performed using OpenFOAM (Open Field Operation And Manipulation), an open source CFD toolbox developed by OpenCFD Ltd. OpenFOAM is a library of C++ code used to create executables, known as applications, for developing and solving user-defined mathematical models as a system of *partial differential equations* (PDEs) with appropriate initial and boundary conditions. The software package consists of a set of precompiled utilities and solvers designed for performing tasks involving data manipulation and for solving a wide range of problems within the sphere of continuum mechanics.

The object-oriented programming techniques of C++ and its implementation in OpenFOAM allow for a top level syntax for tensor operations that closely resemble the PDEs being solved. This feature of OpenFOAM affords users the freedom to modify the code or to develop entirely new solvers and utilities with relative ease.

OpenFOAM is based on the finite volume discretization approach for solving systems of transient transport equations on unstructured meshes in three-dimensional space. A variety of discretization options for temporal, diffusive, convective, and source terms are available to the user, independent of the case geometry and solver being used. Two text-based grid generation applications, blockMesh and snappyHexMesh, are included in the stock download for meshing domains of complex geometry. Additionally, OpenFOAM has the capacity to import externally-generated grids created using other software packages such as ICEM (Ansys, 2015) or Salome (Open Cascade, 2015), for example. Graphic visualizations of the model results can be generated using the internally-linked version of the open source software ParaView (Kitware, 2015), known as ParaFoam.

Parallel computation of individual cases is achieved through the domain decomposition method, whereby the mesh is divided into a number of subdomains equal to the number of processors. Several decomposition methods are available to the user so that, if they choose, they may optimize the effort spent decomposing the domain as well as minimizing the surface area of processor boundaries. For communication across processor boundaries, Message Passing Interface (MPI) is used.

3.2 Governing Equations

3.2.1 Conservation Laws for Mass and Momentum

The numerical solver interFoam solves the three-dimensional Navier-Stokes equations for two incompressible and immiscible fluids, and employs the Volume of Fluid method (VOF) to capture the interface. In a majority of practical coastal engineering problems, the magnitudes of pressure generated are such that treating water as an incompressible fluid is a reasonable assumption (i.e., changes in volume and density are negligible). Although air has a much higher potential for compression relative to water, in small-scale experiments, such as those of the current work, air has a tendency to behave as an incompressible fluid (Sarmento and Falcão, 1985). Furthermore, it is surmised that if the compressibility of air affects the experimental measurements in a perceptible way, discrepancies between those and the numerical results may provide valuable insight into the magnitude of the influence it exerts. Since the incompressible fluid assumption greatly simplifies the calculations, interFoam was deemed an optimal choice for the numerical aspect of the current work.

The mathematical expressions presented in this section are based on writing a single set of conservation equations for the entire flow field, where material properties and field variables are generally discontinuous across the interface between the fluids. Conceptually, it can be thought of as treating the solution domain as a single fluid with rapidly-varying material properties. Following this approach, the conservation laws for mass and momentum can be expressed as (Rusche, 2002)

$$\nabla \cdot \mathbf{U} = 0 \tag{3.1}$$

$$\frac{\partial \rho \mathbf{U}}{\partial t} + \nabla \cdot (\rho \mathbf{U}\mathbf{U}) = -\nabla p + \nabla \cdot \boldsymbol{\tau} + \rho \boldsymbol{f} + \int_{S(t)} \sigma \kappa' \boldsymbol{n}' \delta(\boldsymbol{x} - \boldsymbol{x}')\, dS\,, \tag{3.2}$$

where t is the time, $\mathbf{U}$ is the velocity field, p is the pressure, $\boldsymbol{\tau}$ is the stress tensor, and $\boldsymbol{f}$ represents the acceleration due to body forces acting on the fluids. In this case, the only body force acting on the system is gravity, *i.e.*, $\boldsymbol{f} = \boldsymbol{g}$. For clarity in the discussion that follows, bold characters represent vectors or tensors, and non-bolded characters represent scalars.

The last term on the RHS of equation (3.2) accounts for the source of momentum added to the system by the occurrence of surface tension at the interface. The variables in this term represent the surface tension coefficient, σ, the curvature, κ, and the normal vector, n. Primed variables indicate the value at the interface. The three-dimensional Dirac δ-function integrated over the free-surface $S(t)$ ensures non-zero values for surface tension only when the evaluation takes place on the boundary between the fluids. This form of the δ-function may be expressed as

$$\delta(\boldsymbol{x} - \boldsymbol{x}') = \delta(x - x')\delta(y - y')\delta(z - z')\,, \tag{3.3}$$

where $x, y,$ and z are the spatial coordinates at the location where the δ-function is being evaluated. When the argument to any of the three δ-functions is equal to zero, a value of 1 is returned. Otherwise, it returns a value of 0. For example,

$$\delta(z - z') = \begin{cases} 1, & z = z' \\ 0, & z \neq z'\,. \end{cases} \tag{3.4}$$

However, a particular problem arises when evaluating the integral to account for the surface tension. In the volume-based methodology for capturing the interface employed by the present numerical model, the exact location and shape of the interface is unknown. As a result, the δ-function, which requires spatial coordinates of the interface as input, cannot be directly evaluated. While several methods have been proposed to overcome this problem (e.g., Pucket et al., 1997; Meier et al., 2002; and Renardy and Renardy, 2002), they are often only applicable when specific criteria concerning the interface-capturing methodology are met. In Section 3.2.3, we explore how this term is numerically implemented in the interFoam solver.

3.2.2 Indicator Function

An additional field variable, often called the phase fraction, is introduced into the system to describe the spatial distribution of the two fluids at any given time. The phase fraction is a function bound between zero and one and can be described mathematically as

$$\alpha = \begin{cases} 0, & \text{in fluid } a \\ 0 < \alpha < 1, & \text{in the transitional} \\ \text{region} & \\ 1, & \text{in fluid } b. \end{cases} \tag{3.5}$$

In a physical sense, the phase fraction can be of thought of as the fractional degree to which a computational grid cell is filled with a certain liquid. Hence, it is also sometimes referred to as an indicator function for its ability to indicate the phase-state of a given region in space. Adhering to the nomenclature in equation (3.5), a grid cell that carries a phase fraction value of 0 is entirely filled with fluid a. Likewise, a grid cell carrying a phase fraction value of 1 is entirely filled with fluid b. The transitional region denotes a thin layer between the two pure phases that have combined and exists in a mixed state. Similar to mass, the phase fraction is a conserved quantity and, as such, obeys a transport equation of the form

$$\frac{\partial \alpha}{\partial t} + \nabla \cdot (\mathbf{U}\alpha) = 0\,. \tag{3.6}$$

Once the spatial distribution of the liquid phase fraction has been determined, it is used in a weighted average to update the fluid properties in each cell according to

$$\rho = \rho_a(1 - \alpha) + \rho_b \alpha \tag{3.7}$$

$$\mu = \mu_a(1 - \alpha) + \mu_b \alpha\,, \tag{3.8}$$

where the subscripts a and b denote the values for the two different fluids.

If the concept of the indicator function were applied in reality, it would behave as a step function, jumping discontinuously from zero to one across the boundary between the two phases. However, a critical issue with simulating the convection of such a function is maintaining the transport of a sharp interface while also preserving the boundedness and conservation of the phase fraction (Berberović, 2010). Several methods have been developed to treat this problem, many of which are reviewed by Ubbink (1997) and Ubbink and Issa (1999). The method currently implemented in the VOF solvers available in OpenFOAM v2.4.0 utilize the approach taken by Weller (2008), the creator and chief developer of OpenFOAM. In this approach, the numerical diffusion of steep gradients of the phase fraction is suppressed by introducing an artificial compression term (third term on the RHS of equation 2.9) into the transport equation, taking on the form of

$$\frac{\partial \alpha}{\partial t} + \nabla \cdot (\mathbf{U}\alpha) + \nabla \cdot \big(\mathbf{U_c}\alpha(1-\alpha)\big) = 0\,, \tag{3.9}$$

where $\mathbf{U_c}$ is the compression velocity. The artificial compression term is only active in the thin transitional region surrounding the theoretical location of the interface, achieved by multiplying the divergence of the compression velocity by $\alpha(1-\alpha)$. Travelling in a direction away from and normal to the interface, the artificial compression term vanishes at both limits of the phase fraction and is reduced to equation (3.6). It should be noted that the term *compression* has no relation to the compressibility of the flow, but instead refers to its tendency to shrink the smeared interface caused by numerical diffusion of the phase fraction.

In addition to being active only in the interfacial region, the artificial convective term should strictly limit the flow of the phase fraction to a direction normal to the interface (Berberović, 2010). In this way, the artificial compressive force will act as an equal and opposite vector on either side of the interface and will not affect the natural flow of α, according to equation (3.6). In order to meet these criteria, Weller (2008) proposed a general form to calculate the compression velocity as

$$\mathbf{U_c} = \min[C_\alpha|\mathbf{U}|, \max(|\mathbf{U}|)]\,\frac{\nabla\alpha}{|\nabla\alpha|}\,. \tag{3.10}$$

Typically, the compression velocity $\mathbf{U_c}$ is governed by the first term in equation (3.10). However, it is limited from exceeding the maximum velocity occurring in the system in order to preserve stability of the solution. The compressive coefficient, C_α, controls the intensity of the interface compression. If set to zero, the artificial compressive term in equation (3.9) vanishes and suppression of the numerical diffusion of the interface is turned off. Alternatively, a compressive coefficient value of one yields a conservative compression, while anything larger than one corresponds to enhanced compression of the interface (OpenCFD Ltd., 2015a). For this study, the compressive coefficient C_α is set to one. However, out of curiosity, a single test case was conducted to gauge the effects of having no interfacial compression.

3.2.3 Evaluation of the Surface Tension Term

The accurate calculation of surface tension forces has been one of the main historic problems facing simulations of free-surface flows (Scardovelli and Zaleski, 1999). As mentioned earlier, in the current interface-capturing methodology (VOF), the location of the interface is not explicitly resolved, making a direct evaluation of the surface tension term in equation (3.2) impossible. Furthermore, implementing surface tension as a local discontinuous force (i.e., only acts in a two-dimensional plane), as it is in reality, would result in infinite gradients across the boundary between the fluids. To overcome this problem, Brackbill et al. (1992) introduced the Continuum Surface Force (CSF) model which converts the surface tension force into a corresponding volumetric force which acts inside the transition region (the thin region on either side of the interface where artificial mixing of the two phases occurs in VOF methods). In this way, the theoretically sharp and discontinuous force acting in a two-dimensional plane is smoothed in the vertical direction, making it suitable for application in volume-based free-surface simulations. This conversion by Brackbill et al. (1992) reads

$$\int_{S(t)} \sigma\kappa'\boldsymbol{n}'\delta(\boldsymbol{x}-\boldsymbol{x}')\,dS \approx \sigma\kappa\nabla\alpha\,, \tag{3.11}$$

where the curvature of the interface κ is given by

$$\kappa = -\nabla\cdot\boldsymbol{n} = \nabla\cdot\frac{\nabla\alpha}{|\nabla\alpha|}\,, \tag{3.12}$$

where $\boldsymbol{n}$ is the interface unit normal vector.

3.2.4 Final Form of the Momentum Equation

Before conversion from its continuous to discrete form, several modifications are made to the momentum equation originally presented as equation (3.2). Firstly, the stress tensor $\boldsymbol{\tau}$ is reformulated and expanded; secondly, the modified pressure is introduced into the equation; and lastly, the surface tension model described in Section 3.2.3 is substituted into the momentum equation.

In order to reduce the number of independent variables, the Navier-Stokes equations must be supplemented with an equation that relates the viscous stresses in the fluid to the local strain rate. For an incompressible and Newtonian fluid where viscosity is uniform in all directions (i.e., isotropic), the stress tensor is given by

$$\boldsymbol{\tau} = \mu_{eff}(\nabla\mathbf{U}+\nabla\mathbf{U}^T)\,, \tag{3.13}$$

where μ_{eff} is the effective dynamic viscosity, which will be defined in more detail in the discussion on turbulence modeling in Section 3.2.5.

Substituting the viscous stress tensor into its respective term in the momentum equation and expanding the divergence yields

$$\begin{aligned}\nabla\cdot\boldsymbol{\tau} &= \nabla\cdot\left(\mu_{eff}(\nabla\mathbf{U}+\nabla\mathbf{U}^T)\right)\\ &= \nabla\cdot\left(\mu_{eff}\nabla\mathbf{U}\right)+\nabla\cdot\left(\mu_{eff}(\nabla\mathbf{U})^T\right)\\ &= \nabla\cdot\left(\mu_{eff}\nabla\mathbf{U}\right)+(\nabla\mathbf{U})\cdot\nabla\mu_{eff}+\mu_{eff}\nabla(\nabla\\ &\qquad\cdot\mathbf{U})\\ &= \nabla\cdot\left(\mu_{eff}\nabla\mathbf{U}\right)+(\nabla\mathbf{U})\cdot\nabla\mu_{eff}\,.\end{aligned} \tag{3.14}$$

In a system treated as a single fluid, such as in the VOF method, it is common to solve for what is known as the modified pressure, defined as

$$p^* = p-\rho\boldsymbol{g}\cdot\boldsymbol{x}\,. \tag{3.15}$$

If $\boldsymbol{x}$ is considered to be the depth of fluid above a given point, the modified pressure is essentially reduced to the dynamic pressure, *i.e.*, the hydrostatic contribution is removed from the total pressure. However, since the coordinate system is arbitrary and left to the user to define, it may not strictly follow the definition of dynamic pressure. For this reason, it is also sometimes referred to as the pseudo-dynamic pressure (e.g., Higuera et al., 2013) and is used to simplify the definition of boundary conditions. Taking the gradient of this term yields

$$\begin{aligned} \nabla p^* &= \nabla p - \nabla(\rho \boldsymbol{g} \cdot \boldsymbol{x}) \\ &= \nabla p - \rho \boldsymbol{g} - \boldsymbol{g} \cdot \boldsymbol{x} \nabla \rho \,. \end{aligned} \tag{3.16}$$

Finally, making use of the CSF model (equation 2.11), the reformulated viscous stress term (equation 2.14), and rearranging equation (3.16) for ∇p, the final form of the momentum equation can be assembled. In an inertial frame of reference, it is given by

$$\frac{\partial \rho \mathbf{U}}{\partial t} + \nabla \cdot (\rho \mathbf{U}\mathbf{U}) = -\nabla p^* + \nabla \cdot \left(\mu_{eff} \nabla \mathbf{U}\right) + (\nabla \mathbf{U}) \cdot \nabla \mu_{eff} - \boldsymbol{g} \cdot \boldsymbol{x} \nabla \rho + \sigma \kappa \nabla \alpha \,. \tag{3.17}$$

3.2.5 Turbulence Modeling

An eddy is a coherent rotating structure observed in turbulent flows and can be classified into various length and velocity scales. The largest of which, called energy-bearing or production-scale eddies, are the result of shear generated in the flow through the interaction with some other entity. Once established, there is a cascade of energy to increasingly smaller scales of motion until viscous stresses in the fluid halt the motion entirely. These rotating structures are subject to stretching, warping and combining with one another in complex ways, giving rise to apparently chaotic and random fluctuations in flow properties. The sum total of these interactions is what we call turbulence and, when present, tends to result in increased energy dissipation, mixing, heat transfer, and drag (George, 2013).

The way turbulence is treated in numerical simulations has therefore been an important topic in both research and practical engineering problems. *Direct Numerical Simulation* (DNS), which uses the Navier-Stokes equations to explicitly resolve all scales of turbulence, is one alternative amongst others. This technique bears the most stringent meshing requirements, often demanding a level of computational effort to be impractical for a majority of problems. Next on the list, in terms of accuracy, is a popular method called *Large Eddy Simulation* (LES). In this method, a spatial filtering operation is applied to separate turbulent length scales into two groups. The larger eddies are completely resolved and their effects on the mean flow is simulated directly. On the other hand, the effects of the smaller eddies on the solution are implemented by means of a *Sub-Grid Scale* (SGS) model.

Although methodologies such as LES have been gaining popularity, the so-called Reynolds-Averaged Simulations (RAS) or Reynolds-Averaged Navier-Stokes (RANS) approach remains the most widely used. In RAS models, the flow variables in the Navier-Stokes equations are decomposed into a mean and turbulent fluctuating component. The decomposed variables are then substituted into the Navier-Stokes equations and integrated through time. The motive behind this was to develop a system of equations for which the solution would yield mean flow variables, greatly reducing the required computational effort. However, in the derivation process an additional unknown stress term, called the Reynolds stress, is generated. This gave rise to the famous *closure problem* for which many solutions have been offered but are too numerous to discuss here in detail. Instead, we limit our discussion to a general overview of the RAS models distributed with OpenFOAM.

These RAS models make use of the Boussinesq approximation whereby the Reynolds stresses, and hence turbulent dissipation, are modeled by artificially increasing the molecular shear with what is known as an eddy viscosity. Making reference to the viscous stress term, expressed earlier as equation (3.13), the effective dynamic viscosity μ_{eff} is calculated as

$$\mu_{eff} = \mu + \mu_t \, , \tag{3.18}$$

where μ is the molecular dynamic viscosity and μ is the eddy or turbulent dynamic viscosity.

By using this approximation, the problem of directly simulating the loss in energy due to turbulent fluctuations is reduced to estimating an equivalent theoretical loss caused by an increase in fluid viscosity. The turbulent viscosity ν_t is estimated by solving one of several two-equation turbulence models distributed with OpenFOAM.

3.2.5.1 $k - \epsilon$ model

The standard $k - \epsilon$ model, originally proposed by Launder and Spaulding (1974), parameterizes turbulence into variables: the turbulent kinetic energy, k, and the turbulent dissipation rate, ϵ. Each obey a convection-diffusion equation of the form

$$\frac{\partial \rho k}{\partial t} + \nabla \cdot \left(\rho \mathbf{U} k - \left[\mu + \frac{\mu_t}{\sigma_k} \right] \nabla k \right) = \boldsymbol{\tau} \nabla \mathbf{U} - \rho \epsilon \tag{3.19}$$

$$\frac{\partial \rho \epsilon}{\partial t} + \nabla \cdot \left(\rho \mathbf{U} \epsilon - \left[\mu + \frac{\mu_t}{\sigma_\epsilon} \right] \nabla \epsilon \right) = C_{\epsilon 1} \frac{\epsilon}{k} \boldsymbol{\tau} \nabla \mathbf{U} + C_{\epsilon 2} \frac{\epsilon^2}{k} \tag{3.20}$$

and are solved simultaneously with the continuity, momentum, and phase fraction transport equations. The turbulent dynamic viscosity is given as a function of k and ϵ and is calculated as

$$\mu_t = \frac{C_u \rho k^2}{\epsilon} \, . \tag{3.21}$$

The model coefficients for the RAS turbulence models have been given default values in their respective source codes. However, if the user wishes to override the default values they can be redefined in a sub-dictionary included in the case folder. The default model coefficient values for the $k - \epsilon$ transport equations are

$$C_u = 0.09, \; C_{\epsilon 1} = 1.44, \; C_{\epsilon 2} = 1.92, \; \sigma_k = 1.0, \; \sigma_\epsilon = 1.3 \, . \tag{3.22}$$

3.2.5.2 Other two-equation turbulence models

During the course of this work, several other turbulence models were applied to gauge the sensitivity of the model results. Since they all follow the general framework of the standard $k-\epsilon$ model with the ultimate goal of estimating μ_t, only a brief qualitative description is given here. For a more comprehensive description of the models the reader is referred to the respective references provided.

The Re-Normalized Group (RNG) $k-\epsilon$ model, proposed by Yakhot et al. (1991), is a modified version of the standard $k-\epsilon$ model that better accounts for the effect of different scales of motion on the turbulent diffusion. The analytical derivation results in a modified ϵ-equation containing additional terms and different model constants than those used in the standard model. The refinements most notably increase the accuracy in predicting the behaviour of rapidly strained and swirling flows (Choudhury, 1993).

A different formulation for the turbulent dynamic viscosity, μ_t, was proposed in the realizeable $k-\epsilon$ model (Shih et al., 1995) whereby the previously-constant model coefficient C_u was reformulated as a function of several variables. In addition, a new transport equation for ϵ was proposed which satisfied certain constraints on the Reynolds stresses, consistent with more recent understandings of turbulent flows.

Another popular alternative to the $k-\epsilon$ family of models is the $k-\omega$ model, developed by Wilcox (1988). Here, ω represents the specific rate of dissipation and obeys a slightly different transport equation relative to ϵ, allegedly offering better performance and prediction of flows in near-wall regions.

Menter (1993) suggested a hybrid of the $k-\epsilon$ and $k-\omega$ models which combines the merits of each one into a single turbulence model which was named the Shear Stress Transport (SST) $k-\omega$ model. In this approach, a slightly modified $k-\omega$ model is used to compute the eddy viscosity from the outer edge of the boundary layer down to the wall. Outside of this region, the model behaves similar to the standard $k-\epsilon$ model, thus avoiding some of the shortcomings of the $k-\omega$ model in freestream zones.

3.3 Finite Volume Discretization

The system of continuous PDEs described in the previous section are capable of predicting the behaviour of two fluids in response to any combination of initial and boundary conditions. However, since it is impossible to achieve an analytical solution to this system, several steps must be taken to approximate their solution at discrete points in space and time. All of OpenFOAM's numerical solvers use a finite volume (FV) discretization technique on the considered system and is applied in three steps (OpenCFD Ltd., 2015b):

[1] **Spatial discretization**, whereby the three-dimensional solution domain is subdivided into a number of control volumes, or computational grid cells, at which the PDEs are approximated;

[2] **Temporal discretization**, for which the continuous stream of time stretching from the beginning to the end of the considered frame is split into a finite number of discrete time steps;

[3] **Equation discretization**, transforming the continuous PDEs into a discrete form suitable for approximating at the spatial and temporal coordinates defined in steps [1] and [2].

In the following sections an overview of the FV technique is provided and follows the general approach outlined in the *OpenFOAM Programmer's Guide* (OpenCFD Ltd., 2015b).

3.3.1 Spatial Discretization

Spatial discretization of the solution domain is achieved through decomposing the domain into a number of contiguous control volumes (*i.e.*, share a border without overlapping), forming what is known as the computational mesh. Each two cells are bound by a finite number of flat faces, f, and share exactly one cell-face with each of its neighbors, as depicted in Figure 3.1. Numerical values for variables pertaining to the flow field are computed and stored at cell-centroids in what is known as a collocated arrangement. Directional vector $\mathbf{d}$, which describes the shortest distance between cell-centers P and its neighbour N, and cell-face surface normal vector $\boldsymbol{S_f}$ with a magnitude equal to the surface area of f are stored at cell-face centers. The latter two parameters, $\mathbf{d}$ and $\boldsymbol{S_f}$, are used in the computation of spatial gradients and cell-face fluxes, respectively.

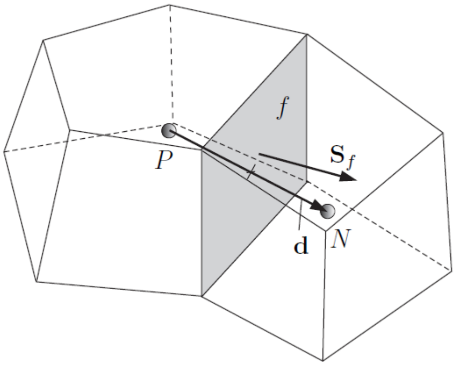

Figure 3.1: Finite volume spatial discretization and associated parameters (OpenCFD Ltd., 2015b)

Temporal discretization is achieved by splitting the considered time frame into discrete time intervals, or time steps, denoted as Δt. Time steps can be either constant or dynamically adjusted during the simulation in order to meet some pre-defined criteria. More details on this are provided in Section 3.4.2.

3.3.2 Discretization of the Transport Equations

To illustrate the transformation of an algebraic equation from continuous to discrete form we consider a generic transport equation for a conservative physical quantity, ϕ,

$$\frac{\partial \rho\phi}{\partial t} + \nabla \cdot (\rho \mathbf{U} \phi) = \nabla \cdot (\Gamma \nabla \phi) + S_\phi(\phi)\,, \tag{3.23}$$

where Γ is the diffusivity and $S_\phi(\phi)$ is a source term.

Expressed in this form, the generic transport equation states that the temporal rate of change and convective transport of ϕ per unit volume is balanced by the diffusive transport and rate of production of ϕ per unit volume.

Finite volume approximations are used to discretize all terms presented in equation (3.23). Of course, the approximations for these terms are not limited to the ones shown in the generic transport equation. For instance, the momentum equation has an additional pressure term with no counterpart expressed here. However, to give a general overview of the FV procedure, we present only the details regarding discretization of the generalized terms in the following sections.

Finite volume discretization of equation (3.23) begins with an integration over the control volume and over time

$$\begin{aligned}\int_t^{t+\Delta t}\left[\frac{\partial}{\partial t}\int_V \rho\phi dV + \int_V \nabla\cdot(\rho\mathbf{U}\phi)dV\right]dt \\ = \int_t^{t+\Delta t}\left[\int_V \nabla\cdot(\Gamma\nabla\phi)dV \right. \\ \left. + \int_V S_\phi(\phi)\, dV\right]dt\,.\end{aligned} \tag{3.24}$$

For discretization of the spatial derivatives, namely the convection and diffusion terms, we make use of Gauss's divergence theorem to transform the volume integrals into an equivalent surface integral. For later use, Gauss's theorem is defined in a generalized form as

$$\int_V \nabla\otimes\phi\; dV = \int_S dS\otimes\phi\,, \tag{3.25}$$

where dS is the differential of the cell-face surface normal vector. The $\otimes$ symbol is used to represent any of the differential operators, *i.e.*, gradient ($\nabla\phi$), divergence ($\nabla\cdot\phi$), or curl ($\nabla\times\phi$).

3.3.2.1 Time Derivative

Discretization of first order time derivatives are performed by integrating over the volume of the computational cell and approximating the resulting term with the Euler implicit time differencing scheme. The implicit Euler method is first order accurate and unconditionally-stable. The approximation is performed as

$$\frac{\partial}{\partial t}\int_V \rho\phi dV \approx \frac{\rho_P^n\phi_P^n - \rho_P^o\phi_P^o}{\Delta \mathrm{t}}V_P\,, \tag{3.26}$$

where subscript P refers to the corresponding value in the cell where the computation is being performed, superscripts n and o refer to the values at the new and previous time step, respectively, Δt is the time step, and V is the volume of the computational cell.

3.3.2.2 Convection Term

The generalized convection term $\nabla \cdot (\rho \mathbf{U} \phi)$ is discretize by first integrating it over the volume of the computational cell and then transforming the volume integral by applying Gauss's divergence theorem. The resulting surface integral is then approximated in discrete form. Applying these steps in order yields

$$\int_V \nabla \cdot (\rho \mathbf{U} \phi) dV = \int_S d\mathrm{S} \cdot (\rho \mathbf{U} \phi) \approx \sum_f \boldsymbol{S_f} \cdot (\rho \mathbf{U} \phi)_f = \sum_f F \phi_f \, . \tag{3.27}$$

The last term on the RHS of equation (3.27) is a simplification made where F denotes the mass fluid flux through the cell face f, defined as $F = \boldsymbol{S_f} \cdot (\rho \mathbf{U})_f$. The subscript f refers to the value at the cell face which requires interpolation between cell-centroids. For more details on the available interpolation schemes the reader is referred to the *OpenFOAM User Guide* (OpenCFD Ltd., 2015a).

3.3.2.3 Diffusion Term

Discretization of the generalized diffusive term is achieved in a similar manner to the convective term. It is first integrated over the volume of the computational cell, transformed into a surface integral according to Gauss's theorem, and approximated as a discrete summation over the cell-faces.

$$\int_V \nabla \cdot (\Gamma \nabla \phi) dV = \int_S d\mathrm{S} \cdot (\Gamma \nabla \phi) \approx \sum_f \Gamma_f (\boldsymbol{S_f} \cdot \nabla_f \phi) \, . \tag{3.28}$$

By removing the diffusivity coefficient out of the dot product, we are assuming it is isoptropic (*i.e.*, not a vector). The gradient at the cell-face, $\nabla_f \phi$, is equivalent to the surface-normal gradient in the case of orthogonal meshes and is calculated as

$$(\nabla \phi)_f^{\perp} = \nabla_f \phi = \frac{\phi_N - \phi_P}{|\mathbf{d}|} \, . \tag{3.29}$$

It should be stressed that this equation holds true only if the condition of mesh orthogonality is met. A mesh is considered orthogonal when the cell-face surface normal vector $\boldsymbol{S_f}$ is parallel to the directional vector $\mathbf{d}$ connecting the cell-centroids P and N (see Figure 3.1). Orthogonality of the mesh can be checked using the *checkMesh* command while inside the case directory. In the case of non-orthogonal meshes, a correction factor should be applied. In the current work, simulations were performed exclusively on orthogonal meshes.

3.3.2.4 Source Term

The generalized source terms, which cannot be expressed as convective or diffusive terms, are first linearized according to

$$S_\phi(\phi) = S_{\phi_1} + S_{\phi_2}\phi \,, \tag{3.30}$$

which has advantages when applying the final time integration in the FV procedure. The S_{ϕ_1} and S_{ϕ_2} terms may themselves be functions of ϕ.

Following linearization, the term is integrated over the volume of the computational cell as follows

$$\int_V S_\phi(\phi)\, dV = \int_V (S_{\phi_1} + S_{\phi_2}\phi)\, dV = S_{\phi_1}V_P + S_{\phi_2}\phi V_P \,. \tag{3.31}$$

3.3.2.5 Time Integration

By substituting equations (3.26), (3.27), (3.28), (3.29), and (3.30) into the generalized transport equation, we arrive at what is commonly referred to as the semi-discretized transport equation

$$\begin{aligned} &\int_t^{t+\Delta t} \left[\frac{\rho_P^n \phi_P^n - \rho_P^o \phi_P^o}{\Delta \mathrm{t}} V_P + \sum_f F\phi_f \right] dt \\ &\qquad = \int_t^{t+\Delta t} \left[\sum_f \Gamma_f \left(\boldsymbol{S_f} \cdot \frac{\phi_N - \phi_P}{|\mathbf{d}|} \right) + S_{\phi_1} V_P \right. \\ &\qquad \left. + S_{\phi_2}\phi V_P \right] dt \,. \end{aligned} \tag{3.32}$$

Although there are several alternatives available for time integration at run-time, the implicit Euler method has been used exclusively throughout the duration of this work. Applying this method to eliminate the continuous temporal integrals and dividing both sides by Δt yields the final form of the discretized transport equation given by

$$\begin{aligned} \frac{\rho_P^n \phi_P^n - \rho_P^o \phi_P^o}{\Delta \mathrm{t}} V_P + \sum_f F\phi_f^n = \sum_f \Gamma_f \left(\boldsymbol{S_f} \cdot \frac{\phi_P^n - \phi_N^n}{|\mathbf{d}|} \right) + S_{\phi_1} V_P \\ + S_{\phi_2}\phi_P^n V_P \end{aligned} \tag{3.33}$$

3.4 Solution Procedure

The fluids considered in the current study obey the Newtonian laws of viscosity and are treated as fully incompressible. As a consequence of the latter simplification, the pressure and velocity become inextricably linked. A change to one variable at a given location in the system will have an instant effect on the other at a different location in the system, independent of the distance of separation. The immediate implication being that the pressure and velocity cannot be de-coupled and must be iteratively solved together throughout the entire system until the solution has converged. One numerical approach to maintain this coupling of pressure and velocity during the solution procedure is the *Pressure Implicit with Splitting of Operators* (PISO) algorithm for transient flows by Issa (1986). A summary is presented here, however, full details can be found in Jasak (1996).

3.4.1 The PISO Algorithm

The PISO algorithm involves application of the following three-step procedure:

[1] **The momentum predictor step**, where the pressure field is borrowed from the previous time step and used in the momentum equation to calculate an approximation of the velocity field. The velocity field at this point will not satisfy the divergence-free condition required for mass conservation in an incompressible flow.

[2] **The pressure solution step**, where the predicted velocities are used to assemble the matrix for the pressure equation which is then solved to obtain an approximate pressure field.

[3] **The explicit velocity correction step**, where the new pressure field is used to compute the new conservative fluxes and the velocity field is corrected to be consistent with the new pressures.

The correction to velocity should consist of two parts – the correction due to the changes in pressure introduced in step [2] as well as the collective influence of the corrections performed on its neighbouring cells. Since the explicit correction neglects the latter part, steps [2] and [3] must be iterated until a pre-define tolerance is achieved.

The transport equation for the phase fraction as well as the turbulent kinetic energy and dissipation rate ($k - \epsilon$) only require to be solved once at the end of the sequence.

3.4.2 Adaptive Time Step Control

To help optimize the use of available computer resources the adaptive time step control feature was applied. In this method, the calculation of Δt is automated and dynamically adjusted after each time step by explicitly controlling the Courant number, defined for an orthogonal mesh as

$$Co = \frac{|\mathbf{U}_f \cdot \boldsymbol{S}_f|}{|\mathbf{d}|} \Delta t\,. \tag{3.34}$$

A physical interpretation of the non-dimensional Courant number is the number of grid cells that a parcel of fluid travels through in a single time step. Often, the stability of the solution is directly dependent on the Courant number. The adaptive time step control feature accepts a maximum allowable Courant number Co_{max} from the user and uses the following expression to calculate Δt

$$\Delta t = \min\left\{\mathit{min}\left[\mathit{min}\left(\frac{Co_{max}}{Co_o}\mathit{\Delta} t_{int}, \left(1 + \lambda_1 \frac{Co_{max}}{Co_o}\right)\mathit{\Delta} t_{int}\right), \lambda_2 \mathit{\Delta} t_{int}\right], \mathit{\Delta} t_{max}\right\}, \tag{2.35}$$

where Δt_{max} can be prescribed by the user if they wish to define an upper limit and Co_o is the Courant number from the previous time step. Damping coefficients λ_1 and λ_2 are applied to avoid oscillatory behaviour of Δt between successive calculations and are equal to 0.1 and 1.2, respectively.

An intermediate value, or best guess, for the time step is evaluated at the beginning of each time step for use in equation (3.35) by

$$\Delta t_{int} = \min\left\{\frac{Co_{max}\mathit{\Delta} t_o}{Co_o}, \mathit{\Delta} t_{max}\right\}, \tag{2.36}$$

where Δt_o is the size of the previous time step.

When the values of the time step are not dynamically adjusted and a fixed value is used instead, the choice of time step must be selected to ensure an accurate solution during the most instability-prone stage of the calculation. This may result in long computation times and inefficient use of the processors. The use of adjustable time steps is an advantageous work-around in this regard and can, in some cases, offer substantial reductions in overall computation times.

4 Bore-Structure Interaction

4.1 Description of the Laboratory Experiments (Nouri et al. 2010 and Al-Faesly et al. 2012)

The experimental portion of the testing program was performed in the *High-Discharge Flume* (HDF) at the *Ocean, Coastal, and River Engineering* hydraulics lab at the *National Research Council Canada* (NRC-OCRE) in Ottawa. The physical configuration described in the following sections were first used by Nouri et al. (2010) to investigate the effect of upstream obstacles and flow constrictions on bore-structure interaction. The work was subsequently extended by Al-Faesly et al. (2012) who performed additional tests aimed at understanding the effect of varying structure cross-sections, upstream mitigation walls, and bore-driven debris impact loading.

In the three sections that follow, details will be provided on the physical dimensions of the wave flume, instrumentation, and initial conditions that are later used for development and analysis of the numerical simulations.

4.1.1 The High-Discharge Flume

Before and after photographs of the modifications made to the HDF to accommodate for the experimental testing program are shown in Figure 4.1(a) and (b), respectively. Full dimensions of the HDF measure 13.17m-long x 2.4m-wide x 1.4m-deep with stainless steel-constructed sidewalls and channel-bottom. The flume is supplied with water at the upstream end by means of a variable-pitch blade pump capable of providing a maximum discharge of 1.7m^3/s. Located at the downstream end is a sluice gate immediately followed by a floor drain leading to a catch basin underneath the facility.

Figure 4.1: The High-Discharge Flume before (a) and after (b) modification for the testing program (Courtesy of NRC-OCRE and Taofiq Al-Faesly)

A sheet metal partition was erected along the longitudinal axis beginning at the downstream end and terminating before reaching the upstream end, leaving a 2.32m-long opening. The first 5.60m of the upstream end was converted into a reservoir using a fixed piece of sheet metal spanning across the flume on one side of the partition, and a swinging gate mechanism spanning across the other. Using this particular configuration, a U-shaped reservoir was established with the intention of maximizing the length of the flow path using the given dimensions of the HDF. The 1.3m-wide section on one side of the partition was used to channel the bores after rapid opening of the reservoir gate via an electric winch and counterweight mechanism. The time it took for the gate to separate from the surface of the water varied from 0.35 to 0.42 seconds, depending on the initial upstream water depth, h_u. In all three considered cases, h_u = 0.55m, 0.85m, and 1.15m, the gate opening time satisfied the criteria outlined by Lauber and Hager (1998) for the release to be considered a *sudden dam-break*. Therefore, the gate opening process was sufficiently fast to have no perceivable consequence on the development of the bores. A schematic of the physical configuration used for the testing is given in Figure 4.2.

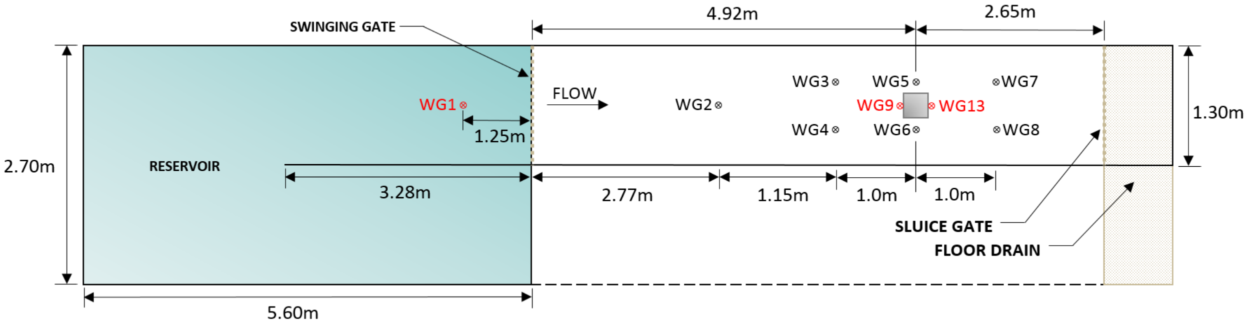

Figure 4.2: General configuration of the High-Discharge Flume

A single model structure analogous to a column or the envelope of an entire building was placed directly in the path of the ensuing hydraulic bores. For this, two cross-sections were considered. The first was a sharp-edged square constructed from four 6.3m-thick Plexiglas sheets standing 1.0m-tall with side dimensions of 0.30m. The second was a 0.70m-tall circular cross-section cut from a section of 0.30m-diameter polyvinyl chloride (PVC) pipe. In both cases, the vertical axis of the structural model was placed directly in the center of the channel, 4.92m downstream of the swinging gate.

4.1.2 Test Procedure

The swinging gate was lowered and locked into position against two vertical steel channels, fixed with rubber gaskets to minimize leakage, welded to the channel walls. The variable-pitch blade pump was engaged to begin filling the reservoir to a specified water depth. As the hydrostatic pressure built up against the gate and the fixed piece of sheet metal on the other side of the partition, minor leakage was observed across the assembly. As the water surface approached the target elevation, the pitch of the impeller blades were adjusted to ensure that at the time of the gate opening the water surface elevation was constant over the preceding couple of minutes. Once this condition was met, the data acquisition system was activated and the electric winch was triggered. At this point, the gate swung open and the vertical column of water, no longer bearing any support, began to collapse and surge towards the downstream end of the flume.

The formation of cross-waves on the water surface were noted during release of the impounded water in the reservoir and can be seen in Figure 4.3. As the water gains velocity travelling past the gate apparatus, there is a tendency for the water to runup on the steel brackets which the gate was initially pressed against in its closed position. As a result, a thin sheet of return flow is generated at the surface which propagates from both sides towards the channel centerline. Since the surface velocity in between the brackets is fastest in the center of channel, the undulation caused by the minor obstruction is transported further downstream before dissipating. Hence, a clear V-shaped surface disturbance emerges.

Figure 4.3: Formation of cross-waves upstream and downstream of the gate apparatus (Courtesy of Taofiq Al-Faesly)

A second set of cross-waves can be seen on the downstream side of the gate, ostensibly occurring from the same process as described above. The exception is that the return flow is generated from the runup on the channel sidewalls after being funneled past the brackets, instead of being generated from runup on the brackets themselves. However, there was no residual evidence of the cross-waves further downstream. Thus, it is thought that the occurrence of the cross-waves did not significantly affect the forces or pressures exerted on the structural model.

4.1.3 Instrumentation

Capacitance-type *wave gauges* (WGs) (Akamina model WP-AOV02-03) were installed to measure variations in water surface elevation over time. It should be noted that two different wave gauge layouts were developed and employed depending on the objective of the test. In total, 13 different locations were used. WG layout 1, consisting of 8 different WG locations, was designed with greater emphasis on spatial variation of water surface elevation and was used during unobstructed flow conditions, *i.e.*, no structural model was present. Using this layout, time-histories of water surface elevation were measured at the location where the structural model would later be installed. In addition, two-dimensionality of the flow could be checked by comparing surface elevation on opposite sides of the channel and bore front celerity could be calculated using the difference in arrival times at WGs separated by a known distance.

On the other hand, WG layout 2, consisting of 6 different WG locations, was designed with greater emphasis on measuring water surface elevation in the vicinity of the structural model after being installed inside the flume. This will herein be referred to as obstructed flow conditions. Using this layout, time-histories of water surface elevation were recorded using 5 WGs mounted immediately adjacent to the structural model on different sides. It should be noted that only some of these locations were considered for comparison to the numerical results, most importantly the runup recorded on the exposed face and WSEs in the wake of the structural model. Locations of the WGs in layouts 1 and 2 can be seen in Figure 4.2, shown in black and red, respectively. The WG installed to record water levels inside the reservoir, WG1, was present in both layouts.

A *six-degree-of-freedom* (6-DOF) dynamometer (AMTI MC6 Series) was bolted to the channel-bottom and was used to record time-histories of the force exerted on the structural model during impact and passage of the hydraulic bores. The structural models were rigidly coupled to the 6-DOF dynamometer through an aluminum frame fabricated and inserted into the bottom of the models. This configuration ensured efficient transfer of the fluid forces exerted on the surface of the structural models to the dynamometer for accurate recordings. A 4 to 5mm gap was left between the bottom of the structural model and the channel bottom to avoid any interaction between the two that would adversely affect the measurements. In order to protect the equipment inside the structural model from water damage the gap was filled with a thin bead of silicone.

Lastly, 10 *pressures transducers* (PTs) (Honeywell 20PC Series) were mounted on the structural model to record time-histories of fluid pressure exerted on the upstream-facing side. The PTs were installed along a vertical line at 5cm intervals starting at the channel-bottom ($z = 0cm$) and terminating at $z = 45cm$. However, due to the physical restraint imposed by the dimensions of the PTs, the lowest one was installed such that measurements were taken at an elevation of $z = 2cm$. For clarity in the sections that follow, individual PTs will be referred to with their elevation in cm

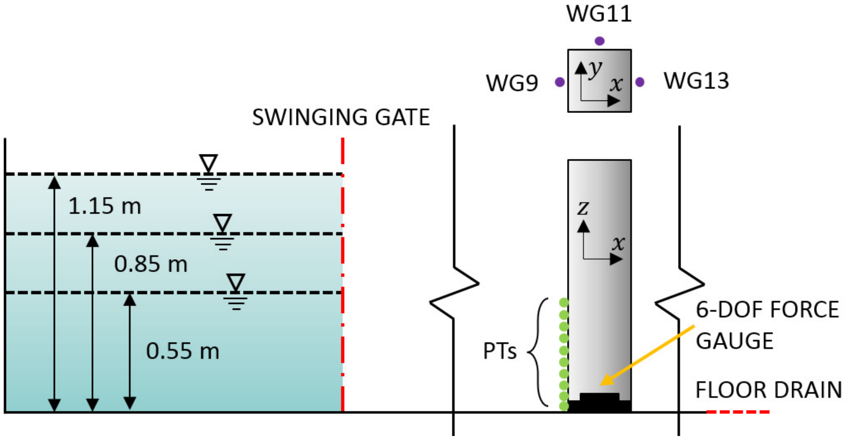

Figure 4.4: Diagram of instrumentation used in the vicinity of the structural model

preceded by PT (*i.e.*, PT2, PT5, … , PT45). A diagram of the instrumentation used in the near-structure region is given in Figure 4.4.

4.2 Description of the Numerical Simulations

4.2.1 The Computational Domain

The full spatial domain enclosed by the flume walls, shown in Figure 4.5, was considered for numerical reproduction of the physical experiments. Since the amount of time for the gate to fully separate from the water surface was sufficient to meet the *sudden dam-break* criteria of Lauber and Hager (1998), numerical simulation of the gate opening was deemed unnecessary and therefore was not performed. Numerical output of the model results for visualization purposes (animations; phase fraction, velocity, and pressure fields) were obtained at a frequency of 20 Hz. However, to capture the highly transient fluctuations in field variables at locations where comparison are made to experimental data, OpenFOAM's run-time post-processing feature was applied. Making use of this feature enables full control of the variable type, spatial location, and frequency of the numerical output for instances where specific and refined results are required. In this way, line sampling of the phase fraction for calculation of the water surface elevation is performed and output every 5 time steps. Fluid pressure at corresponding experimental PT locations and net base shear force exerted on the structure are output at every time step to capture even the most fleeting variations.

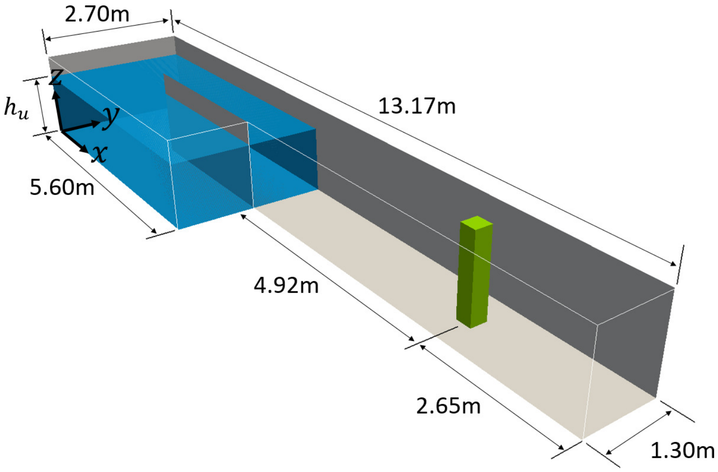

Figure 4.5: Initial configuration for simulating the experiments of Nouri et al. (2010) and Al-Faesly et al. (2012).

Three computational meshes were generated for each of the initial reservoir depths considered. Although the dimensions in the two horizontal directions (x and y, see Figure 4.5) remained constant, the height in the vertical direction (z) was free to optimize for computational efficiency. Since the flow of the liquid phase (which also includes entrainment of the gaseous phase) was of primary interest, the mesh was extruded to remove grid cells that contained only the gaseous phase over the simulated time frame. Using this as a general rule, the height of the mesh inside the reservoir was set equal to initial reservoir depth, h_u. However, in order to avoid adverse interaction between the liquid phase and atmospheric boundary at the top, they were kept separated by the addition of a single layer of grid cells. The mesh in the near-structure region extends across the flume and $0.75m$ upstream and downstream of the structure. The height of the mesh in this region is governed by the maximum splash height (S_{max}) occurring shortly after bore impingement on the structure. The height of the channel section connecting the reservoir and the near-structure region tended to be governed by the height of and upstream-propagating obstruction-induced (O_{max}) wave due to blockage effects in the flume. A diagram of the generalized computational mesh for various h_u is provided in Figure 4.6.

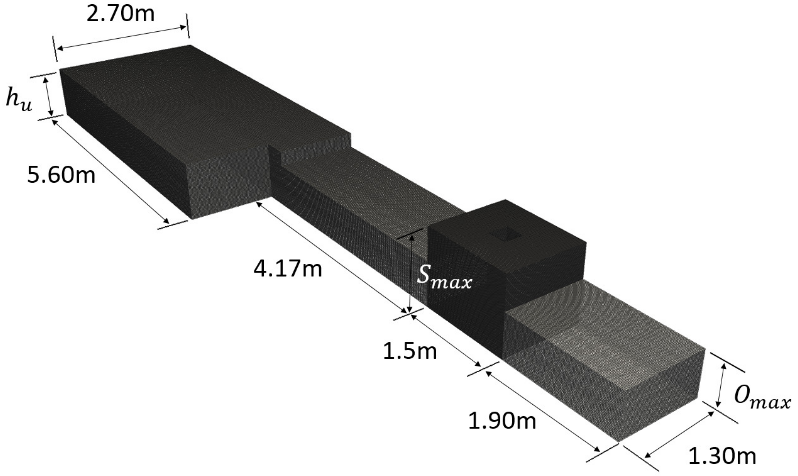

Figure 4.6: Optimized computational mesh generated for the HDF.

4.2.1.1 Initial Conditions

The solution to the transient Navier-Stokes equations requires starting values, or initial conditions, for the field variables being solved. Following mesh generation, the *setFields* dictionary is used to define bounding boxes which targets cells with prescribed values of pressure, velocity, phase fraction, and turbulent quantities.

Before release of the upstream reservoir, the system is at rest and so the choice for initial values is straightforward. The initial values for the velocity and pressure field are set to zero. In the way that the multiphase solvers handle the definition of pressure (see Chapter 3), it is better to think of it as prescribing the dynamic pressure. The total pressure will be automatically calculated during the first iteration based on the prescribed velocity field and distribution of the phase fraction. In VOF simulations, the accuracy of the prescribed and computed water surface elevation is equal to the mesh resolution. If the target water level does not coincide with a set of cell faces, it may be necessary to adjust the thickness of individual layers of grid cells to achieve the desired initial conditions. In the current work, this adjustment was performed in the reservoir and in the downstream channel section for simulations with an initially wet channel bed. If the downstream depth was smaller than the grid cell, the height of the bottom layer was set equal to h_d. On the other hand, if the target downstream depth was larger than the existing grid cell, a layer above the lower-most row was adjusted accordingly in order to accurately define h_d. An Illustration of this is provided in Figure 4.7.

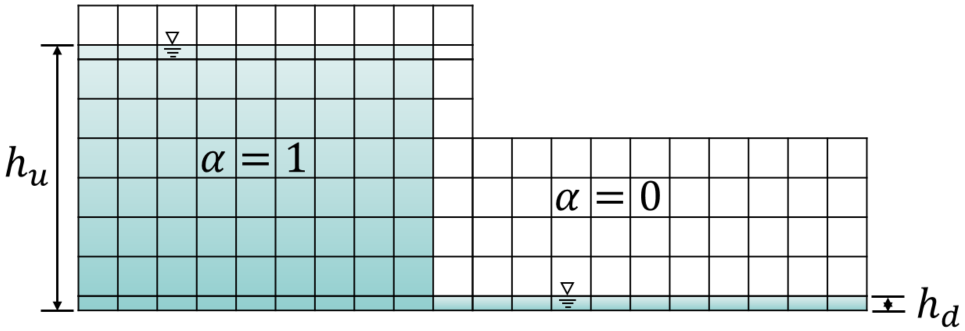

Figure 4.7: Adjustments to cell heights near the surface for accurate prescription of the initial phase fraction distribution.

Convergence of the turbulent quantities can be accommodated by selecting reasonable initial values for the internal field. However, the solution for the turbulent quantities will converge to a given value independent of the initial guess, so the choice is not crucial. Of greater importance, is the turbulent quantities prescribed at inlet or outlet boundaries. However, in the current work, no inlet boundary exists and the flow at the outlet is supercritical. As such, no information regarding the flow travels upstream from the outlet, making the choice for the initial turbulent quantities arbitrary.

4.2.1.2 Boundary Conditions

In addition to the initial values, values for field variables at external cell faces forming the outer limits of the spatial domain must be provided. There are three different boundary-types in the domain considered here: the flume walls, the atmospheric boundary at the top, and the outlet boundary at the downstream end.

On solid walls, a *fixedFluxPressure* boundary condition is applied to calculate the pressure field. This adjusts the spatial gradient of pressure so that the boundary flux is consistent with the boundary conditions prescribed for velocity. Since all three components of the velocity are set to zero at boundary faces (*i.e.*, no-slip condition), the *fixedFluxPressure* essentially reduces to a Dirichlet *zeroGradient* condition, defined as

$$\frac{\partial p}{\partial x_{\perp}} = 0 \,, \tag{4.1}$$

where p is the total pressure. This means that the pressure field is calculated in order to ensure that the spatial derivative normal to the boundary face is equal to zero. Similarly, a *zeroGradient* condition is applied to the phase fraction field. This ensures that there is no flux of phase fraction through solid boundaries and that water levels at the boundary and at the internal field immediately adjacent (in the normal direction) to the boundary are equal. Turbulence parameters at solid boundaries are calculated using a wall function formulation based on law of the wall. A discussion on the calibration and the sensitivity analysis for various wall functions will be conducted in Section 4.3.3.

The atmospheric and outlet boundaries are treated equally. In both cases, the *totalPressure* boundary condition is applied on cell faces where a fixed value for total pressure equal to zero is prescribed. The *pressureInletOutletVelocity* is applied to these boundaries for calculation of the velocity field. This is essentially a *zeroGradient* condition imposed on the velocity that switches between explicit and implicit solution depending on the direction of the flow. At cell faces where the velocity is directed out of the domain, the solution is implicit and value for the velocity on the cell face is iteratively solved in the PISO loop. If the flow is directed inwards, the velocity is given explicitly as the corresponding value from the previous time step of the internal field normal to the inlet.

Phase fraction is calculated on the outlet and atmospheric boundaries using an *inletOutlet* boundary condition. If the flow is directed outwards, the phase fraction is calculated using a *zeroGradient* condition. Conversely, if the flow is directed inwards the phase fraction is given a fixed value of zero. Thus, in order to preserve the divergence-free velocity field, air is allowed to enter through cell faces that behave as an inlet. Turbulent quantities are treated the same as phase fraction with the exception that cell faces behaving as an inlet, turbulent kinetic energy $[m^2/s^2]$ and dissipation $[m^2/s^3]$ are prescribed a small value of 0.1, equal to the initial guess for the internal field.

In addition to the external boundaries mentioned above, an internal boundary was generated using the *topoSet* and *createBaffle* commands to model the partition in the reservoir. For this, a set of cell faces coinciding with the physical location of the partition was converted into a boundary on which values for the field variables, or their derivatives, can be imposed. Since it is expected to behave as any of the other walls, the corresponding conditions as described above were specified.

4.3 Calibration of Numerical Parameters

4.3.1 Mesh Resolution

The separation distance between computational nodes is directly related to the amount of truncation error introduced through spatial discretization. As the size of the three-dimensional computational grid cells decrease, the error is reduced. However, additional discretization error may be introduced in multidimensional flow simulations when the aspect ratio of the grid cells becomes too large (Ferziger and Perić, 2002). Thus, only cubic grid cells with equal side dimensions were considered during calibration of mesh resolution.

The effect of varying grid cell sizes on the streamwise force acting on the column for an initial impoundment depth h_u = 0.85m is evident in Figure 4.8. In general, it is clear that smaller grid spacing produces slightly larger forces at almost every stage during the interaction. It is also clear that the magnitude of the discrepancy between the results is largest at the instant when the bore impacts the structure. This discrepancy tends to decrease until approximately t = 2.5 seconds and remains relatively constant thereafter.

During the first second of interaction (t = 1 – 2 seconds) the force exhibits oscillatory behaviour which is particularly pronounced for the 5x5x5cm mesh. The oscillations are the most dominant feature during this time and tend to drown out any finer details, such as changes in slope or sharp peaks in the force time-history. As the mesh resolution is increased, the oscillations are become

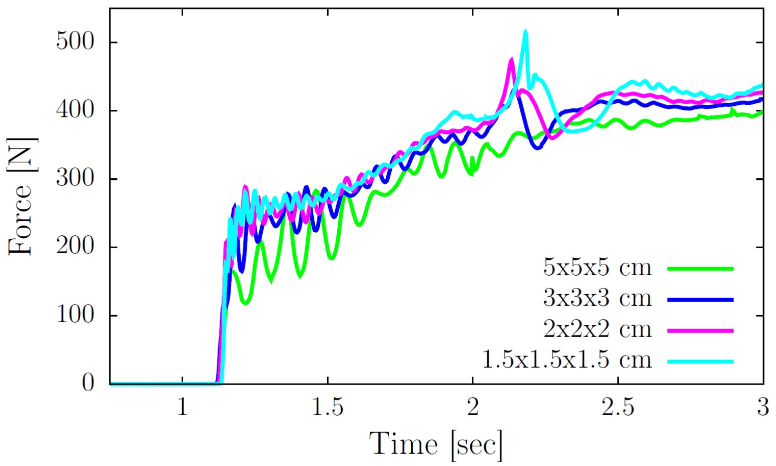

Figure 4.8: Computed time-history of the net base shear force exerted on the structure using various uniform meshes. h_u = 0.85m.

damped and some of the finer details are revealed. One example is a short plateau in the time-history, lasting less than half a second, occurring immediately after the sudden rise in force when the bore impacts the structure. This detail only started to become apparent when the grid spacing was reduced to 3x3x3cm, and became increasingly defined for higher mesh resolutions. Another detail captured by the solution is a short and sudden spike in the force occurring just after t = 2 seconds. Similar to the plateau, this feature in the force signal was revealed only when the grid cells were 3x3x3cm in size or less. Further decreases in grid cell size resulted in a corresponding increase in the magnitude of the spike.

Additional simulations were performed with local refinements applied to the 2x2x2cm mesh in the vicinity of the structure. The first of these meshes was created using a level 1 refinement in a 1.5m-long box centered on the structure and extending the full width and height of the mesh (refer to Figure 4.6). Each level of refinement divides the dimensions of the grid cells by two in each direction. In this case, a level 1 refinement performed on a 2x2x2cm grid cell results in eight 1x1x1cm grid cells. The second locally-refined mesh was created by applying another level of refinement to a 0.75m-longx0.75-wide box centered on the structure and extending the entire height. This final operation lead to a mesh which transitions from 2x2x2cm to 1x1x1cm to 0.5cmx0.5cmx0.5cm grid cells travelling in a direction from the reservoir to the structure. Diagrams of the two refined meshes, 2x2x2 Refined 1 and 2x2x2 Refined 0.5, are provided in Figure 4.9.

Computed time-histories of the force acting on the structure using the two refined meshes are compared to the uniformly distributed 1.5x1.5x1.5cm mesh and the experimental data in Figure 4.10. The numerical time-histories appear to be similar and all show good agreement with the experimental results up until the transient spike between t = 2 – 2.5 seconds. A shift in the duration and arrival time of the increase in force is observed for the mesh refined to 0.5cm grid cells around the structure. Although the numerical model tends to overpredict the magnitude of the transient spike, the experimental data shows a local maximum at approximately the same time. Interestingly, the peaks

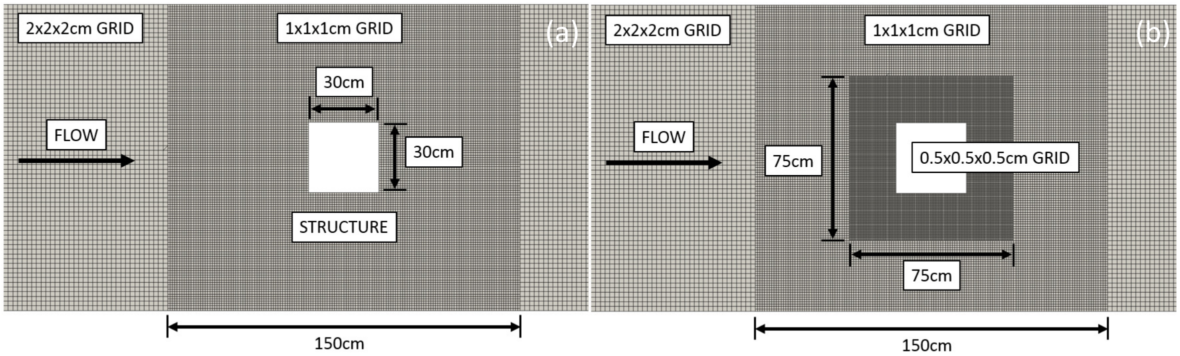

Figure 4.9: Diagram of the refined computational meshes: (a) 2x2x2 Refined 1 and (b) 2x2x2 Refined 0.5.

of the two coarser meshes tend to line up with local maximum of the experimental data more so than the finest mesh. In addition, there appears to be some agreement regarding a short-lived trough in the force immediately following the peak. It seems once again that this detail is more accurately produced by the two coarser meshes considered. However, the subsequent rise in force after t = 2.5 seconds appears to be most closely reproduced by the mesh with the 0.5cm grid cells around the structure. However, Table 4.1 shows that there was a substantial increase in computational time between the two finest meshes tested. For an initial impoundment depth of h_u = 0 .85m, the simulation performed on the mesh shown in Figure 4.9-b cost nearly 6 days of additional computational time compared to the mesh shown in Figure 4.9-a. The same two meshes applied to the largest initial impoundment depth of h_u = 1.15m showed an even greater disparity in the computational times. In fact, the simulation performed with the 0.5cm grid cells around the structure was terminated before the full computation could be completed since it was clear that the computational hardware (most notably the available RAM) was being pushed past its limits. Although the 0.5cm grid cells produced slightly better results than the 1cm grid cells, it was not feasible to use for the remainder of the project due to a limited time frame. For this reason the 2x2x2 Refined 1 mesh was selected to perform the simulations for subsequent investigations.

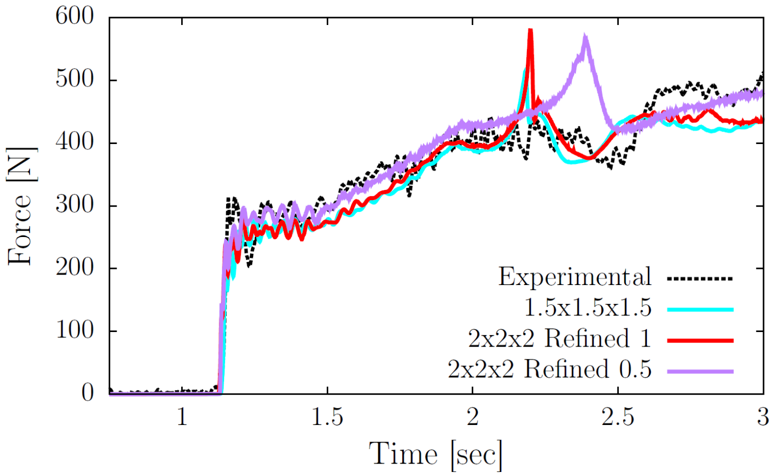

Figure 4.10: Comparison of experimental and computed time-histories of force acting on the structure using various refined meshes. h_u = 0.85m.

h_u (m)	Cell Size (cm)	No. Grid Cells	Computational Time
0.85	5x5x5	169,735	2.6 hours
0.85	3x3x3	785,809	9.47 hours
0.85	2x2x2	3,608,180	1.62 days
0.85	1.5x1.5x1.5	8,468,152	3.79 days
0.85	2x2x2 Refined 1	5,496,080	3.04 days
0.85	2x2x2 Refined 0.5	8,703,596	8.86 days
1.15	2x2x2 Refined 1	7,025,110	5.63 days
1.15	2x2x2 Refined 0.5	10,176,435	>20 days

Table 4.1: Computational details of simulations performed for mesh resolution calibration. Simulation time = 10 seconds.

4.3.2 Turbulence Model

A traditional parameter used for calibrating numerical models to experimental data is the eddy or turbulent viscosity, μ_t. In numerical model developed for the present study, the eddy viscosity is indirectly prescribed by choosing which one of several two-equation turbulence models to apply. The solution to the transport equations for the turbulent quantities are then used to calculate a spatially- and temporally- varying eddy viscosity. The value for this term is then used together with Equation 3.18 and 3.13 to compute the viscous stress tensor in the momentum equation.

To quantify the effect of different turbulence models on the results, the standard $k - \epsilon$, $k - \omega$ SST, and RNG $k - \epsilon$ models were considered. The resulting time-histories of force acting on the structure produced by applying these turbulence models are compared to the experimental data in Figure 4.11. The first significant difference to emerge is the magnitude of the initial force generated at impact. For this, the values for the $k - \epsilon$ and RNG $k - \epsilon$ models are in good agreement with the experimental measurements. However, the $k - \omega$ SST model appears to underestimate the force at initial impact, possibly indicating greater amounts of turbulent dissipation in the bore front. After passage of the bore front, the forces predicted by the $k - \omega$ SST model converge with the other computed values

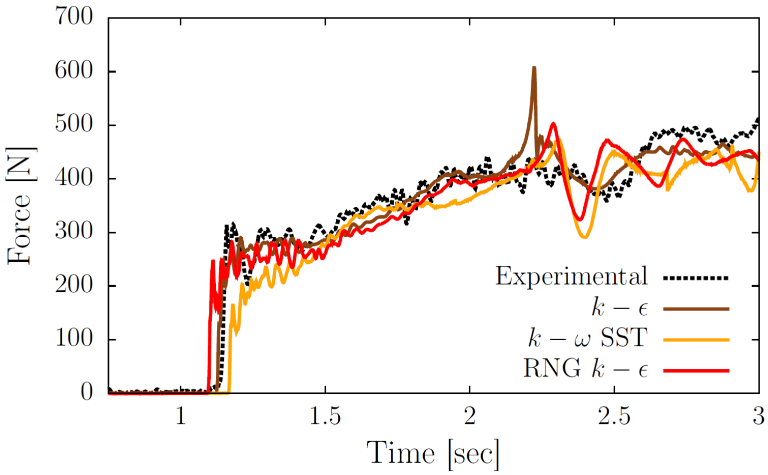

Figure 4.11: Time-histories of force acting on the structure for various turbulence models. h_u = 0.85m.

and appear to be in reasonable agreement with the experimental data. Although the magnitudes of the sharp peak in force at $t = 2.25$ seconds predicted by the $k-\omega$ SST and RNG $k-\epsilon$ model are in better agreement, the subsequent dip in force is overshot in both cases.

None of the discrepancies produced by the models considered here was enough to discount any one in particular. However, the standard and RNG $k-\epsilon$ models appear to have the best overall agreement with the experimental data. Lastly, since the standard $k-\epsilon$ model was the least computationally-expensive of the ones considered here, it was deemed optimal for use in later simulations.

h_u (m)	Computational Mesh	Turbulence Model	Computational Time
0.85	2x2x2 Refined 1	$k-\epsilon$	3.04 days
0.85	2x2x2 Refined 1	RNG $k-\epsilon$	3.97 days
0.85	2x2x2 Refined 1	$k-\omega$ SST	3.40 days
1.15	2x2x2 Refined 1	$k-\epsilon$	5.63 days
1.15	2x2x2 Refined 1	RNG $k-\epsilon$	6.65 days
1.15	2x2x2 Refined 1	$k-\omega$ SST	5.91 days

Table 4.2: Computational details of simulations performed for turbulence model calibration. Simulation time = 10 seconds.

4.3.3 Wall Function

Both smooth and rough wall functions with varying roughness heights, k_s, were considered during the calibration phase. Since the level of agreement between the numerical and experimental data was already established from previous tests, it was decided to use a coarser mesh (2x2x2cm cells) to simply gauge the relative effect of the wall functions. From the resulting time-histories of force presented in Figure 4.12, there are two important distinctions to point out. Firstly, the arrival time of the bore is noticeably affected by the roughness height. In particular, a decreasing bore celerity is observed for

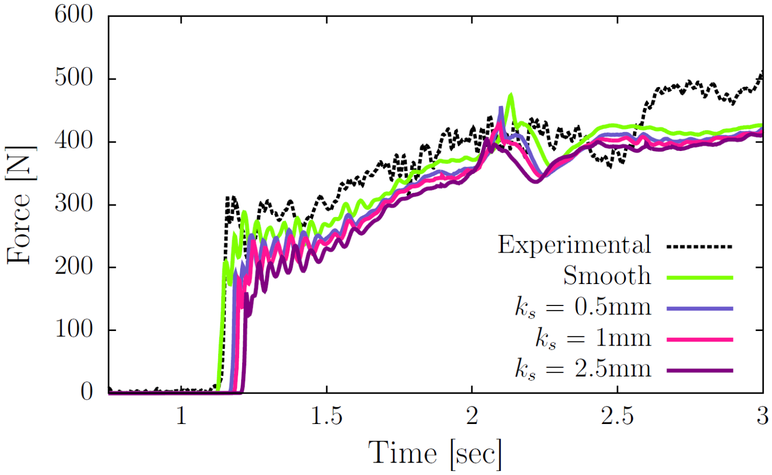

Figure 4.12: Time-histories of force acting on the structure for various wall functions and roughness heights. $h_u = 0.85$m.

increasing roughness height. This observation was expected given that an increase in roughness height should increase the shear stress between the walls and the water, resulting in a slower propagation speed. Secondly, increasing roughness heights appear to yield lower forces. The differences appear to be largest during the early stages of the interaction and tend to decrease over time. By t = 3 seconds the differences in force induced by roughness height is almost negligible. The roughness heights considered here were intentionally inflated, relative to reasonable estimates for stainless steel, to compensate for the lower-than-expected influence it had on the results. Based on the results produced by the optimal mesh, the best-suited wall function and value for roughness height should maximize the amount of force exerted on the structure. Bearing this in mind, the smooth wall function produced the most desirable effects and was therefore selected for use in subsequent simulations.

h_u (m)	Computational Mesh	Turbulence Model	Roughness Height (k_s)	Computational Time
0.85	2x2x2	$k - \epsilon$	Smooth	1.62 days
0.85	2x2x2	$k - \epsilon$	0.5mm	1.71 days
0.85	2x2x2	$k - \epsilon$	1mm	1.75 days
0.85	2x2x2	$k - \epsilon$	2.5mm	1.74 days

Table 4.3: Computational details of simulations performed for wall function calibration. Simulation time = 10 seconds.

4.4 Validation of the Numerical Model: Comparison of Numerical, Experimental and Analytical Results

4.4.1 Water surface elevation

4.4.1.1 Unobstructed flow conditions

Since the pressure and force acting on the structure is highly dependent on the bore profile and its temporal variation, the numerical dam-break-generated bores are first examined under unobstructed flow conditions (*i.e.,* no structural model in place). Figure 4.13 compares experimentally-captured and simulated temporal variations in the water surface elevation at various stream-wise locations in the flume. Considering all four comparisons, the greatest discrepancy occurs inside the reservoir at WG1 (Figure 4.13-a), 1.25m upstream of the gate location. From the trend that is observed in both the numerical and experimental data, it is convenient to divide the time-history into three stages; the beginning and end of which are marked by a change in the rate at which the reservoir drains. Stage one begins when the negative wave, generated by the collapse of the water column after gate removal, arrives at the wave gauge location. At this time, the water surface elevation begins to decline at a relatively rapid rate which appears to be well-matched by the numerical model. The beginning of stage two is marked by a transition to relatively milder decline in surface elevation. The first discrepancy arises as a result from a disagreement between the timing of this transition. In the case of the numerical reservoir, the transition occurs only fractions of a second later. However, due to the rapid decline evident during stage one, that small difference leads to the plateau (t = 1.5 – 3.5 seconds) of stage two occurring roughly 8cm lower than what was observed during the experiments. In addition, the length of plateau of the numerical reservoir appears to be extended, ending approximately 1.5 seconds later relative to the experimental data. The reservoir enters its final stage, stage three, after the rate of the decline in water levels increases once again, gradually leveling off until it has been completely emptied. After t = 5.5 seconds, an approximately constant level of discrepancy is observed between the numerical and experimental data after the experimental surface elevation appears to increase for a brief period after t = 4.5 seconds. It is thought that this increase in water level is due to additional water added to the experimental apparatus by a large supply pipe leading to the reservoir. The volume of water held between the connection and the shut-off valve only begins to drain once the water levels have dropped below the obvert elevation of the pipe. After this has occurred, the effective channel width is increased relative to that immediately downstream, inducing a response reminiscent of an open channel constriction. In addition to this, the discharge capacity of the experimental flume is likely reduced by a small amount owing to the vertical brackets welded to flume walls to which the gate is secured in its closed position. It is thought that the combined effect of these small constrictions produce the constant discrepancy observed at WG1 during the last half of the simulation.

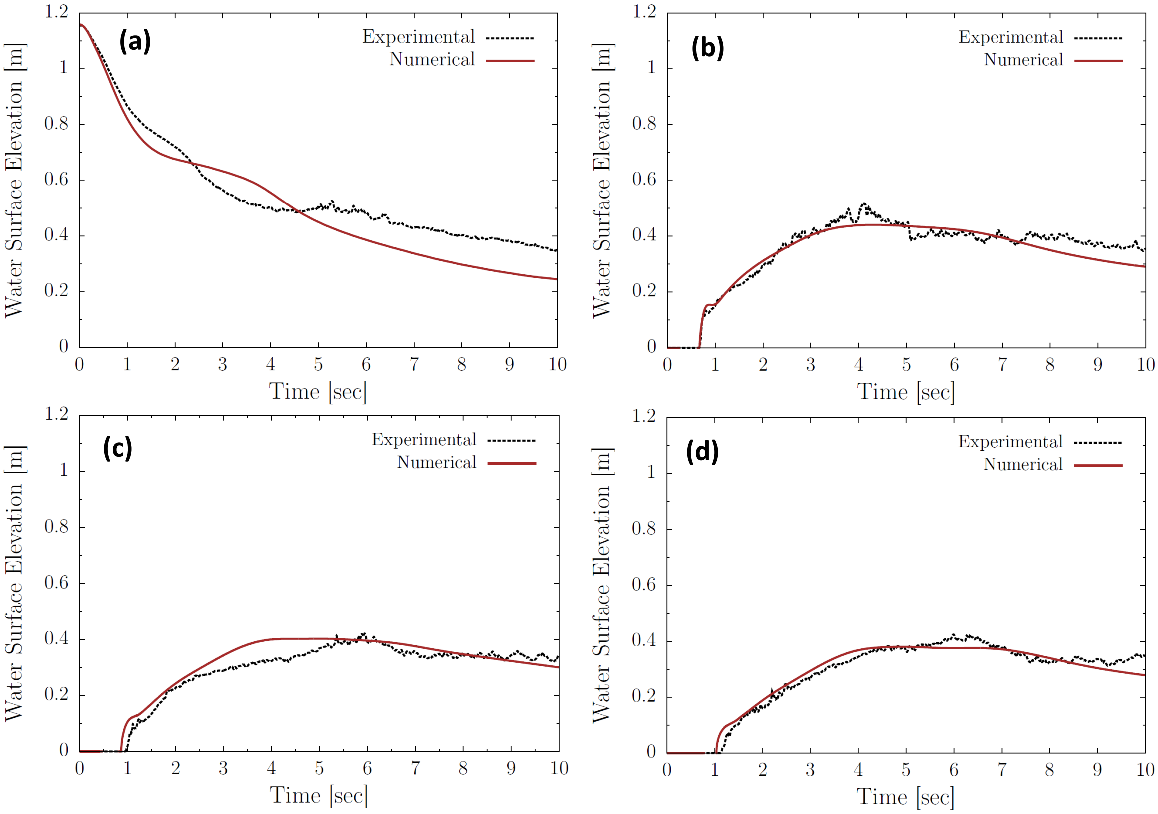

Figure 4.13: Comparison of experimental and numerical time-histories of water surface elevation in an obstruction-free flume (i.e., no structural model) at: (a) WG1; (b) WG2; (c) WG3; (d) WG6. h_u = 1.15.

Aside from the discrepancies observed inside the reservoir, the numerical and experimental water levels elsewhere in flume appear to be in good agreement. Upon arrival of the wave at each gauge, a sharp increase in the water level is observed, indicative of a steep bore-front. In each case, the sharp rise in water level is followed by a transition to a relatively milder slope, lasting for only a brief moment (roughly 0.1 – 0.3 seconds), before increasing at a higher rate until the maximum water level has been reached. It is observed that the sharpness of these transitions, as well as the flatness of the brief moment of mild increase, tends to be most pronounced at locations closest to the reservoir (WG2). This trend in the temporal variations near the bore-front appear to be stretched out and become less pronounced with increasing propagation distance. In fact, the experimental results display the same tendency and has strong resemblance to the phenomenon described by Lauber and Hager (1998) where two distinct waves (initial and dynamic) are generated during the dam-break. The distance separating the two waves is greatest immediately after release. Eventually, the dynamic wave overtakes the initial, causing the apparent blending that occurs as the bore develops.

In Figure 4.14, numerical bore profiles extracted at four discrete points in time for an initial impoundment depth of h_u = 1.15m are compared to the solutions of an analytical formula proprosed by Chanson (2009) (described in Chapter 2). It is clear from examining Figure 4.14 that, in general, the level of agreement between the numerical and analytical bore profiles tends to increase with time. The ideal fluid regions connecting the reservoir and the friction-dominated wave tip region in the analytical solutions are represented by a curved parabola in each case. The wave tip region preceding the ideal fluid is represented by a surface with varying curvature, tending to become steeper as the flow depth decreases. The boundaries between these regions are marked by a sharp discontinuity in the slope of the water surface. In contrast, no such discontinuities are visible in the numerical bore profiles. Although it is possible to roughly distinguish the three different regions, they are connected with a single, smoothly-varying surface.

By t = 1.0 seconds, the numerical and analytical bore profiles are remarkably similar. The location and depth of the surge front are almost in perfect agreement. However, since the analytical solution developed by Chanson (2009) assumes a fully developed bore, it is reasonable to expect substantially larger margins of error during the initialization and development of the dam-break wave. In fact, the relatively sharper transition from the gravity-dominated body of the dam-break flow to the friction-dominated wave tip region observed in the first two still-frames (Figure 4.14-a and b) is thought to be evidence that the bore has not yet become fully developed. The remarkable level of agreement seen in Figure 4.14-c and beyond is of particular interest since the model structure installed during later stages of the study will be placed at x = 10.52m. The results shown here suggest that the bore has sufficient time and propagation distance to become fully developed before reaching the structure location. Thus, concerns about the influence of bore development on the pressures and forces generated at initial impact may be disregarded.

In order to predict to shape of the wave tip at any given time, a Darcy-Weisbach coefficient f must be selected based on the roughness of the surface that the bore propagates over. Although it can be used as a calibration parameter, Chanson (2005) compiled a list of typical flow resistance estimates from best fit data using the diffusive wave equation. Based on the published data, a value of f = 0.03 was used to produce the analytical solutions displayed in Figure 4.14, corresponding to a surface

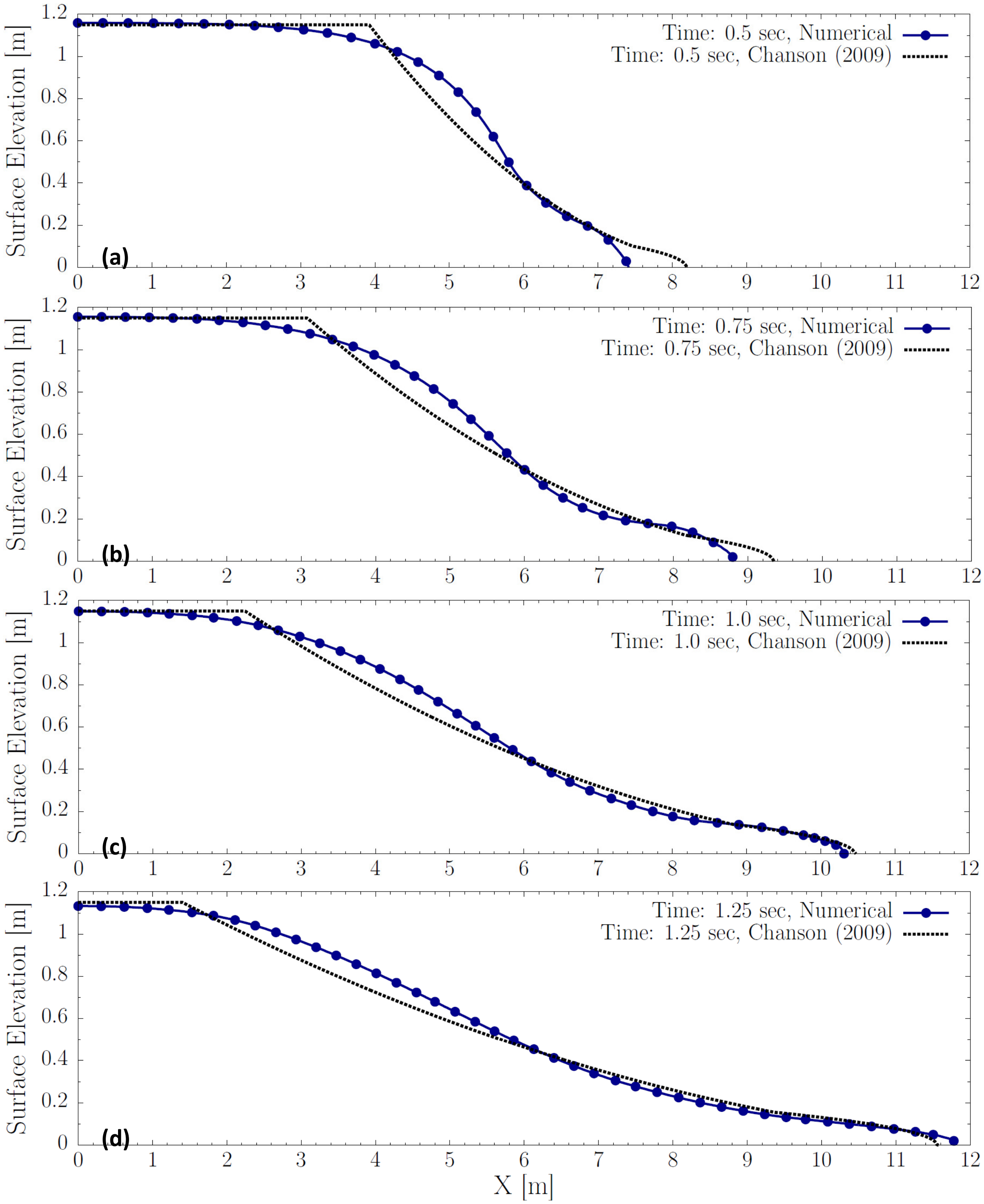

Figure 4.14: Comparison of numerical and analytical bore profiles predicted by Chanson (2009) at (a) Time: 0.5 seconds; (b) Time: 0.75 seconds; (c) Time: 1.0 seconds; and (d) Time: 1.25 seconds after gate opening. h_u = 1.15m.

described as smooth paint with a roughness somewhere in between PVC and sand paper. The value chosen for the roughness will influence the length and depth (*i.e.*, the elevation at which it connects to the ideal fluid region) of the surge front. A close look at Figure 4.14- to d reveals that the steepness the bore front predicted by the analytical model does not vary over time as much as that predicted by the numerical model. As the numerical bore front flattens out under the influence of gravity, there appears to be a corresponding reduction in the steepness, clearly evident by comparing any two of the successive profiles in Figure 4.14.

Figure 4.15 compares the four numerical bore profiles via superimposition, revealing some important spatial and temporal changes in the overall shape of the profiles. The relatively sharper transition from the main body of the dam-break flow to the wave tip region observed in the first two profiles (t = 0.5 and 0.75 seconds) becomes more clearly evident due to the larger distortion of the length scales. Interestingly, all four profiles appear to intersect at the same location, suggesting that there is no temporal variation in the surface elevation at this point, at least until the effects of a depleting reservoir begin to be felt. In fact, a close look at equation (3.3) reveals that this result should be expected. At x = 0m (*i.e.*, the gate location, however 5.6m have been added to the analytical solutions so that the coordinate system is consistent with the numerical solutions), the depth d predicted by the SWE reduces to $(4/9)h_u$ = 0.51m. This is precisely the elevation predicted by the numerical model. However, rather than the intersection occurring at the gate location (x = 5.6m), it appears that is has been translated approximately 15cm in the downstream direction. The reason for this is thought to be owing to the increased discharge capacity of the flume, relative to a straight reservoir which the analytical solution assumes.

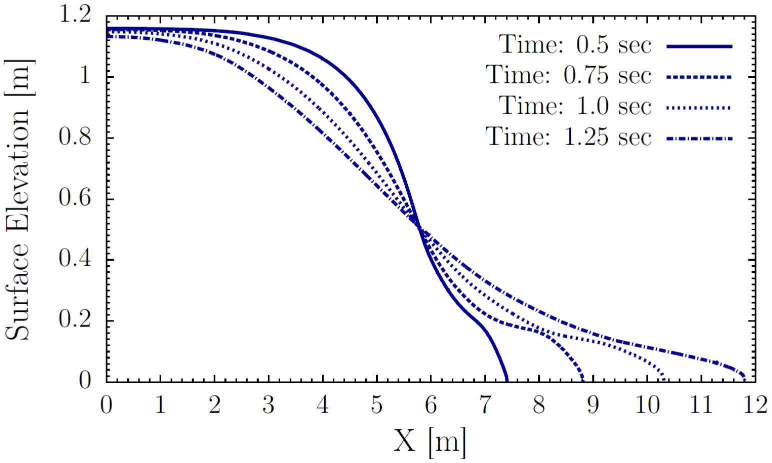

Figure 4.15: Development of the numerical bore profiles over time. h_u = 1.15m.

4.4.1.2 Obstructed flow conditions

Following installation of the structural model, the spatial arrangement of the wave gauges were adjusted in order to capture greater detail of the temporal variations in surface elevation around the structure. The locations of the wave gauges used during obstructed flow conditions are provided in Figure 4.2 (shown in red) and Figure 4.4. Comparisons of the measurements taken at these locations during physical test runs are compared to the corresponding results of the numerical model for each of the initial impoundment depths considered. Where possible, two sets of experimental data are plotted to provide an idea of the inherent variability in the results from test to test.

Figure 4.16 compares numerical and experimental time-histories of water surface elevation measured at WG1, WG9, WG11, and WG13 for an initial impoundment depth of h_u = 0.55m. Water levels in the reservoir measured at WG1 show relatively good agreement, with the numerical time-history falling roughly in between the two experimental ones shown. Notable discrepancy in the trends of the experimental and numerical data first appear at approximately t = 6 seconds. Although the instantaneous value for the surface elevations at this time appear to be in good agreement, the rate at which the numerical surface elevation decreases is higher than the experimentally-measured rates. This discrepancy in the rate at which the reservoir drains eventually leads to the more substantial differences in instantaneous values observed after t = 8 seconds. These differences become particularly pronounced following a momentary increase in water levels as seen in the experimental data displayed as the thicker dashed line. The reason that this is not apparent in the second experimental data set is thought to be related to the apparent increased rate at which the surface elevation decreases in the first two seconds of sampling. Since the experimental data shown as the thicker dashed line appears to decrease substantially faster than its counterpart, the flow restriction effects caused by the presence of the column becomes relatively stronger due to the increased discharge. When the discharge demand of the flume cannot meet the discharge capacity, which repeatedly occurs at the section with the structure, water levels will begin to increase. As the incoming flow drops below critical (Fr < 1), the built-up water trying to bypass the structure finds a new way to equalize the pressure differentials and an upstream-propagating wave is created. Owing to the increased discharge demand in the case of the experimental data shown as the thicker dashed line, this obstruction-induced wave occurs earlier and hence, in this case, appears in the measurements taken at WG1. Although it is not entirely clear from the notes taken during the experimental testing why such a discrepancy appears, it is likely that the test shown as the thicker dashed line was conducted without the flow straightener (visible in the reservoir in Figure 4.1) that was later installed to increase the symmetry of the flow coming around the bend.

Comparisons of water surface elevation measured along the upstream-facing side of the structure at WG9, herein referred to as structure runup, are shown in Figure 4.16-b. The discrepancy observed between the two experimental data sets between t = 1 and 2 seconds highlights the difficulty in properly capturing splash elevations using capacitance-type wave gauges. Since wave probe calibrations are performed in green-water (water not broken up into spray), the change in voltage induced by droplets of water broken up by the initial violent impact cannot be converted into reliable estimates of water surface elevation. In fact, as evidenced by the experimental data shown Figure 4.16-b, sometimes the splash generated during the impact is not captured at all. However, even if a reliable estimate of splash elevation could be provided by the wave gauges, due to the chaotic nature and apparent randomness of the splash they should always be viewed with a relatively higher level of scrutiny. With that aside, and despite the discrepancy between the numerical and experimental splash heights, there appears to be agreement between the arrival time of the bore, and rise/fall time of the initial splash (at least with the one data set that provides splash measurements). At times following the initial splash, there appears to be good agreement between the numerical and experimental data sets for the remainder of the simulation. Perhaps most importantly, the second

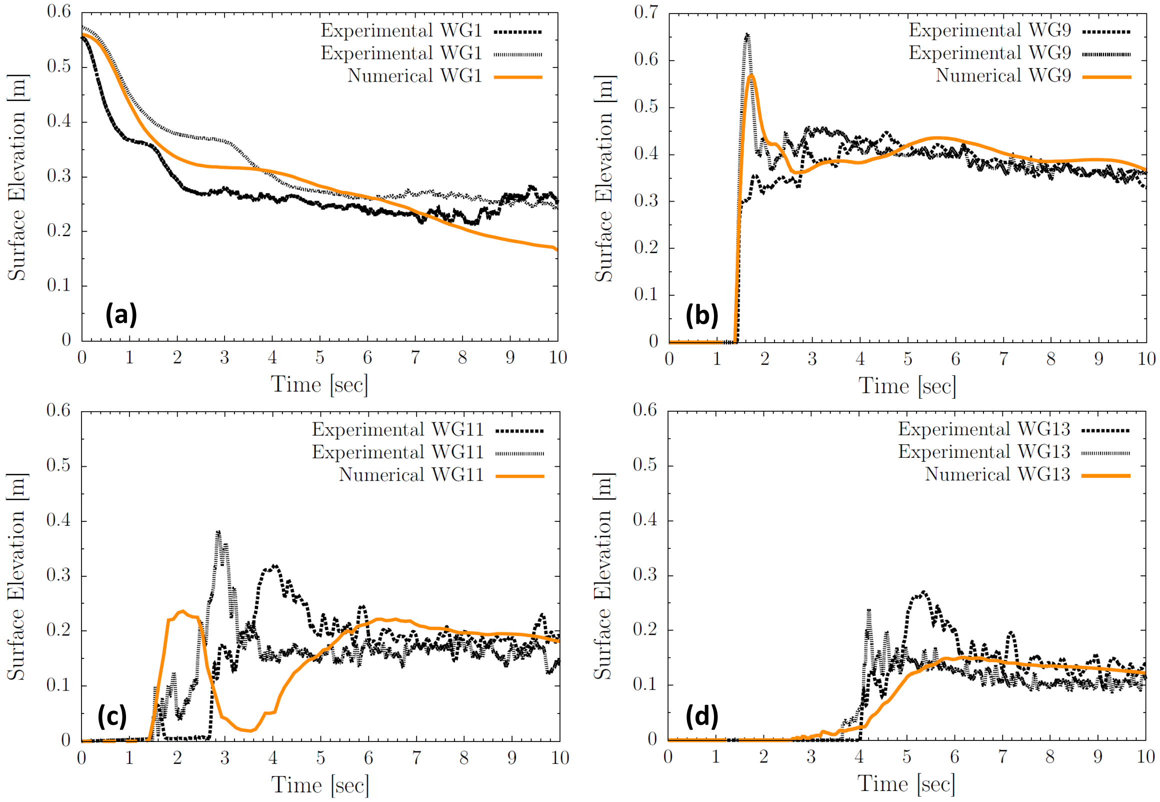

Figure 4.16: Comparison of experimental and numerical time-histories of water surface elevation at (a) WG1, (b) WG9, (c) WG11, and (d) WG13. h_u = 0.55m.

peak in runup that is most easily discerned in the numerical data is only overestimated by approximately 2cm. Since this local peak in the runup occurs in green-water, it is at this time when hydrostatic pressures are greatest at the base of the structure.

Water levels at WG11 (side of the structure) posed the largest difficulties in terms of obtaining good agreement between numerical and experimental results, particularly during the first 5 seconds of the interaction. There is several reasons why this may be true. First, owing to the streamwise momentum of the flow, the splash generated during the initial impact wraps around the sides the structure, contributing to the surface elevation measurements taken at WG11. Again, due to the apparent randomness of the splash and the way that the experimental wave gauges take the measurements, comparisons between the numerical and experimental data during the first couple seconds cannot be expected to provide much insight. The reason for this is because discrepancies observed during this time cannot be reasonably attributed to anything meaningful (*e.g.,* randomness of the splash, measurement error, etc.). Secondly, more error can be expected at this location due to the way that the numerical model handles the problem of turbulence. During the interaction, a wake is generated starting at the upstream-facing side of the structure, creating a “tear-drop” shape with the broad end connecting to the exposed face of the structure and the sharp end terminating at some distance downstream of the leeside of the structure. Because of the lateral diversion of the flow around the column, the sides of the structure actually stay dry for a brief moment during passage of the bore-front. At this time, viscosity of the water plays a large role in how fast the wake closes up. Since the numerical model employs the RANS technique to handle turbulence, the artificial viscosity noticeably reduces the rate at which this occurs. There is evidence of this in Figure 4.16-c between t = 3 and 5 seconds where the experimentally-measured surface elevations are substantially higher than the corresponding numerical prediction. However, after the splash passes and once the wake finally closes up (after approximately t = 5 seconds), the agreement between the numerical and experimental data is quite good.

As can be seen in Figure 4.16-d, the numerical model is able to predict the arrival time and water levels on the leeside face of structure with reasonable accuracy. Since the leeside is protected from the splash that occurs at the exposed face, the relatively higher experimental water surface elevations seen during the first couple of seconds following arrival must be attributed to a different phenomenon. Instead, it is believed these raised surface elevations are caused by converging flow in the wake of the structure. The surface elevations measured during this time may be highly sensitive to the location of the measurement. Since there was no restrictions in the numerical model as to where surface elevation is measured, it was taken directly on the face of the structure. Conversely, due to the physical space restrictions imposed by the size of the wave gauge itself, the experimental measurement may have been taken up to 1 cm off the face of the structure. This, combined with the artificial viscosity added to the numerical system to account for the effects of turbulence provide the most likely reasons for the discrepancy observed in the wake during the first few seconds following bore arrival. Otherwise, after approximately t = 6 seconds fairly good agreement is observed.

Similar levels of agreement between numerical and experimental time-histories of water surface elevation are observed for initial impoundment depths h_u = 0.85m and 1.15m. In the case of water levels measured during the physical testing at WG1, much less variability is noted relative to the initial impoundment depth of h_u = 0.55m. In general, the same discrepancies are observed. Firstly, the maximum discharge capacity of the numerical reservoirs are reached at a slightly later time than its physical analog, indicated by the lower plateau occurring between t = 1.5 and 3.5 seconds in Figure 4.17-a and Figure 4.18-a. After the reservoir depletion effects begin to be felt, the rate at which the surface elevation drops begins to increase once again. As was the case for the initial impoundment depth of h_u = 0.55m, the numerical reservoir appears to drain at quicker rate after the maximum discharge capacity has been surpassed. As mentioned before, it is likely that the discharge capacity of the reservoir is reduced by a small amount owing to the vertical bracket to which the gate is fixed in its closed positon. However, it is also noteworthy that the pumps were left on at a reduced impeller blade pitch to make up for the leakage through the gate and back of the reservoir. Since this additional water added to the system was not accounted for in the numerical model, it may have acted to compound the discrepancy that manifests during the last half of the simulations. However, since the differences observed between the numerical and experimental data at WG1 take time to propagate to the structure location, only in a few cases (*e.g.*, after t = 9 seconds in Figure 4.17-b) do they seem to have a noticeable effect at the structure before the end of the simulation. If the phenomenon of interest took place over longer temporal scales, such as scouring, it may have been necessary to model the components responsible for these discrepancies.

In a few cases during physical tests with an initial impoundment depth of h_u = 0.85m, and all cases with h_u = 1.15m, the impact between the bore and structure was sufficiently violent to disrupt the measurement taken at WG9 during the splash. In these cases, it is reasonable to surmise that the force of the fluid on the wave probe wire was strong enough to press it against the structure, therefore sending faulty voltage readings to the controller. Despite the difficulty in obtaining water surface elevations estimates during the impact, the numerical and experimental runup following the splash, shown for the two larger impoundments depths in Figure 4.17-b and Figure 4.18-b, appear to be in good agreement.

With respect to the water levels measured at WG11 during runs with an initial impoundment depth of h_u = 1.15m (Figure 4.18-c), an interesting deviation in behaviour is observed relative to the two smaller impoundment depths. Instead of displaying a relatively sharp increase in water level, followed by an equally sharp decrease at the beginning of the time-history (characteristic of the splash brushing past the sides of the structure), no such behaviour is evident in the numerical or the experimental data. Rather, it appears that the splash completely bypasses WG11, probably due to the stronger lateral diversion of the flow around the structure upon impacting the upstream-facing side. In fact, in the case of the numerical results, the wake does not begin to close up until t = 3.5 seconds, nearly 2.5 seconds after the bore arrives at the structure. This also roughly true in the case of the experimental results, however there is a brief moment starting at approximately t = 2.5 seconds where the measured surface elevation increases a small amount before falling back down to nearly the bed

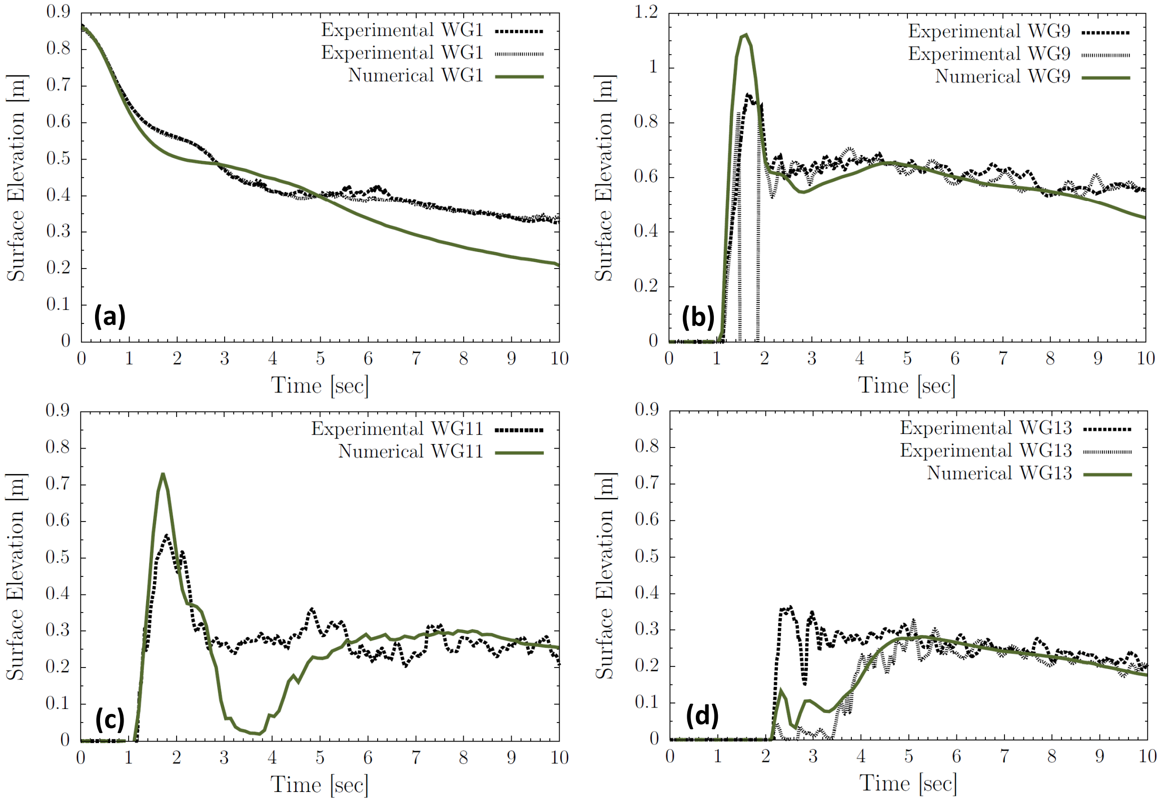

Figure 4.17: Comparison of experimental and numerical time-histories of water surface elevation at (a) WG1, (b) WG9, (c) WG11, and (d) WG13. h_u = 0.85m.

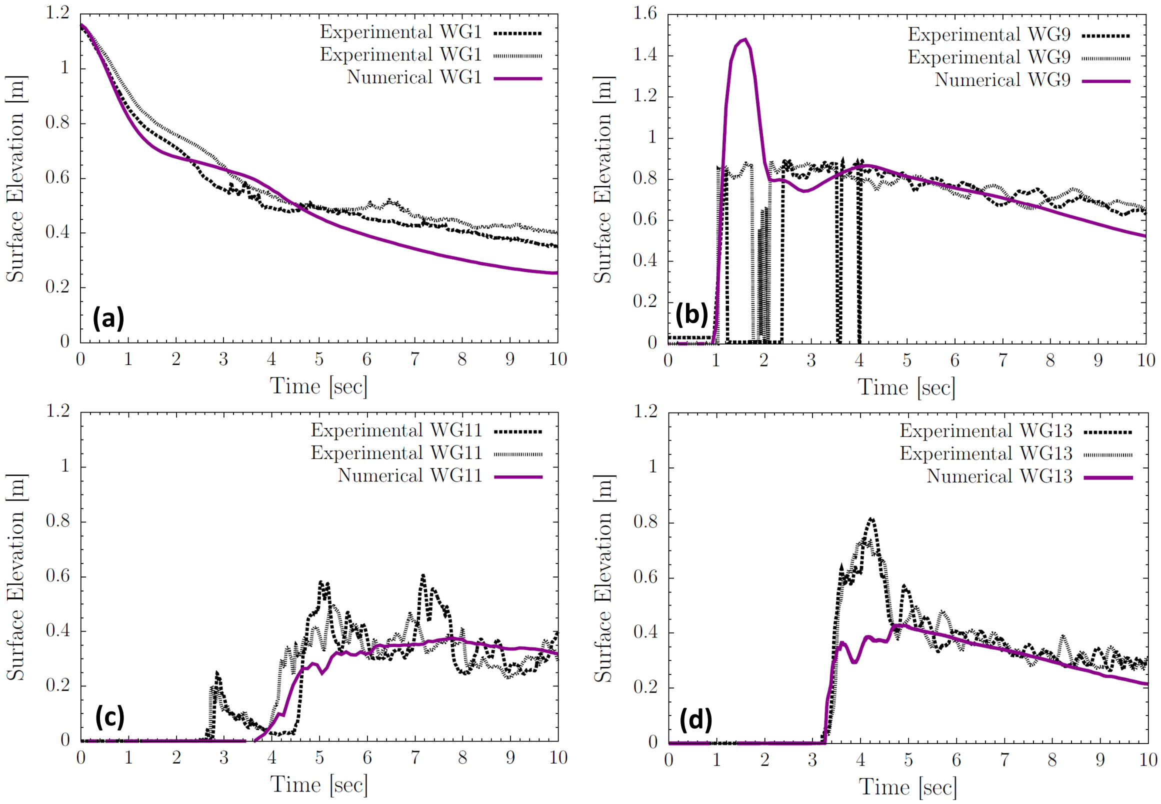

Figure 4.18: Comparison of experimental and numerical time-histories of water surface elevation at (a) WG1, (b) WG9, (c) WG11, and (d) WG13. h_u = 1.15m.

elevation. Although this detail was not captured in the numerical results, the model was able to reproduce the water levels during and after wake closure at WG 11 with reasonable accuracy.

Finally, time-histories of surface elevation measured next to the leeside face of the structure at WG13 for h_u = 0.85m and 1.15m are given in Figure 4.17-d and Figure 4.18-d, respectively. In the case of h_u = 0.85m, the two experimental data sets show substantial variability between t = 2 – 5 seconds. Although it cannot be stated with certainty what the source of the discrepancy is, it is clear that the computed water levels tend to behave very similar to the second experimental data set provided. Conversely, substantially less variability is observed in the experimental measurements at WG13 for h_u = 1.15m (Figure 4.18-d). Although there appears to be some difficulty in numerically reproducing the brief spike in water level occurring between t = 3 – 5 seconds, the remainder of the time-histories are in good agreement. Even though the discrepancy evident for the first two seconds after arrival of the water appears to be substantial, the temporal variation in surface elevation seen in the experimental data indicates strong vertical accelerations. Thus, the higher surface elevation relative to the numerical results likely does not induce any additional hydrostatic pressure that would affect the net shear on the structure.

In addition to the time-histories of surface elevation, a qualitative comparison of numerical and experimental water surface profiles in the vicinity of the structure is shown in Figure 4.19. In this figure, each row of still-frame snapshots represents a particular time, progressing chronologically from top to bottom. The two columns of panels on the left were obtained from the numerical output of interFoam (current study) and SPH (St-Germain et al., 2014), respectively, while the still-frames in the right-most column were taken from a video filmed by Nouri et al. (2011) during a physical test run with h_u = 1.0m. It should be noted that both numerical water surface profiles correspond to an initial upstream depth of h_u = 1.15m since the impoundments depths considered were selected based on the later study of Al-Faesly et al. (2012). Unfortunately, no elevation views of the column during the physical testing were captured in the latter study, however, a meaningful comparison can still be made.

In Figure 4.19-a, shortly after the violent impact of the surge-front with the structure, the water ejected upwards that forms the initial runup tongue, or splash, reaches its maximum elevation. The curvature of the runup tongue pointing back towards the reservoir in the opposite direction of the flow signals the tendency of the wave to be reflected off the structure before collapsing back down under the influence of gravity. Furthermore, both numerical models display the same tendency observed during the physical testing for the splash to be carried around the sides of the structure with the momentum of the flow (which is why, particularly for the two smaller impoundment depths, a short-lived increase in water level is observed at WG11 shortly after impact). Although both models do well in reproducing some of these notable aspects, some discrepancies are also observed. For example, the total volume of water ejected upwards during the impact predicted by the interFoam model appears to be substantially greater than what can be seen from the corresponding experimental still-frame. In addition, the hydrodynamic break-up of the water surface into droplets predicted by interFoam is not quite as extensive. However, the height and overall shape of the splash computed using interFoam appears to be replicated quite well. In the case of the SPH model developed by St-Germain et al. (2014), the hydrodynamic break-up of the surface in addition to the height of the splash appears to be substantially underestimated. The root cause of both of these apparent discrepancies is likely the excessive numerical viscosity induced by the combination of a relatively coarse particle resolution and the application of a Riemann solver to control instabilities in the pressure field, as noted by St-Germain et al. (2014). However, a smaller scale test was conducted in a preceding study by St-Germain (2012) where the available computational resources could afford a finer particle resolution which seemed to remedy the issue.

The water surface profiles displayed in Figure 4.19-b correspond to a time shortly after the water ejected upwards during the impact collapses back down onto the incoming flow. The runup on the face of the structure inevitably returns to the oncoming flow creating a zone of recirculation near the surface. Eventually, this surface roller wraps around the sides of the column, creating a coherent fluid structure resembling a "bow-wave" that forms at the front of a marine vessel moving through the water. At the time shown in Figure 4.19-b, the surface roller is initially very steep as it becomes compressed in the streamwise direction due to the relatively fast incoming flow velocity pressing it against the structure. At the same time, diversion of the flow with a strong cross-stream velocity component forces the water to runup on the flume sidewalls, clearly visible in the interFoam and experimental still-frames. Since the flow velocity is relatively fast and the water depths are shallow, the two streams of water split by the presence of the column converge behind the wake, creating a raised fountain-like structure sometimes referred to as a "rooster tail". The rooster tail is clearly visible in both the interFoam and experimental still-frame. However, the same fluid structure was never observed in the SPH model which was likely damped out by the excessive numerical viscosity.

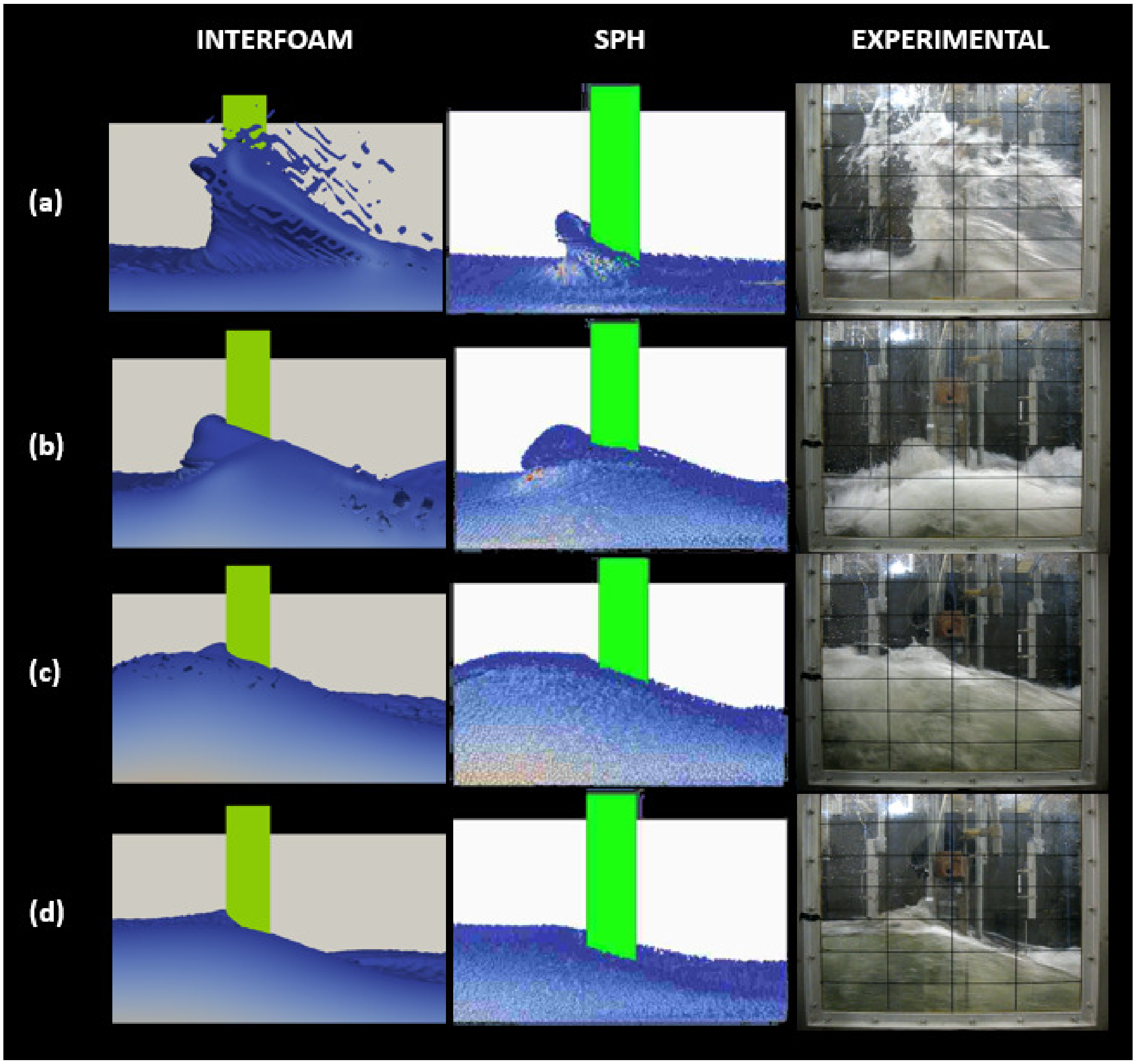

Figure 4.19: Qualitative comparison of InterFoam (current study), SPH (St-Germain et al., 2014), and experimental (Nouri et al., 2010) water surface profiles around the structure at (a) 1.5 seconds, (b) 3.0 seconds, (c) 4.0 seconds, (d) 7.0 seconds. Numerical (InterFoam and SPH) h_u = 1.15m. Experimental h_u = 1.0m.

As time progresses, the flow restriction caused by the presence of the column results in the cumulative build-up of water at the front of the upstream-facing side of the structure. As a result, the surface roller begins to extend across the flume as well as in the upstream direction as the incoming flow velocity decreases. By the time shown in Figure 4.19-c, the strength and visibility of the surface roller has been significantly reduced and the accumulation of water at the front of the structure has noticeably increased the water depths. Without the presence of the strong vertical accelerations characteristic of the surface roller, the hydrostatic pressure at the base of the structure is greatest around this time.

Once the flow velocity has dropped below the critical threshold ($Fr < 1$), the rate at which the build-up of water at the front of the structure propagates upstream increases dramatically. Figure 4.19-d displays a set of still-frame snapshots at a time following the release of the obstruction-induced wave. At this time, the flow has become much calmer and the effects of the depleting reservoir begin to reach the structure location. Flow acceleration through the openings on either side of the column is still evident by the decreasing surface elevation in both numerical still-frames which show good agreement with the corresponding experimental snapshot.

Similarly, a qualitative comparison of the numerical water surface obtained using interFoam is made with the corresponding experimental snapshots in the wake of the structure, given in Figure 4.20. It can be seen in Figure 4.20-a that the single stream of incoming flow is split into two distinct jets on either side of the structure. A substantial portion of the "missing" fluid between the two jets constitutes the splash that can be seen rising along the upstream-facing side of the structure. As a result of the unbalanced pressure gradient in the cross-stream direction, fluid from the two jets begin to converge toward the centerline of the flume. Shortly after passage of the bore-front (~0.5 seconds), the converging jets make contact at a point downstream of the leeside face and the remainder of the wake closes up. At the time shown in Figure 4.20, the beginnings of a rooster tail (as previously described) can be seen in the wake and forms a raised line along the centerline of the flume. Initially, the rooster tail is relatively thin (only a fraction of the width of the structure) and appears to maintain roughly the same dimensions until it merges into the flow further downstream. The experimental still-frame at the same time shows similar characteristics, although the contrasting colours used in the visualization of the numerical results makes it more easily distinguishable.

At t = 3.15 seconds, shown in Figure 4.20-c, the runup tongue generated at impact has collapsed and a well-developed horseshoe-shaped surface roller wrapping around the structure can be seen. The high stagnation pressure at the upstream-facing side of the structure forces the incoming flow to convert some of its streamwise momentum into a cross-stream velocity component in order to bypass the structure. At this time, the effect is quite strong, creating a small cavity along the sides of the structure. From this angle, the runup on the sidewalls of the flume is clearly evident and is the first visible symptom of blockage effects present in the flume. The shape of the numerical rooster tail has undergone a few changes and shows good agreement with the evolution of its physical counterpart. Since the previous still-frame, the rooster tail has reduced in height and broadened in width to nearly match the side dimensions of the structure.

By the time shown in Figure 4.20-d, the horseshoe-shaped surface roller has been mostly submerged by the accumulating water at the front of the structure and is no longer visible from this angle. The surface profile is, for the most part, consistent across the flume and the obstruction-induced wave has begun to slowly advance in the upstream direction. A close look at the front of the wave reveals a choppy texture which is characteristic of a hydraulic jump, indicating that the incoming flow is still supercritical ($Fr > 1$). Once the subcritical condition has been met, the speed of the advancing wave increases substantially and transitions into a more stable wave form with a smooth face. Interestingly, the rooster tail in the wake has evolved into clear a triangular shape, broadening in width with increasing downstream distance. The corresponding experimental snapshot appears to display the same behaviour, albeit with an additional surface pattern that could only be caused by unstable vortex shedding in the wake.

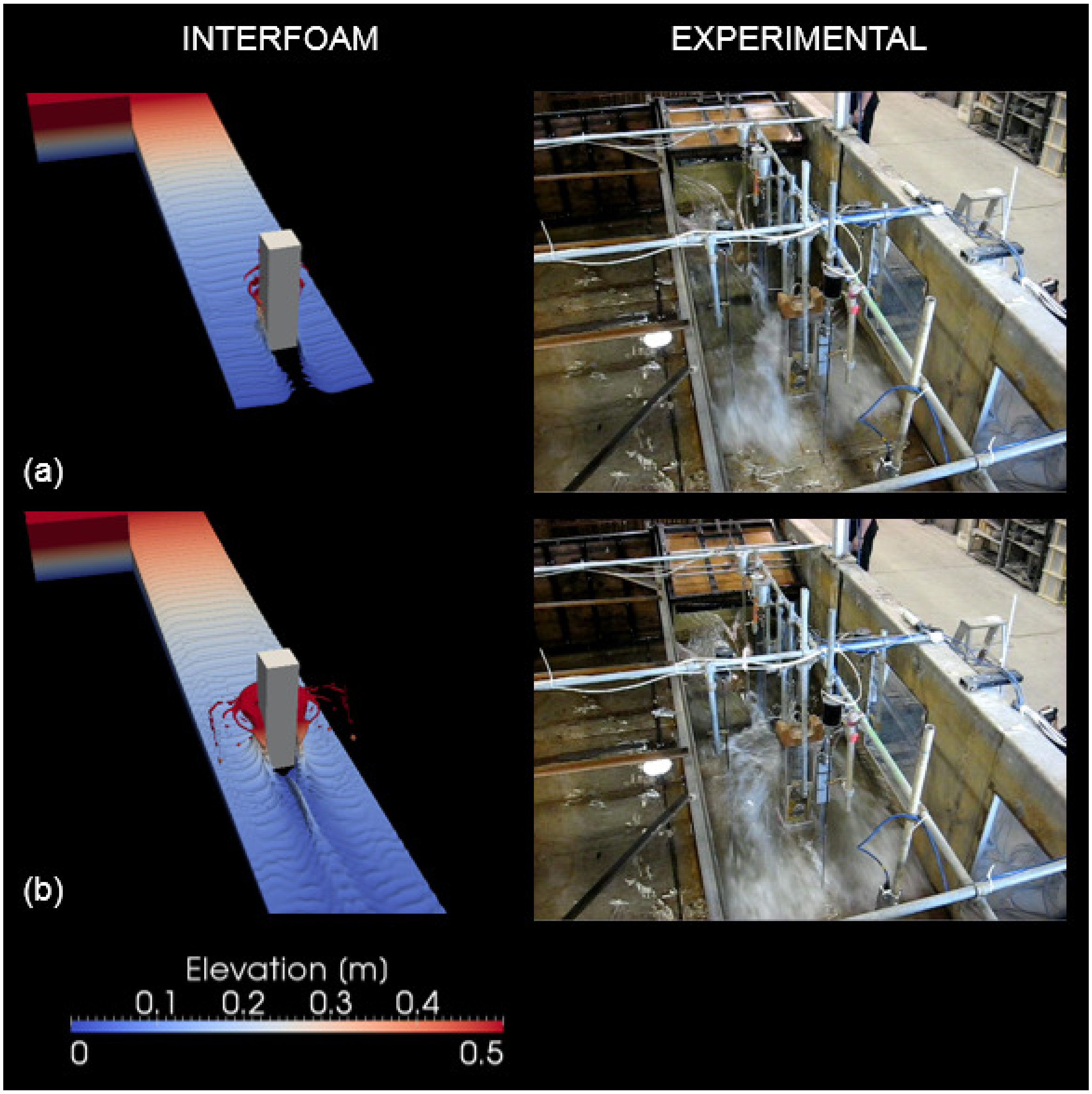

For caption see following page.

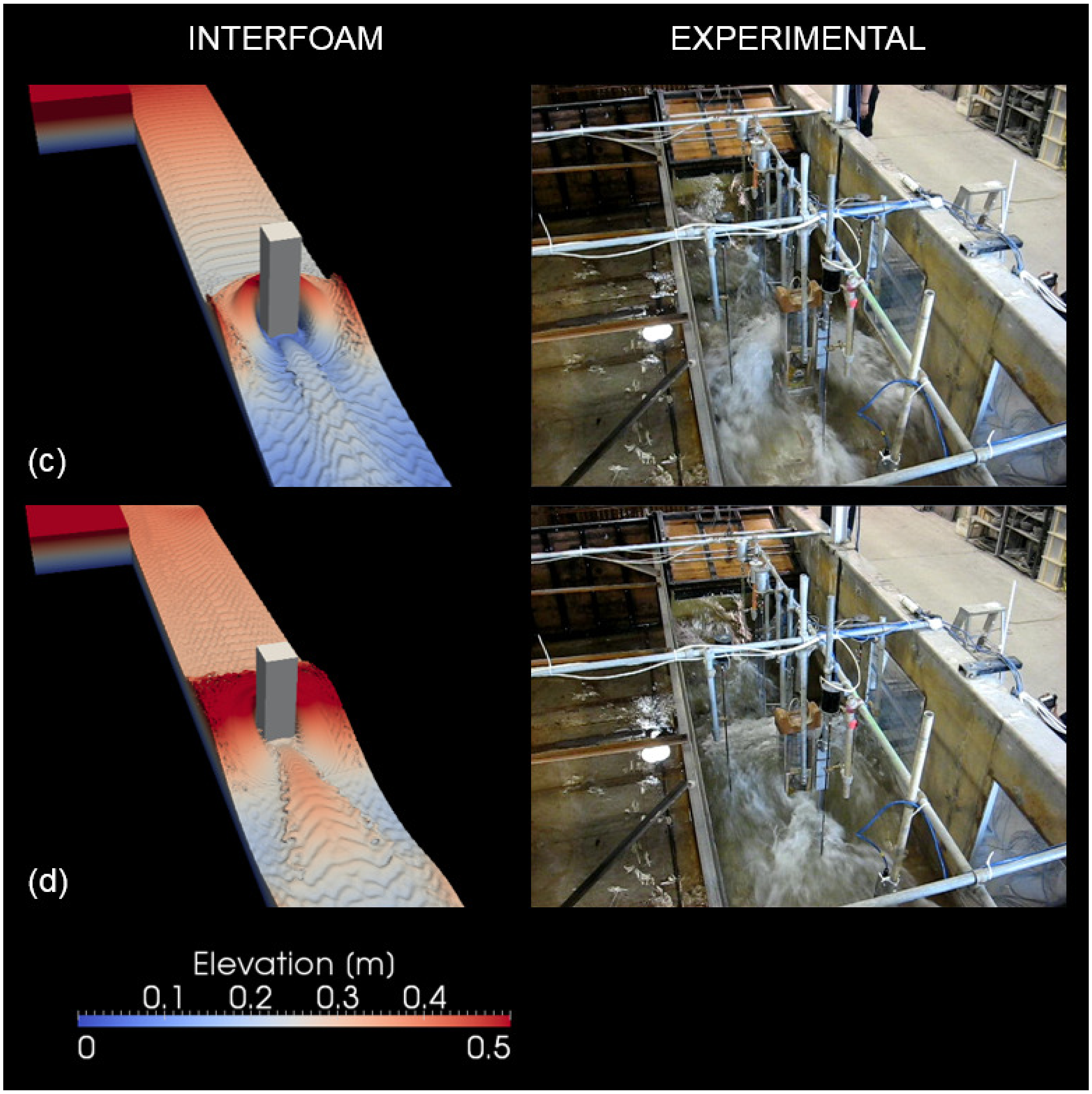

Figure 4.20: Qualitative comparison of numerical (interFoam) and experimental water surface in the wake of the structure at (a) 1.35 seconds , (b) 1.95 seconds, (c) 3.15 seconds, and (d) 5.0 seconds. h_u = 0.85m.

4.4.2 Pressure

Pressure data collected by the transducers along the upstream-facing side of the structure during a run with an initial reservoir depth of h_u = 1.15m is compared with the corresponding simulated values in Figure 4.21. It can be seen that the magnitude of the initial sharp increase in pressure upon impingement of the bore appears to be overestimated for the two lowest pressure transducers (Figure 4.21-a and Figure 4.21-b). After a small fraction of a second later, and in the case of all the pressure transducers at higher elevations, good agreement is observed between the numerical and experimental data.

With regard to the observed discrepancy at the two lowest pressure transducers, the sampling rate used to acquire the datasets may play an important role. At the arrival time of the hydraulic bore during the numerical simulation, the pressure was being sampled at every time step. Since the fluid velocities are relatively high at this time, the adjustable time step is small in order to keep the maximum allowable Courant number under the accepted value (in this case, Co_{max} = 0.9). These conditions resulted in a sampling frequency of the numerical pressure at approximately 1450Hz. Compared to the experimental sampling frequency of 200Hz, the temporal resolution of the numerical data is substantially higher, allowing much smaller transient fluctuations to be captured. However, when examining the numerical data, it was noticed that over a time span of 0.005 seconds (200Hz), the pressure fluctuations were never greater than 5kPa. Although experimental data regarding the same consideration could show different results, the latter suggests that the sampling frequency may play some role in the observed discrepancy (approximately 14kPa), but is likely not the only factor. Since the magnitude of the impulsive pressure generated upon collision of the bore-front with the structure shows strong dependence on elevation, another influential factor may be something as simple as slight differences between actual and reported elevation of the pressure transducers.

In addition to the possible sources of the discrepancy discussed above, a pertinent point regarding the compressibility of the fluids should be raised. Since the bore-front is highly turbulent and entrains significant amounts air, in reality, the compressibility of the air-water mixture increases while the density decreases (relative to pure water). It is known that both of these factors work together to diminish the impulsive pressures as well as to increase the duration of the impact, or rise and fall time of the initial spike in pressure (Peregrine, 2003). A key factor in this “cushion effect” is that the small air pockets trapped inside the water take time to compress, diverting some of the energy in the process. In the current numerical model, air is treated as incompressible and therefore is not able to reproduce any affects related to an increase in mixture compressibility. However, since the amount of time it takes for the air pockets to compress is such an important factor, and temporal scales can vary depending on the spatial scale of the experiment, some other studies bring into question how great of an effect mixture compressibility has in scaled-down models. For example, Bullock et al. (2007) have noted that the compressibility of air may become less important at laboratory-scales compared to its full-scale counterpart. The reason for this is because when the impact duration becomes closer to or smaller than the oscillation period of the entrapped air pockets (alternating expansion and contraction), the time scale may be too small for any meaningful diversion of energy required to compress the fluid mixture. Thus, the cushioning effect offered by the entrained air may be a less dominant effect at smaller scales. Although these qualitative observations offer some potential sources of the discrepancy, a model accounting for the compressibility would be required to quantitatively assess the magnitude of the influence it exerts.

In a few instances, particularly Figure 4.21-f and Figure 4.21-g, there is a brief period at the beginning of the time-history where relatively substantial negative pressures develop on the structures exposed face. At the time when the pressure reaches its minimum value, it can be seen from Figure 4.18-b that the runup on the structure from the initial impact is nearly reaching its peak elevation. Since the fluid will tend to follow the path of least resistance during its descent back down, the runup peels off the face of the structure and creates a momentary void in its wake, resulting in the negative pressure. The numerical model does not appear to predict the same behaviour, owing entirely to the fact that both fluids are modeled as incompressible materials. Since the continuity equation imposes a divergence-free velocity field, any attempt to create a vacuum will be instantly balanced by the solution with an influx of fluid. Without the temporal term in the continuity equation that would allow for density changes, there is no way to replicate the negative pressures that manifest along the structure at higher elevations.

The quasi-steady pressures, characterized by the relatively constant magnitude following the initial impact, predicted by the numerical model show good agreement with the experimentally-measured values at all elevations (Figure 4.21-a through Figure 4.21-h). The one exception, appearing at all elevations, is that the numerical time-history appears to fall below the experimental after approximately t = 8 seconds. As was mentioned earlier in the discussion of the time-histories of surface elevation, the cause of this discrepancy is almost certainly related to additional water in the physical apparatus, added by the pump during the tests to compensate for the leakage. Since the additional flow was relatively minimal, the effects of this are imperceptible during the first 8 seconds. However, since the pump was continuously adding water over the course of the physical test, the time at which the effects of the depleting reservoir arrive at the structure were shifted ahead. Hence why the experimental pressure tends to maintain its quasi-steady trajectory while the numerical results fall off near the end.

To see how the velocity field affects the vertical pressure distribution, the computed values are compared to an equivalent hydrostatic distribution calculated from the numerical runup on the structure in Figure 4.22. The pressure profiles were obtained from a simulation with an initial upstream depth h_u = 1.15m and are plotted at four different moments during the bore-structure interaction. Since these pressure profiles were obtained via post-processing (*i.e.*, after the simulation was complete), rather than sampled during run-time, they were only available at a temporal resolution of 20 Hz, or every 0.05 seconds. As a result, the maximum impulsive pressure generated (~34kPa from Figure 4.21-a) was not captured. Instead, the profile given in Figure 4.22-a at a time small fractions of a second after impact, represents the maximum impulsive pressure captured using a sampling frequency of 20Hz (as opposed to ~1450Hz used to generate the time-histories provided in Figure 4.21). It is clear, however, that the total or simulated pressure exceeds the hydrostatic pressure by a substantial margin, more so than at any other time during the interaction. In fact, the total pressure at the given time is nearly 7 times greater than the hydrostatic pressure computed from the numerical runup on the structure. The high impulsive pressure given in Figure 4.22-a rapidly declines to a value less than hydrostatic with very small increases in elevation. As a result, an extremely high pressure gradient is generated in the vertical direction which accelerates fluid upwards and creates the violent splash.

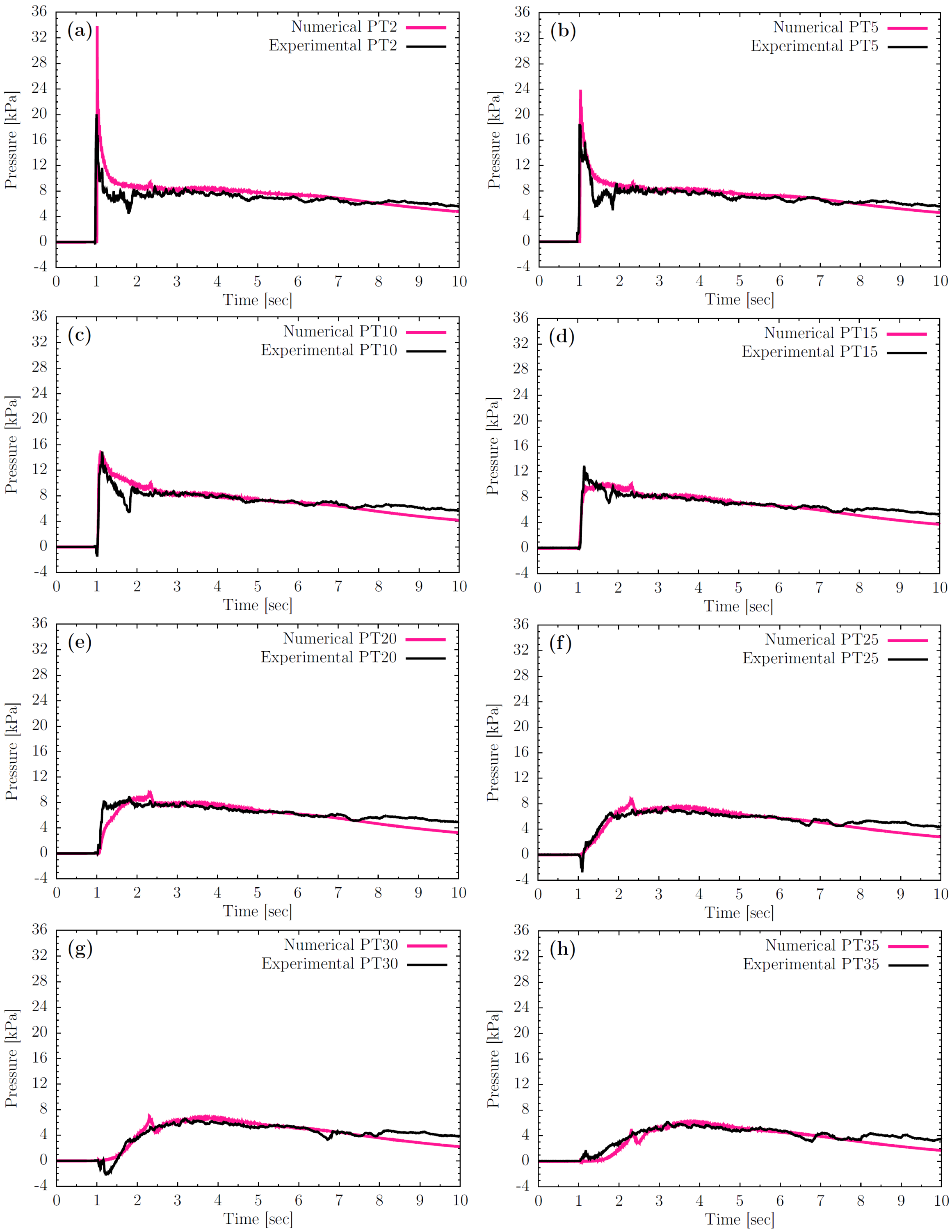

Figure 4.21: Comparison of numerical and experimental time-histories of pressure exerted on the upstream-facing side of the structure at elevations (a) 2cm, (b) 5cm, (c) 10 cm, (d) 15cm, (e) 20cm, (f) 25 cm, and (g) 30cm above the channel bottom for h_u = 1.15m.

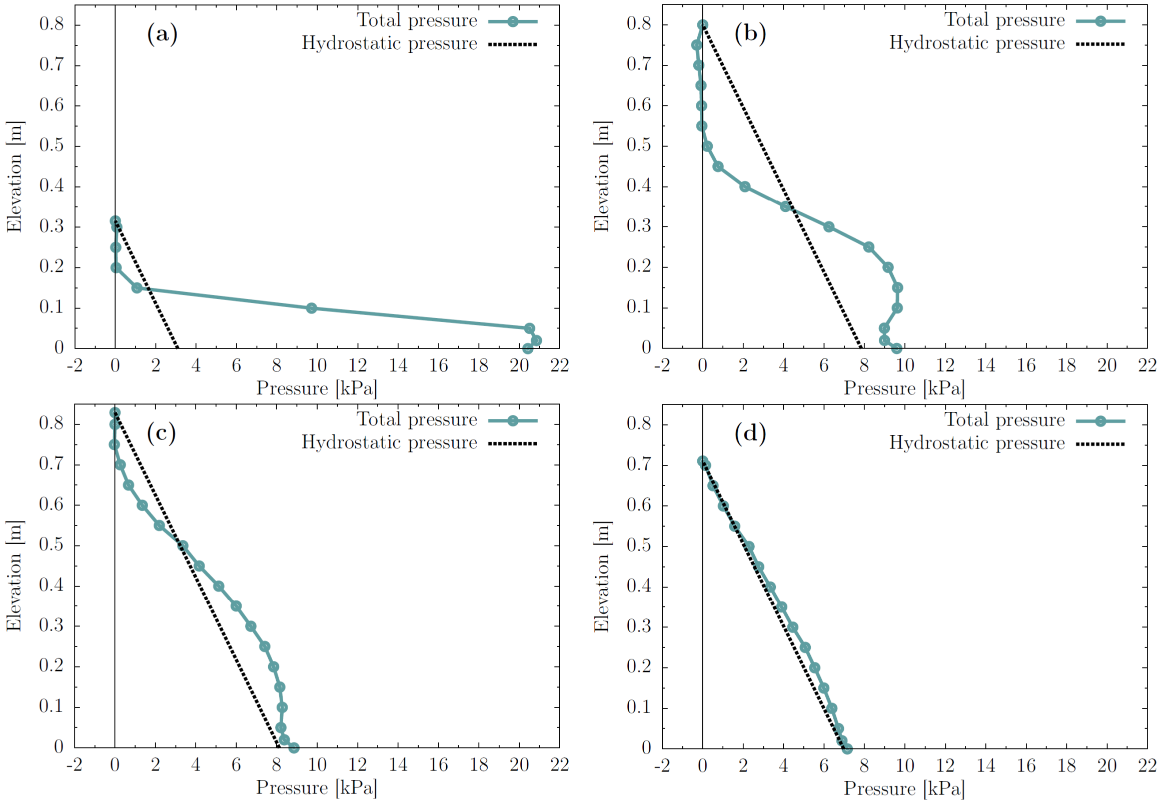

Figure 4.22: Vertical total and hydrostatic pressure distribution along the upstream-facing side of the structure at (a) 1.05 seconds, (b) 2.35 seconds, (c) 3.6 seconds, and (d) 7.0 seconds for h_u = 1.15m.

In each case (however less visible in Figure 4.22-d), it is observed that the total pressure profile intersects the hydrostatic profile at a certain elevation. Above the intersection, the total pressure is less than the hydrostatic pressure due to strong vertical accelerations present in the flow. Portions of the fluid which exhibit a pressure equal to zero are in free-fall (*i.e.*, not being supported by the fluid underneath it), whether it be the initial splash or regions near the top of the surface roller that forms shortly after the splash. At the intersection point, the increase in pressure due to the streamwise deceleration is balanced by the reduction in pressure due to the vertical and cross-stream accelerations (*i.e.*, dynamic pressure is equal to zero). Below the intersection point, the dynamic pressure is positive and results in a total pressure greater than hydrostatic. This pattern results in an S-shaped pressure profile, with the most extreme curvature occurring at early times. The curvature of the profile tends to decrease over time as the velocities die down, resulting in a nearly-hydrostatic pressure distribution by t = 7 seconds (Figure 4.22-d).

Figure 4.23 provides a more continuous view of how the vertical pressure distribution changes over time, from start to finish. The initial collision of the bore-front with the structure (just after t = 1 second) is characterized by extremely high pressures confined to relatively low elevations. These impulsive pressures rapidly diminish and the pressure profile evolves into the more gradually-varying S-shape seen in Figure 4.22-b.

Shortly after t = 2 seconds, it can be observed that a short-lived burst of pressure occurs along the structure at relatively high elevations (z = 0.3 to 0.9m). In fact, it is the only time throughout the duration of the simulation where any fluid pressure greater than atmospheric is exerted above z = 0.7m. As it turns out, the occurrence of this short-lived pressure is related to the collapse of the splash generated at intial impact onto the incoming flow. As the initial runup tongue curls back towards the upstream direction (the beginning of which can be seen in Figure 4.19-a) and begins to fall back down, a pocket of air becomes trapped in the process. Once the liquid first touches down onto the incoming flow, the pathway for the air to escape is cutoff, and the weight of the falling liquid attempts to compress the trapped pocket of air. In reality, the pocket of air would be allowed to compress, given long enough time scales, and would be accompanied with an increase in pressure. Since the numerical model treats the fluids as incompressible, however, the pocket of air is not permitted to undergo a change in volume. As a result, the increase in pressure, relative to what would occur during the experiments, occurs more rapidly and with a larger magnitude since the "cushion effect" offered by compressible air is not reproduced. In fact, evidence of this can be seen in the time-histories of numerical pressure provided earlier in Figure 4.21, where shortly after t = 2 seconds a small spike in pressure is observed.

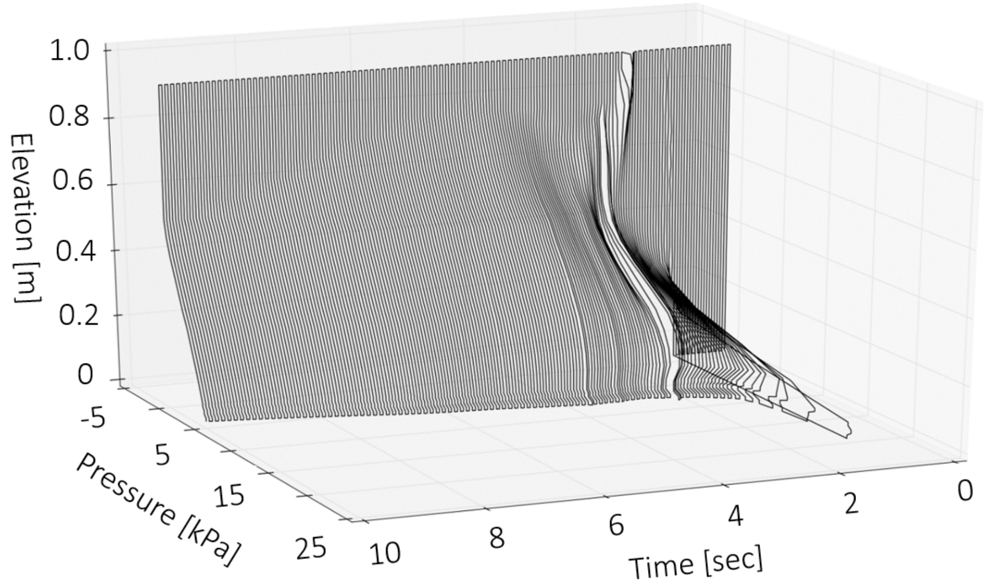

Figure 4.23: Time-history of simulated vertical pressure distribution along the upstream-facing side of the structure for h_u = 1.15m.

Although it is difficult to discern the same short-lived increase in pressure in the experimental time-histories of for h_u = 1.15m, it becomes increasingly clear for smaller initial impoundment depths. To illustrate, in Figure 4.24, it can be seen that both the numerical and experimental time-histories of pressure for h_u = 0.85m show the same spike occurring around t = 2 seconds. This demonstrates that the numerical model is in fact predicting a behaviour that occurs in reality, however, due to the incompressible treatment of the fluids, the physics are not in complete agreement (*i.e.*, the spike occurs with a greater magnitude and over a smaller time span relative to the experimental data).

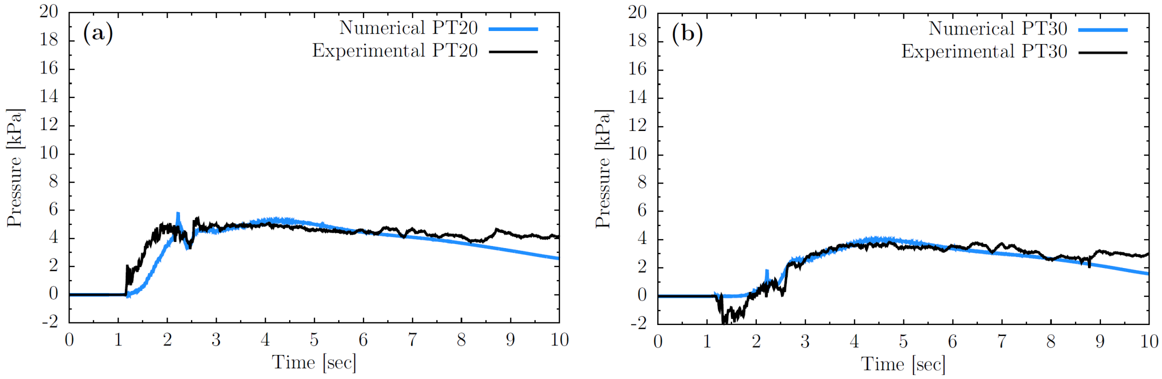

Figure 4.24: Comparison of numerical and experimental time-histories of pressure exerted on the upstream-facing side of the structure at elevations (a) 20cm and (b) 30cm above the channel bottom for h_u = 0.85m.

4.4.3 Force

Through integration of the numerical pressures over all four side of the structural model at each time step, time-histories of the net base shear force are generated. In the discussion that immediately follows, the specific terms that are used to describe several key moments during the bore-structure interaction are defined with the help of visual aids to increase the clarity of the concepts.

In Figure 4.25, a vertical red line is drawn across a typical force time-history produced during runs with h_u = 1.15m to indicate the time of interest. The times selected for display generally coincide with important events occurring in the force signal or water surface profile around the structure. In order to give context to the particular event being discussed, a plan and elevation view of the water surface profile along with a two-dimensional view ($x - z$ plane), cutting through the structure, of the pressure field is provided. The ripples or oscillations that can be seen on the surface of the water were noticed to be caused by the interfacial compression scheme applied to the transport equation for the phase fraction, described in Chapter 3. When the interfacial compression was turned off, the small oscillations on the surface disappeared from the solutions. However, in return, some non-physical behaviour of the interface was observed around the surface roller. In addition, the interface became more diffuse and some of the smaller details caused by real physical interactions began to get smeared out and disappear (such as the rooster tail forming in the wake). For these reasons, the purely unaesthetic ripples were considered a small price to pay to preserve the physicality and finer details of the flow.

Sometime between the initial impact of the bore-front with the structure and the leading edge of the wave advancing passed the leeside of the structure, the peak impulsive load is recorded in the force time-history. The impulsive load is distinguishable in the force signal as the small hump or plateau occurring immediately after the quick rise in force upon arrival of the leading edge of the wave. At this time, as shown in Figure 4.25-a, the water depths are relatively shallow due to the rapid spreading of the water column near bore-front. As a consequence of the latter and the resulting high velocities, the extreme impulsive pressures are confined to a small area at low elevations on the structure. It was shown in the previous section that the magnitudes of the impulsive pressures exceed those occurring at any other time during the interaction. However, since they are confined to such a small localized

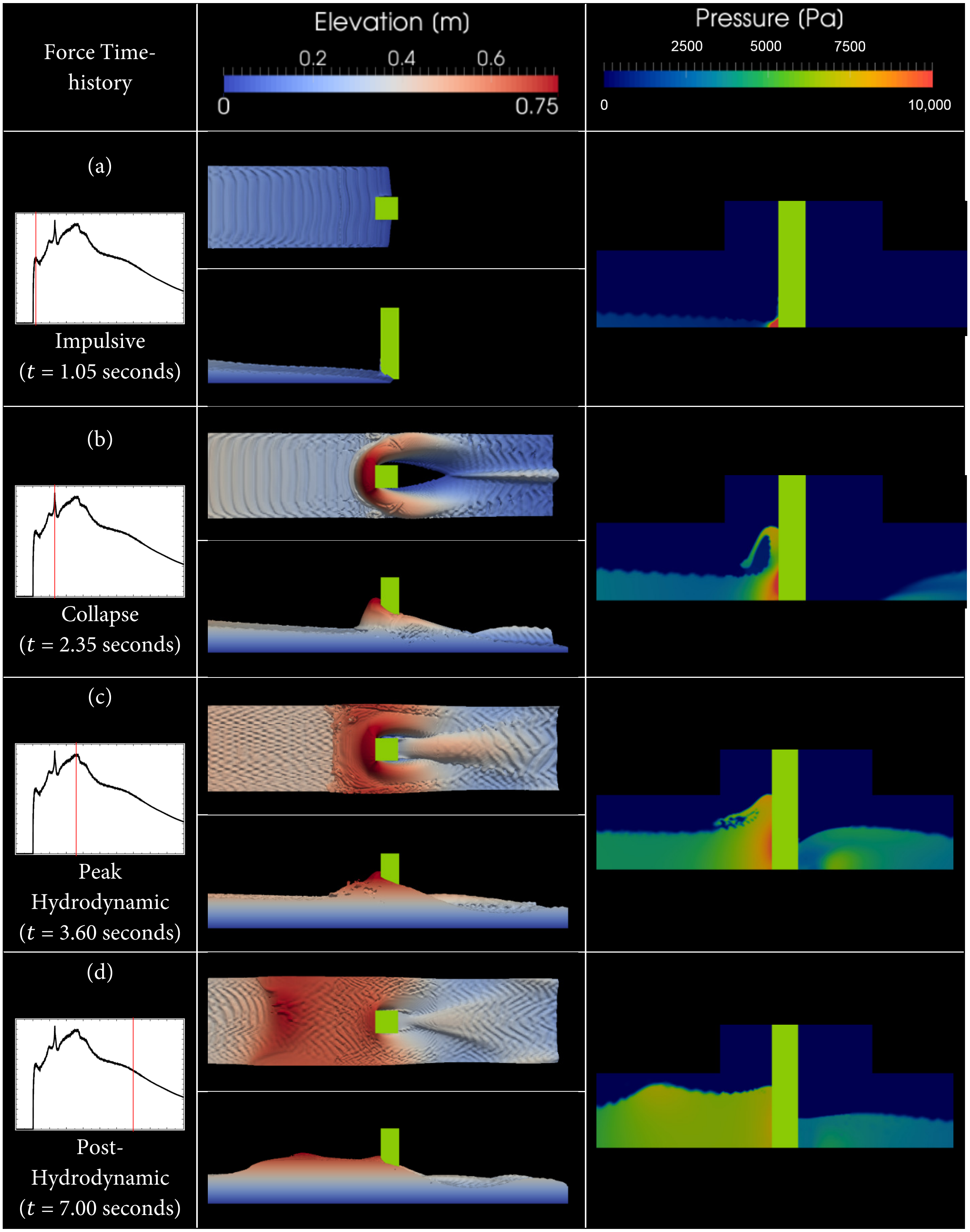

Figure 4.25 Visualizations of the water surface profiles (plan and elevation) and pressure field surrounding the structure during key moments of the bore-structure interaction: (a) Impulsive force, (b) collapse force, (c) peak hydrodynamic force, and (d) post-hydrodynamic force for h_u = 1.15m.

area, the resulting net force on the structure tends to be lower than what can be seen at later times. This realization was consistent for all three impoundment depths considered for both the numerical and experimental tests.

As revealed in Figure 4.25-b, the short-lived increase in pressure caused by the collapse of the runup tongue onto the incoming surge has a perceptible influence on the net force (herein referred to as the collapse force). The net force exerted on the structure at this time is a combination of the dynamic and hydrostatic pressures acting through the liquid phase, plus an additional shock component produced by the runup tongue crashing down onto the entrapped pocket of air (visibile in the pressure field displayed in Figure 4.25-b). As is clear from the plan view at this time, the water has not yet converged at the leeside face of the structure and so no hydrostatic pressure component counteracting the streamwise force is in effect.

Shortly after collapse of the initial runup tongue, the first symptoms of blockage effects in the flume can be noticed. As the incoming flow is diverted through the openings on either side of the structure, the component of the flow with a cross-stream direction runs up the flume walls and is reflected to rejoin the streamwise flow. The immediate implication is that the flow begins to compete to get through the openings, resulting in a gradual building up of water just upstream of the structure. In Figure 4.25-c evidence of this manifests as the apparent growing mound of water surrounding the column, first extending across the flume, and subsequently in the upstream direction. At the time of the peak hydrodynamic load (Figure 4.25-c) water levels at the front of the structure have nearly reached the second local maximum (the first being the initial splash). The important distinction is, however, that the majority of the water column at WG9 during the splash is in free-fall, and therefore does not meaningfully contribute to the net force. Since during the second local maximum the fluid accelerations are much less extereme, it has much more of a significant influence on the net force. Also clear at the timing of the peak hydrodynamic force is that the wake has fully closed. Although this is true, it can be seen that the fluid pressure adjacent to the leeside face of the structure (Figure 4.25-c) appears to be less than the fluid pressure at location with similar water depths along the profile. This reduction in pressure relative to hydrostatic next to the leeside face can most likely be attributed to the separation of the boundary layer as the flow passes the structure due to the abrupt, sharp edges. The resulting low pressure zone left in the wake of the column induces recirculation of the fluid, and two strong, stable vortices form which can be seen in the streamline plot provided in Figure 4.26. Intuitively, the increased water levels in the sheltered region behind the structure could be used to counteract the stronger pressures at the exposed face. However, the strong fluid accelerations in the wake appear to offer reductions in pressure relative to hydrostatic. Thus, for the purposes of design load calculations, it may not be accurate to assume a hydrostatic pressure distribution behind the structure if it is not sufficiently streamlined.

Immediately after the occurrence of the peak hydrodynamic load, the net force on the structure begins to decline at a relatively rapid rate. Just prior to the time represented in Figure 4.25-d, the incoming flow near the upstream edge of the growing mound of water becomes subcritical and the obstruction-induced wave is released. The remaining time is characterized by a linear decrease in

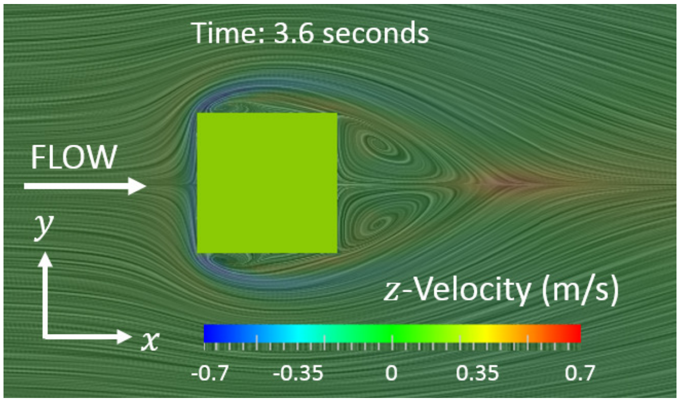

Figure 4.26: Streamlines of the flow at z = 0.05m around the structure at a time corresponding to the peak hydrodynamic load. h_u = 1.15m.

force as the flow velocities exiting the near-depleted reservoir diminish.

The numerical force time-histories produced using all three considered initial reservoir depths are compared to experimental data retrieved by the 6-DOF force gauge in Figure 4.27. In general, it is observed that the overall congruence between the numerical and experimental data tends to grow with increasing h_u. Nevertheless, reasonable levels of agreement are seen for all three initial upstream depths considered.

In the case of the forces exerted on the structure during runs with h_u = 0.55m (Figure 4.27-a), it is noticed that the impulsive load predicted by the numerical model is approximately half of the corresponding experimental value. However, for the two larger initial reservoir depths, the impulsive loads distinguishable in the numerical and experimental force signals appear to be in nearly perfect agreement.

As was discussed in the analysis of Figure 4.25, the collapse of the initial runup tongue causes a noticeable and short-lived increase in force. This collapse force can be seen in all three numerical force time-histories and tends to occur shortly after t = 2 seconds. With regard to this load component in the experimental data, it tends to be most prominent for smaller initial impoundment depths. For example, the experimental collapse force in the case of h_u = 0.55m (Figure 4.27-a) is easily recognized in the midst of the other noise appearing in the signal. The same can be said for h_u = 0.85m (Figure 4.27-b), however, it is clear that the deviation from the background trend caused by the collapse force is not quite as substantial. In the experimental force time-history for h_u = 1.15m given in Figure 4.27-c, it appears that the increase in force caused by the collapse of the runup tongue gets lost entirely and no longer appears as a distinguishable event. It is likely that that additional force caused by the collapse does not increase proportionally with the additional forces caused by increasing water depth and velocity as h_u is increased. Thus, although the collapse force is quite distinct in the case of h_u = 0.55m, the additional force caused by the collapse becomes essentially imperceptible for impoundments depths equal to or larger than h_u = 1.15m.

In fact, a similar observation was noted by Arnason (2005). In his thesis, it was documented that the force during impact for smaller bores was about 50% greater than the largest force occurring at a subsequent time. In fact, the force "during impact" being referred to was actually the force caused by the collapse of the runup tongue. For initial impoundments depths larger than $\sim h_u$ = 0.225m, Arnason (2005) found that the collapse force never exceeded the later-occuring hydrodynamic force. The trends in the experimental time-histories presented in Figure 4.27-a to Figure 4.27-c corroborate this finding. Although the numerical force signals do not tend to show the same trend, it is thought that the incompressible treatment of the air is responsible for the observed discrepancy. Since the collapse force is generated by the weight of the initial runup tongue crashing down onto the trapped pocket of air, the spike in pressure in the incompressible air occurs more rapidly and with a greater magnitude. When integrated over the surface of the structure, the result tends to be a sharper and overestimated numerical collapse force which is observed in Figure 4.27-b and Figure 4.27-c.

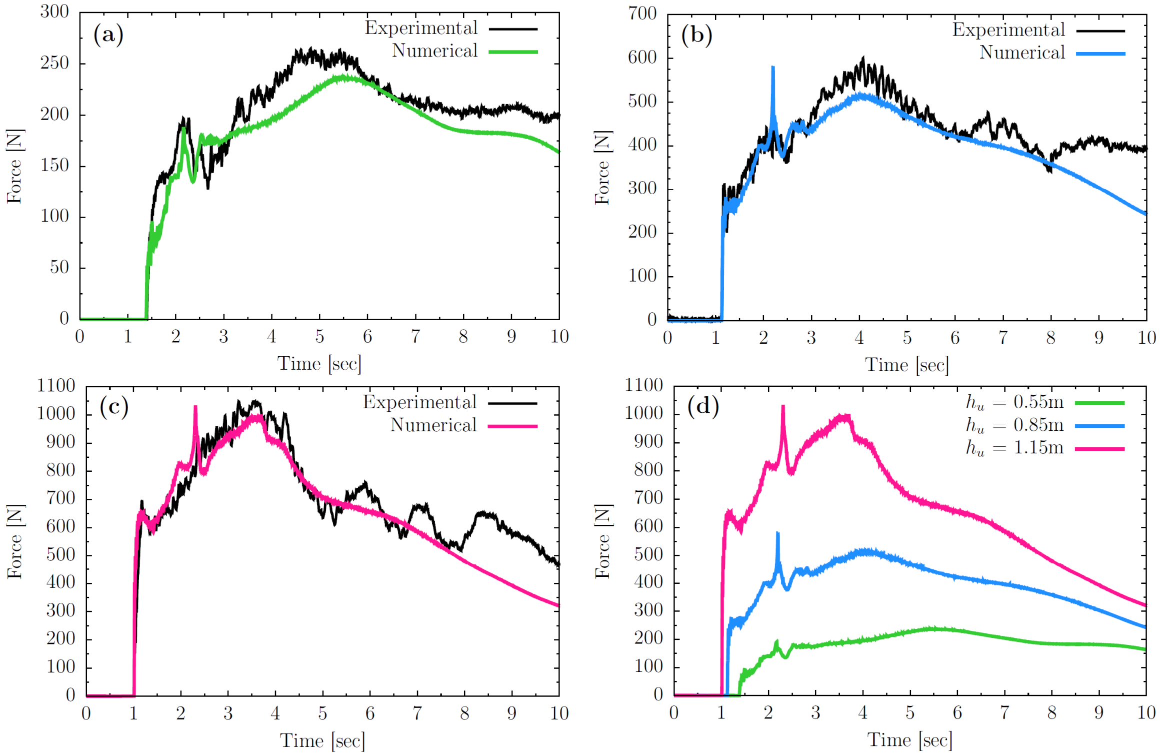

Figure 4.27: (a,b, and c) Comparison of numerical and experimental time-histories of net-base shear force acting on the structure for h_u = 0.55, 0.85, and 1.15m, respectively . (d) Comparison of all three numerical time-histories of force plotted on a common scale.

Finally, several oscillations with a period of ~1.5 seconds are observed near the end of the experimental force time-histories generated with runs using h_u = 0.85m and 1.15m. The occurrence of these oscillations are most likely associated with the shedding of unstable vortices forming in the wake of the column, as described earlier in the analysis of Figure 4.20-d. Although the formation of vortices in the wake was observed in the numerical results, they tended to remain stable, and therefore the oscillatory behaviour associated with the shedding was not emulated.

During the design stages of structures that may be vulnerable to bore-induced loading, typically, the designers will have access to flood maps that can provide estimates of maximum inundation depth at the site location. In some limited cases, an estimate for maximum flow velocity may also be available, however be it, with considerable more uncertainty. Thus, in a discussion about the time-history of bore-induced loading on a structure, it may be useful to examine how the depths and velocities vary at the site location without the structure present. With this in mind, Figure 4.28-a displays the temporal variation of water surface elevation at the structure location during unobstructed flow conditions for each of the three initial reservoir depths considered. At the beginning of each time-history, the initial rapid rate at which the water level rises reduces for a brief moment. The peak impulsive load generated at initial impact occurs just before this transition point. The timing of the impulsive load and corresponding surface elevation during unobstructed flow conditions is indicated by the square markers. Following the brief reduction in the rate at which the water levels rise, a stage of approximately linear increase is observed until the maximum inundation depth is reached. Upon arrival at this point, the surface elevation is seen to remain constant for some time before entering the final stage of decline.

The stars in Figure 4.28-a indicate the timing and corresponding surface elevation during unobstructed flow conditions of the peak hydrodynamic load, as defined in Figure 4.25-c. For all three initial reservoir depths, it is observed that the peak hydrodynamic load occurs just before maximum inundation depths are reached at the structure location. More precisely, this force is observed to occur when inundation depths at the structure location reach 96.0%, 89.6%, and 94.0% of the maximum inundation depth for initial reservoir depths h_u = 0.55, 0.85, and 1.15m, respectively. This result suggests that if the maximum inundation depth at the site location is used to calculate the peak hydrodynamic load, a safety factor may be automatically adopted into the result. The magnitude of the built-in safety factor will vary depending on how the force is correlated with inundation depth in the analytical formulation for estimating the design load.

Similarly, Figure 4.28-b displays the temporal variation in depth-averaged velocity at the structure location during unobstructed flow conditions. The same markers used to indicate the timing of the impulsive and peak hydrodynamic load are plotted to indicate the value of velocity at that time. In contrast to the water depth, maximum fluid velocity is observed upon arrival of the bore and consistently decreases thereafter. This is consistent with analytical predictions obtained using non-linear shallow water theory (Yeh, 2006) and experimental observations of bore runup on a beach (Shen and Meyer, 1963). At first, the reductions in velocity are drastic and appear to follow a parabolic trajectory towards zero. However, several seconds after the bore front has passed the velocity enters a stage of substantially milder decrease at a linear rate. The peak impulsive load generated at impact occurs when the velocity is near its maximum observed value. The occurrence of the peak hydrodynamic load, on the other hand, occurs at a time when the combination of the simultaneously-measured water depth and velocity produce the highest momentum flux. In the case of all three impoundment depths, this occurred at a time when the velocity at the structure location had decayed to 55.3%, 54.5%, and 53.2% of the maximum fluid velocity measured at the leading edge of the bore. This result was surprisingly consistent and indicates usage of the maximum computed velocity to estimate the peak hydrodynamic load would lead to substantially over-estimated design loads.

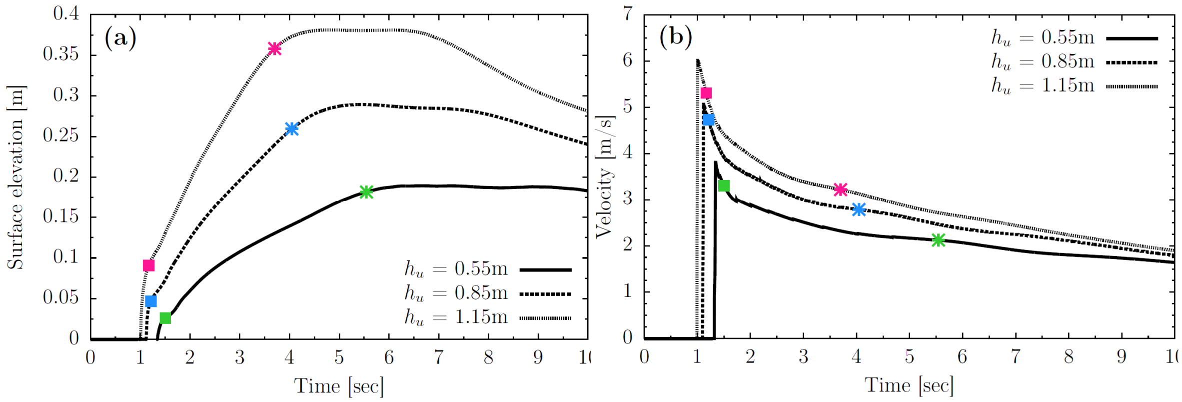

Figure 4.28: Water surface elevation (a) and depth-averaged velocity (b) at the structure location during unobstructed flow conditions (i.e., no structure present). The square and star markers indicate the timing at which the impulsive and peak hydrodynamic load occur.

4.5 Comparison of Numerical Results with Analytical Formulae of FEMA P646

In 2012, the U.S. Department of Homelands Security's Federal Emergency Management Agency (FEMA) released its second addition of FEMA P646, Guidelines for Design of Structures for Vertical Evacuation from Tsunamis. The project was primarily motivated by the acknowledgment of a lack of suitable guidance to design structures capable of withstanding the extreme forces of a tsunami. Given the proximity of the Western Seaboard of North America to the Cascadia Subduction Zone, the feasibility of horizontal evacuation before arrival of a tsunami, triggered by a fault slip, is significantly reduced. Thus, FEMA P646 was one of the first efforts to provide a new means to mitigate the effects of tsunamis to communities bordering the Pacific.

The report decomposes the effects of a tsunami into several load components and attempts to quantify each according to estimates of local flow conditions (inundation depth and flow velocity). Typically, these values would be obtained from tsunami inundation maps based on a given design return period or numerical models developed for certain stretches of the coast. In the latter case, more detailed estimates for the velocity fields may be obtained, given a fine enough mesh resolution. It is important to bear in mind that, in general, the estimates for local flow conditions during tsunami inundation are generated by the wave interaction with topography alone. Thus, modifications to local flow conditions caused by the presence of existing structures is neglected in current design standards.

Of particular relevance to the scope of the current work are the analytical formulations for estimating the forces acting in the direction of tsunami wave propagation. Namely, the impulsive and maximum hydrodynamic load. Although FEMA P646 also provides formulations for estimating debris impact loading, which also acts in the main flow direction, it is not considered in the present work.

FEMA P646 proposes to use the maximum momentum flux $(hu^2)_{max}$ at the site location to estimate the maximum hydrodynamic (drag) forces exerted on the structure in a formulation given as

$$F_d = \frac{1}{2}\rho_f B C_D (hu^2)_{max}\,, \tag{5.6}$$

where ρ_f is the density of the fluid including entrained sediment , B is the streamwise-projected width of the structure, C_D is the drag force coefficient with a recommended value of C_D = 2.0 for square structures, h is the inundation depth and u is the flow velocity. Since the timing of maximum inundation depth and maximum fluid velocity do not necessarily coincide, the h and u^2 terms are multiplied together and the maximum value of the product is used. As suggested by the results shown in the previous section, the maximum momentum flux typically occurs when water depth and flow velocity are 90-95% and 50-55% of their maximum values achieved during passage of the wave, respectively. If a detailed numerical model of tsunami inundation in the vicinity of the proposed structure is not feasible, the maximum momentum flux can be evaluated according to an exact solution to nonlinear shallow water theory given by Yeh (2007).

In order to calculate the momentum flux for use in equation (5.6), numerical predictions of water depth and depth-averaged velocity at the structure location during unobstructed flow conditions were used. Rather than using the maximum value of momentum flux to calculate the governing hydrodynamic load, the entire time-histories shown in Figure 4.28 are used to generate time-histories of FEMA P646-predicted values of hydrodynamic loading instead. In order to obtain these, a fluid density of ρ = 1000 kg/m^3 along with the recommended value of C_D = 2.0 and a structure width of B = 0.30m. The comparison provided in Figure 4.29 shows that the FEMA P646-predicted forces follow remarkably similar trends as the corresponding numerical ones. In the case of initial impoundment depth h_u = 0.55m, the forces are reproduced with a high degree of accuracy at all stages of the interaction. However, it can be seen that a growing discrepancy emerges between the peak hydrodynamic loads for increasing initial reservoir depth. This result suggest that the recommended value of C_D = 2.0 may provide reasonable estimates at small scales. However, for prototype and larger model scales it may produce overly conservative design loads.

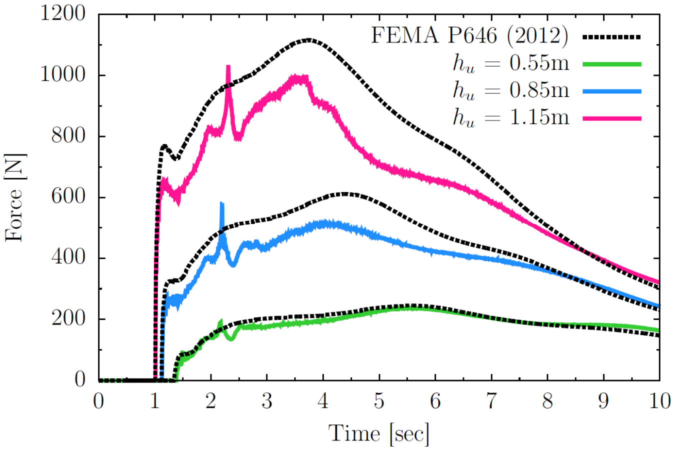

Figure 4.29: Comparison of numerical time-histories of force exerted on the structure to analytical predictions of the hydrodynamic force by FEMA P646 (2012) for all three initial impoundment depths.

To investigate further, the simulated time-histories of net force exerted on the structure were used to reverse calculate the drag coefficients using equation (5.6). The drag force coefficients corresponding to the peak hydrodynamic load for the three initial impoundment depths h_u = 0.55, 0.85, and 1.15m are C_D = 1.92, 1.71, and 1.79, respectively. In Figure 4.30, the extracted drag force coefficients are plotted against initial impoundment depth and are compared to results obtained by Arnason (2005). The data from Arnason (2005) alone show a clear inverse relationship between drag coefficients and initial impoundment depth. The data points from the two smaller initial impoundment depths considered in the current work (h_u = 0.55 and 0.85m) show a propensity to follow the same line of regression generated using Arnason's (2005) data. However, considered alone, the drag coefficients extracted from the results of the present study, on average, show a tendency to decrease at a slower rate with increasing initial impoundment depth. Based on this observation, it is reasonable to expect milder decreases in drag coefficient with further increases in initial impoundment depth until, eventually, it becomes completely independent of the latter.

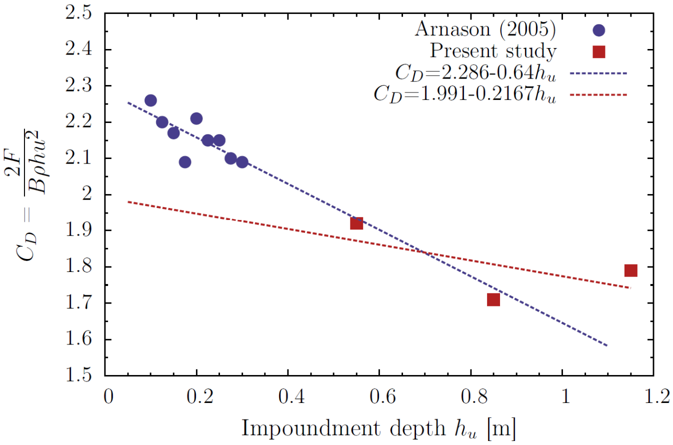

Figure 4.30: Variation of drag force coefficient corresponding to peak hydrodynamic load with initial impoundment depth.

Estimates for the maximum impulsive load are conservatively quantified by FEMA P646 as a linear relationship with the maximum hydrodynamic load, expressed as

$$F_i = 1.5F_d \, . \tag{5.7}$$

The relationship expressed in equation (5.7) was allegedly derived from experimental data obtained by Ramsden (1993) and Arnason (2005). In his dissertation, Ramsden (1993) had observed that the initial force of a bore propagating over an initially dry bed never overshot the latter quasi-steady loads. However in the case of bores propagating over initially inundated surfaces (a relatively thin layer in comparison to the initial impoundment depth), the maximum force occurring near the beginning of the force time-history tended surpass the latter peak hydrodynamic load by approximately 50%. This observation by Ramsden (1993), in part, was used to justify the relationship applied by FEMA P646 to estimate the impulsive load. However, deeper into the dissertation, Ramsden attributed the initial peak that overshot the later peak hydrodynamic load to the runup tongue collapsing onto the incoming surge – not the impulsive force caused by the impact of the leading edge of the wave. In fact, the impulsive load was never observed, in any case, to overshoot the later peak hydrodynamic load. The reason why the collapse force was observed to exhibit a higher magnitude than the later quasi-steady load is almost certainly linked to the small model scales employed (initial impoundment depth h_u = 0.502m). As mentioned earlier, it was observed in the present work that the collapse force tends to become less important as model scale (or initial impoundment depth) increases, becoming essentially imperceptible for impoundment depths equal to or larger than h_u = 1.15m.

Similarly, Arnason (2005) had observed that, for the smaller bores (those generated using $h_u <$ ~0.225m), the force during impact was generally larger than or equal to the peak hydrodynamic force occurring shortly thereafter. It should be noted that, the observed peak "during impact" was in fact the force caused by the collapsing runup tongue, a fact that was not mentioned in the discussion. In the worst case scenario (also the smallest bore tested and therefore not by coincidence), the collapse force surpassed the later peak hydrodynamic force by 50%. Since, at the time, there was still considerable uncertainty regarding the impulsive force, FEMA P646 conservatively took these observations and proposed the relationship expressed in equation (5.7). In light of the analysis presented in the current work, and after a deeper look into the results of Ramsden (1993) and Arnason (2005), there appears to be no evidence that the net impulsive force on the structure (or the collapse force for that matter) will ever exceed the net peak hydrodynamic force during interaction between a full-scale bore and structure. However, this does not rule out the possibility of the impulsive load exceeding the hydrodynamic load on individual elements of the structure. Since elements at low elevations (equal to or smaller than the depth of the bore-front) will transfer the entirety of the impulsive load to the structure, but only a portion of the later-occurring peak hydrodynamic load (if the element becomes completely submerged), the local shear on the element generated at initial impact may exceed those occurring at later stages of the inundation.

4.6 Results of Numerical Experiments

4.6.1 Effect of Bed Condition

Tsunamis occur as a series of waves which break near the shoreline prior to advancing inland as a turbulent bore. The first inundating wave will typically encounter dry land, commonly referred to as a "dry bed condition". Depending on a variety of factors such as wave amplitude, wave period and local topography, subsequent waves may arrive before the last has had time to fully recede, encountering what is referred to as a "wet bed condition". For this reason, it is of interest to understand the effect that the bed condition has on bore propagation and how that may influence the loading on a structure. This aspect was investigated numerically by St-Germain (2012) using a single phase weakly compressible SPH model. However, St-Germain (2012) describes substantial difficulty in modeling target downstream depths due to the repulsive boundary force acting on the fluid particles. Consequently, only the smallest possible downstream depth of h_d = 0.08m was considered. In the present study, any desirable downstream depth could be produced by modifying the height of the bottom layers of grid cells and setting an appropriate initial phase fraction distribution. In the following sections, the effects of varying initial downstream depths (h_d = 0mm, 5mm, 20mm, and 50mm) on propagation characteristics, runup on the structure, and the resulting forces using an initial impoundment depth of h_u = 1.15m are presented.

4.6.1.1 Propagation Characteristics

Time-histories of depth-averaged velocity taken 0.57m upstream of the structure face for various initial downstream depths are displayed in Figure 4.31. After passage of the leading edge of the bore, there appears to be steady declines in velocity over time for the case of all initial downstream depths considered. Additionally, there appears to be drastic reductions in the flow velocity near the bore front as the initial downstream depth is increased. However, in comparing the arrival time of the bores (the point at which the velocity begins to rise in the time-history), a contradictory idea appears to be suggested. If the arrival times of the bores are so similar, why, then, the substantial discrepancy in velocity observed in the first few seconds following arrival of the bore? As is turns out, the presence of the initially quiescent layer of water residing on the channel bed has a large influence on depth-averaged measurements taken near the bore front.

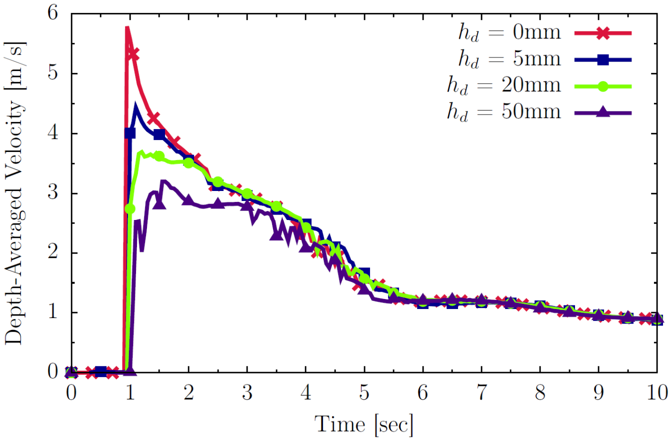

Figure 4.31: Time-history of simulated depth-averaged velocity at a location 0.57m upstream of the structure for varying initial downstream depths. h_u = 1.15m.

To illustrate, successive still-frames of the velocity field in the $x - z$ plane are provided in Figure 4.32 which show how the dam-break bore propagating over an initially still 50mm layer of water develops over time. Shortly after removal of the gate (Figure 4.32-a), a jet of water forming as a result of the induced pressure discontinuity appears to be directed at a slight upward angle. This behaviour is similar to the experimental observations made by Stansby et al. (1998) and appears to be caused by the resistance imposed by the initially still layer of water. Since the jet of water will tend to follow the path of least resistance, the downstream layer of water acts to work as an inclined ramp for the initial jet of water. After observing the bore profiles given in Figure 4.32-b and Figure 4.32-c, it becomes clear that a portion of the bore front rides on top of the initially still downstream water with seemingly little interaction. At some point upstream of the bore front, a sufficient amount of time has passed for the released upstream water to fully transfer its momentum to the underlying layer. The location at which the jet of water is elevated by the “inclined ramp”, then, tends to move further downstream as time passes. Due to the upward velocity component at this point, an undulation on the surface behind the bore front appears and is clearly visible in Figure 4.32-c. In fact, the undulation on the surface marks the beginning of the section of bore front that appears to ride on top of the initially still downstream water. Upstream of the surface undulation, the vertical velocity distribution appears to be much more uniform than on the downstream side. It is this discontinuity in the vertical velocity distribution in the bore front region that explains why such drastic reductions in depth-averaged velocities appear in Figure 4.31 for increasing initial downstream depths. It can be seen in Figure 4.32-c that, in the case of the 50mm wet bed, the velocity of the bore tipis approximately 5.5 m/s. Comparing this to the corresponding measured value for the case of a dry bed (roughly 5.8 m/s from Figure 4.31), the magnitude is smaller, but not by nearly the same margin suggested by Figure 4.31 alone. Although Figure 4.31 suggests a significant increase in in resistance to the advancement of the bores for increasing downstream depth, the bore travelling over a 50mm wet bed arrived at the structure only 0.12 seconds later than the dry bed surge.

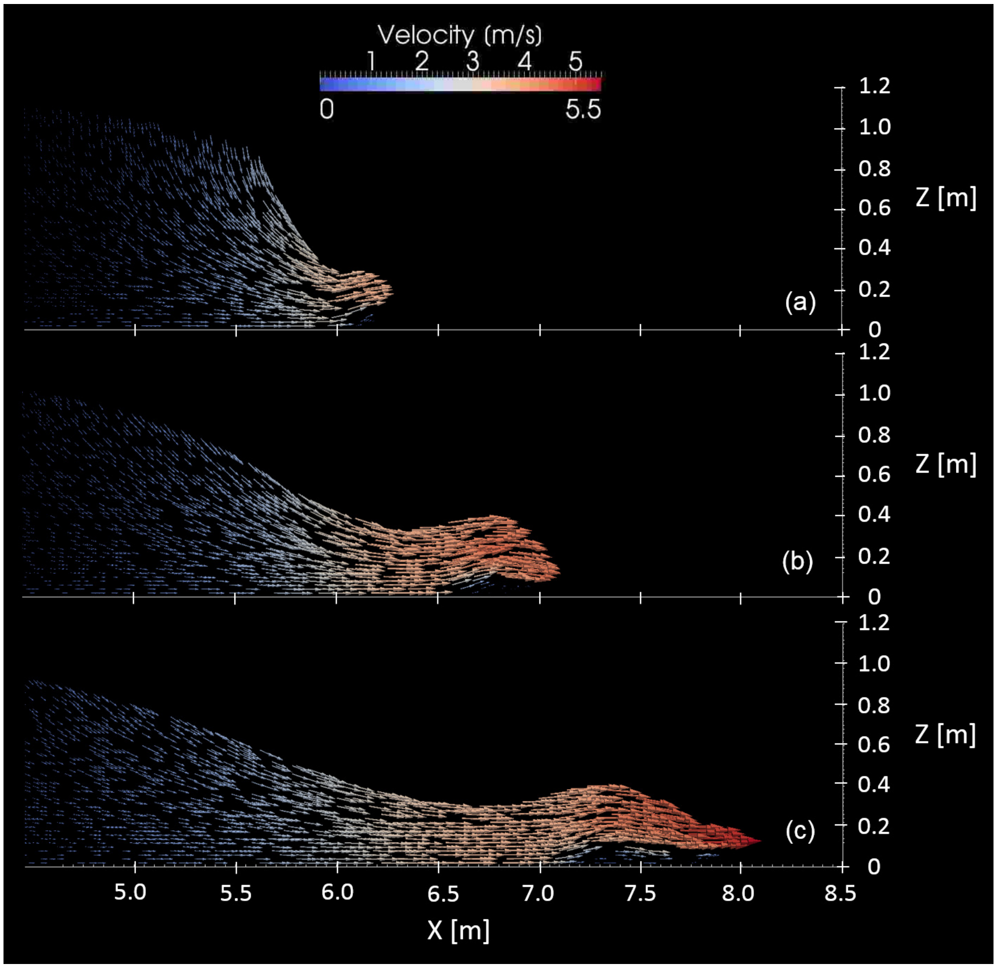

Figure 4.32: Development of the dam-break bore propagating over an initially inundated surface (h_d = 0.05m, h_u = 1.15m): (a) Time: 0.25 seconds, (b) Time: 0.45 seconds and (c) Time: 0.65 seconds.

Comparisons of the numerical bore profiles immediately before impact are provided in Figure 4.33 for all initial downstream depths considered. Since it was shown that the underlying water beneath the bore front region is essentially motionless (and therefore does not contribute to the impulsive loading), a comparison of the bore front shapes are also provided with a reference elevation at the initial downstream water surface elevation (Figure 4.33-b). In this way, a better comparison of the portion of the profile that actually a dynamic pressure on the structure can be performed. From

Figure 4.33-b it can be seen that, in general, the wet bed condition contributes to the accumulation of a greater volume of water near the leading edge of the bore (*i.e.*, the bore front becomes deeper). This effect is noticed even with the thinnest layer of water covering the channel bed (h_d = 5mm). As a result, the near-vertical face of the bore front which impacts the column is extended vertically. However, considering only the wet bed bore profiles, very minimal changes in shape are noted at the leading edge. The most pronounced difference is the amplitude of the surface undulation that occurs upstream of the bore front. Since, however, the bore profiles in the tip region appear to be quite similar, the influence of non-zero values for downstream depth (at least the ones considered here) on impact dynamics is expected to be minimal.

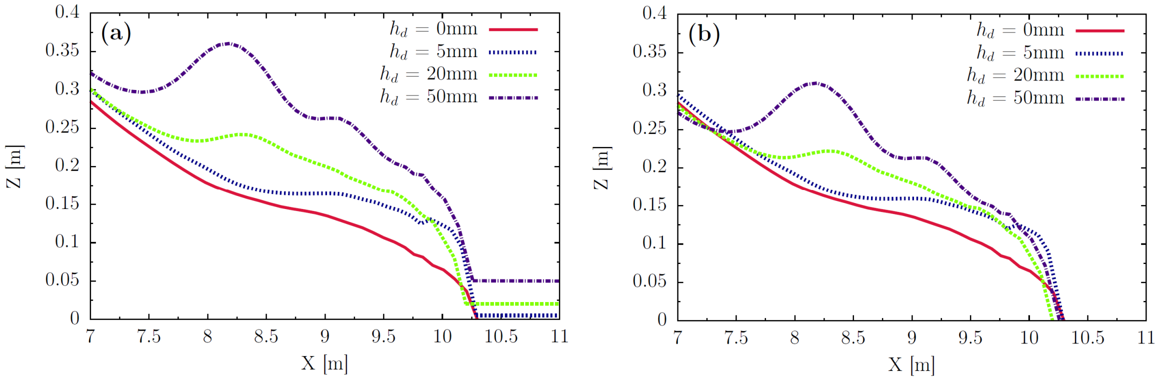

Figure 4.33: Comparison of simulated bore profiles for varying initial downstream depths (h_d) with the reference elevation at the (a) channel bed and (b) initial downstream water surface elevation. h_u = 1.15m.

4.6.1.2 Structure Runup

A comparison of simulated runup on the upstream facing side of the structure for all initial downstream depths considered is given in Figure 4.34. The time-histories demonstrate that the bed condition exerts the greatest influence on the runup at times during the splash following initial impact. The splash reaches the highest elevation for bores propagating over initially dry channel beds. In general, consistent decreases in splash height are observed as initial downstream depth is increased. Comparing the two most extreme cases, the dry bed and 50mm wet bed, a reduction of over 25% in peak splash height is observed. This trend appears to be in opposition with that described in the work conducted by Ramsden (1993). During his experiments, Ramsden observed that the peak splash height for a bore propagating over wet beds exceeded that of those travelling over initially dry channel beds. This result was attributed by Ramsden to the fact that the bores propagating over the wet bed tended to accumulate a larger volume of water in the bore tip region, an observation that was also confirmed in the present study. However, several important physical distinctions can be made that may, each, be partially responsible for the apparent conflicting observations. Firstly, Ramsden's (1993) comparison of a surge (dry bed) and bore (wet bed) was performed such that the initial impoundment depth was adjusted, rather than being held constant, so that the bore front celerities were approximately equal. Although the difference in initial impoundment depth was relatively modest (h_u = 0.50 and 0.48m for the surge and bore, respectively), the fact that the celerity was not permitted to vary likely had a measurable influence on the results. Lastly, it is worth noting that Ramsden's experiments considered the impact of bores on a vertical wall extending entirely across the width of the flume, effectively reducing it to a two-dimensional problem. This may be an important distinction considering the additional degree of freedom in the three-dimensional flow around the structure in the case considered here. Interestingly, after the initial splash collapses there appears to be no distinguishable differences in the runup onto the structure for all four bed conditions considered.

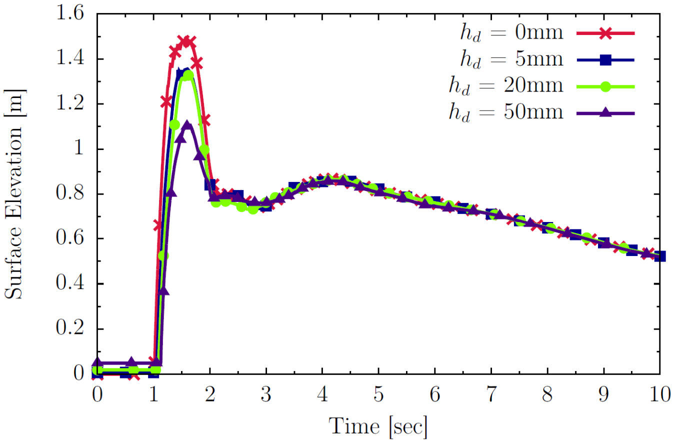

Figure 4.34: Time-history of simulated runup on structure face for varying initial downstream depths. h_u = 1.15m.

Intuitively, it seems reasonable to assume that the maximum splash height would be directly related to the celerity of the incoming bore. Given that the bore propagating over the dry and 50mm wet bed arrived at the structure after t = 1.0 and 1.12 seconds, respectively, and that the distance between the reservoir and the structure is 4.77m, the difference in average bore front celerity between the two cases was 0.51m/s. However, it does not seem likely that the relatively marginal difference in bore front celerity would be solely responsible for the substantial decrease in splash height observed. According to Ramsden (1993), the volume of the bore tip is also a factor in determining the height of the splash. However, his observed positive correlation between volume and splash height was already shown to be in contradiction with observations made in the present work. Thus, the question of why such a large decrease in splash height between the two cases still remains. The only other reasonable question to ask would be, where does the water go during impact? In Figure 4.35, a vector field cutting through the $x - z$ plane in front of the structure is given for the two most extreme bed conditions just before the splash reaches peak elevation. As was shown earlier, at the time of impact, the first meter or more of the bore front rides on top of the initially quiescent downstream water layer. In Figure 4.35-b, a clear division between these layers is made visible by the sharp discontinuity between the vertical velocity distribution. Since the rapidly advancing 50mm wet bed bore travels on top of the underlying still water layer, the dynamic pressure is exerts on the structure during impact is centered at a higher elevation relative to the dry bed case. In fact, due to the presence of the underlying still water layer, the dynamic pressure gradient is roughly equal in both the upwards and downwards direction. In the case of the wet bed bore, a pressure gradient sets up a point of flow divergence along the structure face located at an elevation of approximately 0.2m at the time shown in Figure 4.35-b. As a result, it appears that only the top half of the impacting bore gets diverted upwards, creating the splash. The lower half appears to be diverted downwards, becoming part of the horseshoe vortex that begins at the toe of the structure, extending laterally and eventually wrapping around the sides of the structure. In contrast, the downward pressure gradient in the case of the dry bed bore is roughly equal to zero due to the proximity of the pressure center to the channel bottom. As such, the generated pressure gradient drives the entire section of the bore upwards, creating a splash of larger magnitude.

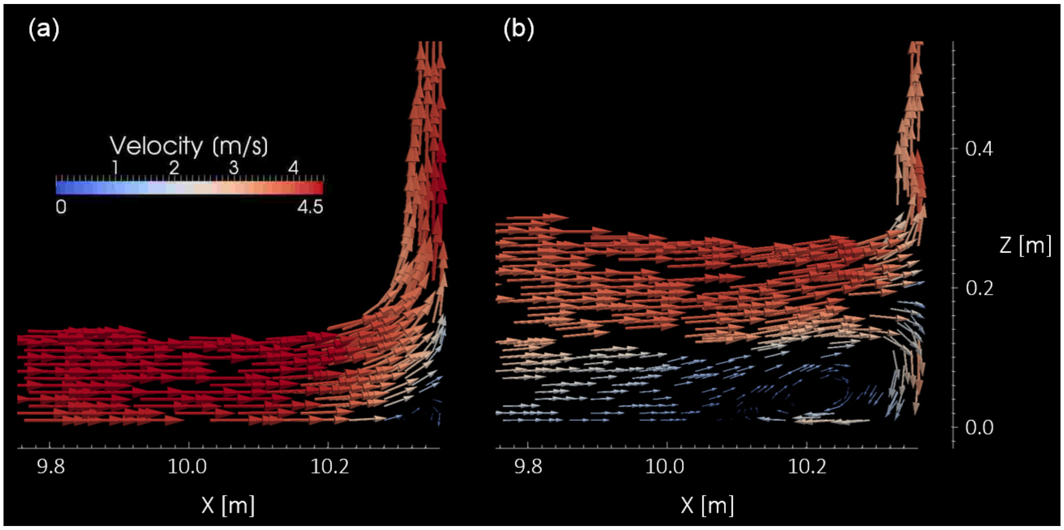

Figure 4.35: Elevation view of the velocity field at the upstream facing side of the structure just before initial splash reaches peak elevation (Time: 1.30 seconds) for an (a) initially dry channel bed and (b) initial downstream depth of h_d = 0.05m. h_u = 1.15m.

4.6.1.3 Force

Time-histories of the resultant streamwise force acting on the structure for all four bed conditions considered are given in Figure 4.36. It can be seen that after approximately t = 4.5 seconds the bed condition ceases to have any influence on the results. Prior to this instance, however, there are some relative deviations in behaviour worth mentioning. Firstly, the initial downstream depth appears to have an influence on the impulsive loads generated at impact. In the case of the bore propagating over a 5mm and 20mm layer of downstream water, the initial impulsive load appears to exceed that generated by the dry bed surge. This overshoot in the magnitude of the dry bed impulsive load is, however, relatively marginal, exceeding it by only ~11.5% in the worst case scenario (5mm wet bed). In contrast, further increases in downstream depth beyond h_d = 20mm appear to have a damping effect at this stage of the loading process, as can be seen in the time-history for the 50mm wet bed condition. In this case, the damping effect seems to be more pronounced than the amplification effect observed for two smaller initial downstream depths. As was previously shown in Figure 4.33 even the thinnest layer of water can have a significant effect on the bore profile, increasing the depth of the near-vertical face of the bore front. Further increases in downstream depth beyond h_d = 5mm, however, did not seem to induce any significant changes near the bore face. Since there are no real distinctions to be made between the steepness or depth of the bore front for the wet bed bores, the differences observed in the impulsive loads exerted on the structure must be related to some combination of bore front celerity and air entrainment. Perhaps, in the case of the two smaller downstream depths (h_d = 5 and 20mm), the slight amplification of the impulsive load caused by the increase in bore depth had overridden any dampening effects caused by increased air entrainment or reductions in bore front celerity. On the other hand, in the case of the deepest downstream depth considered (h_d = 50mm), the reductions in bore front celerity and fluid density (as a result of additional air entrainment) may have become more dominant effects than the increase in bore front depth, resulting in a dampening of the impulsive load.

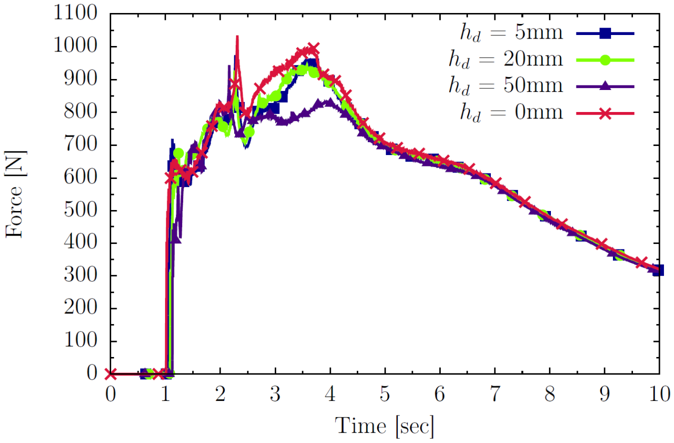

Figure 4.36: Time-history of simulated streamwise force exerted on the structure for varying initial downstream depths. h_u = 1.15m.

However, the largest and perhaps most important difference seen in the time-histories of force shown in Figure 4.36 occurs during the peak hydrodynamic load (which is also the governing load in the experimental results) around t = 3.5 seconds. Although there appears to be very marginal decreases in the peak hydrodynamic load for the two smaller downstream depths (h_d = 5 and 20mm) relative to the dry bed case, there appears to be a much more significant reduction in the case of h_d = 50mm. As was shown in the previous two sections, the runup on the structure and depth-averaged velocity for the four bed conditions considered have converged to the same value by t = 3.5 seconds, ruling these two factors out as the primary cause. Another important factor that influences the net force is the differential pressure between the upstream and downstream face of the structure, which, in this case, is entirely controlled by water levels in the wake (runup on the front of structure has been shown to be equal at t = 3.5 seconds for all bed conditions). Due to a few instances of rapidly varying surface elevation in the wake (that may lead to nonhydrostatic pressure), it was decided to plot total pressure over time at the base of the leeside face for the four bed conditions in Figure 4.37. It can be seen that the pressure acting on the leeside face of the structure begin to rise earlier for increasing initial downstream depths, indicating a more rapid wake closure. In the fact, the difference in the pressure acting on the leeside face for the different bed conditions can be quite substantial, particularly before t = 4.5 seconds. For example, at t = 3.5 seconds, the pressure on the leeside face of the structure has risen to 3.5kPa in the case of the 50mm wet bed condition, whereas in the dry bed case the pressure has only just reached 0.5kPa. Between t = 3 and 4 seconds, where the most substantial difference in net force appears in Figure 4.36, there are quite significant differences between the hydrostatic pressures acting on the leeside face which help explain the reduction in net force. The reason why the wake tends to close faster for increasing downstream depth is thought to be related to the corresponding increase in bore depth (as seen in Figure 4.33-b) and additional resistance imposed on the advancement of the bore. In the case of the former, after the flow is split into two streams by the structure, the rate at which they converge behind the structure is directly related to the lateral pressure gradient induced by the differential water level between the centerline of the flume and the sidewalls. In the case of the latter, the additional resistance imposed by increasing the downstream depth slows the velocity of the bore. When this is the case, the two streams tend to converge at a location closer to structure, therefore reaching it earlier than in cases with lower downstream depths.

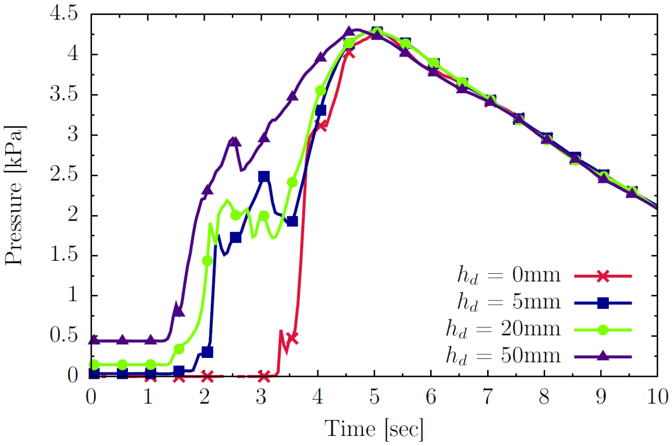

Figure 4.37: Pressure exerted at the base of the lee-side face of the structure for varying initial downstream depths. h_u = 1.15m.

5 Pneumatic Long Wave Generation

5.1 Description of the Physical Experiments (Stolle et al., 2015)

The experimental modeling portion of the project was conducted in the new Tsunami Wave Basin (TWB) at the Coastal Engineering and Management Laboratory of Waseda University, Tokyo, Japan. The physical configuration of the new long wave generating facility was first used by Stolle et al. (2015) to investigate the motion of debris fields carried by tsunami-induced bores propagating through harbour environments. The work includes analysis on the hydrodynamics generated by the pneumatic wave generator which is prerequisite to understanding the initiation of motion and dynamics of the debris field.

In the two sections that follow, details are provided on the physical dimensions of the wave basin and instrumentation that are subsequently used to develop the numerical model and to analyze the results.

5.1.1 The Tsunami Wave Basin

A major historical issue encountered in the physical modeling of tsunami waves has been the accurate reproduction of the extremely long wave lengths relative to wind waves. Most piston-type wave generators lack the required stroke length required to generate realistic wave lengths of a tsunami which may vary from 1-100km at prototype scale. To overcome this challenge, a principle originally applied to create tides in large scale wave basins (pneumatic tide generation) has been adopted in the design of the TWB.

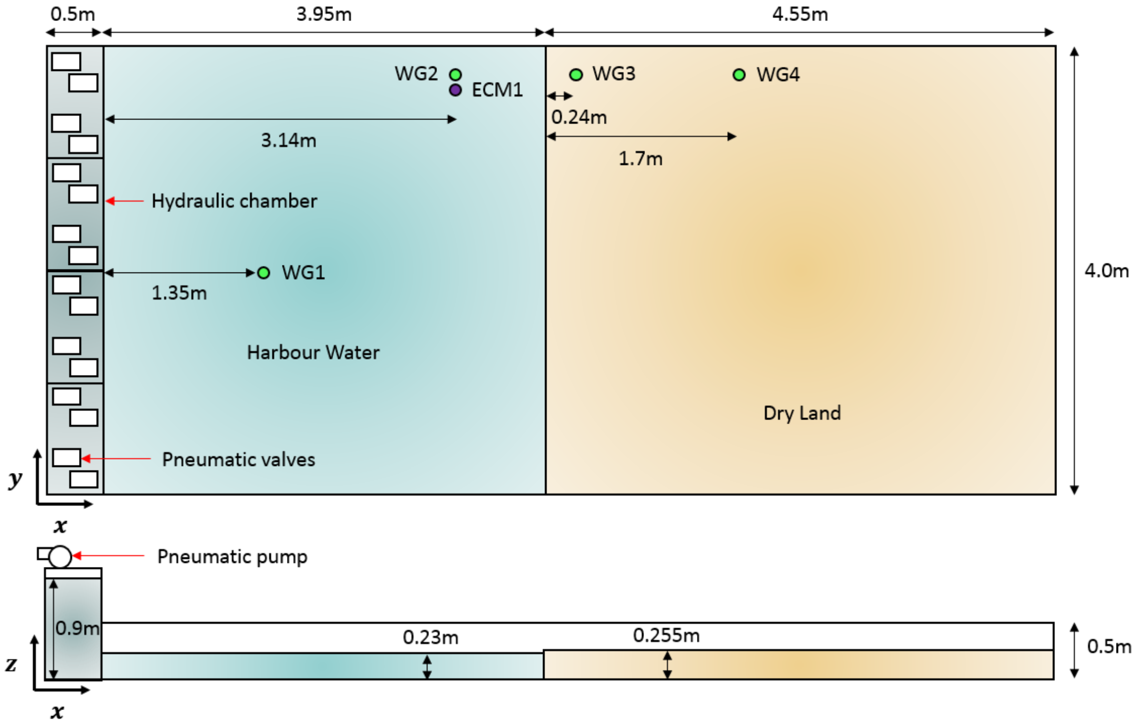

Figure 5.1: General configuration of the Tsunami Wave Basin

The outer horizontal dimensions of the TWB measure 9.0m-long x 4m-wide for which the area is divided into three major sections. A drawing illustrating the general configuration of the wave basin is provided in Figure 5.1. The area adjacent to the downstream end is constructed as a rigid horizontal false floor elevated off the bottom of the basin by 0.255m. The topography of the dry land drops vertically at the seaward edge similar to a quay wall to simulate the conditions of a modern port environment. The hydraulic chamber at the opposite end houses four separate reservoirs fillable by pneumatic pumps (TST-150, Sato Vac Inc., Japan) that remove the air inside the sealed compartments. The impounded volume of water is released through a 0.1m-high outlet running adjacent to the basin floor by the opening of computer-controlled valves (SVB1V-50F-02HS, CKD Corporation, Japan) mounted along the top of the hydraulic chamber. The middle section representing the harbour serves as a stretch of water to propagate the released long waves to the shoreline where it typically breaks and surges across the dry land. Upon reaching the extreme downstream end, the water exits the basin into a catch reservoir which can be drained back into the harbour area via return lines after completion of each test run.

5.1.2 Instrumentation

Four capacitance-type wave gauges (Kenek Co., Ltd., Japan) were installed to capture temporal variations in the water surface elevation at different locations in the basin. Wave gauges (WG) 1 and 2 were positioned at longitudinal locations inside the harbour area for which the gathered data could be used to assess changes in the wave form as it propagates through the basin. In a similar way, WG3 and WG4 were installed in the initially dry harbour area for which the collected data could be used to assess bore transformation as it progressed inland. Prior to the start of testing each day, the wave gauges were calibrated to known water levels yielding correlation coefficients greater than 0.99 (*i.e.*, acceptable error less than 1%). An electromagnetic current meter (ECM) was installed next to WG2 in the harbour area at a depth of 0.075m below the surface. In this way, the head of the measuring device was ensured to be submerged for the duration of the test, providing continuous fluid velocities over that time. Finally, the instrumentation was connected to a data acquisition system (VM-806H, Kenek Co. Ltd, Japan) set to sample the analog signals at a frequency of 100Hz. Exact locations of the instrumentation can be found in Figure 5.1.

5.2 Description of the Numerical Simulations

5.2.1 Computational Domain

Since three-dimensional effects in the basin are thought to be minimal, only a two-dimensional slice cutting through the center of the physical domain is considered for numerical simulation (see Figure 5.2). In doing so, the computational time can be kept within reasonable bounds while at the time ensuring mesh- and time step-independent results. The data acquisition system employed during the physical testing was only in operation once the target water depth in the hydraulic chamber had been reached and after any seiches induced in the basin had dissipated. Thus, the process of drawing the water into the chamber was not considered for the simulations (although it could be by applying appropriate pressure conditions at the boundary) and the temporal origin begins at the instant the water column inside the chamber begins to collapse. However, operation of the experimental testing did not necessarily follow the same protocol. Thus, the temporal origin of the experimental results was often unknown and not reference to any significant event occurring during the experiments (such as opening of the pneumatic valves). As a result, in some cases, the experimental results had to be shifted some arbitrary amount of time in order make a comparison with the numerical results feasible. This action was performed for the results at WG1 so that the arrival time of the crest of the first numerical and experimental wave were in agreement. This offset was then added to the experimental data collected at the three other wave gauges (WG2, WG3, and WG4) and the current meter (ECM1).

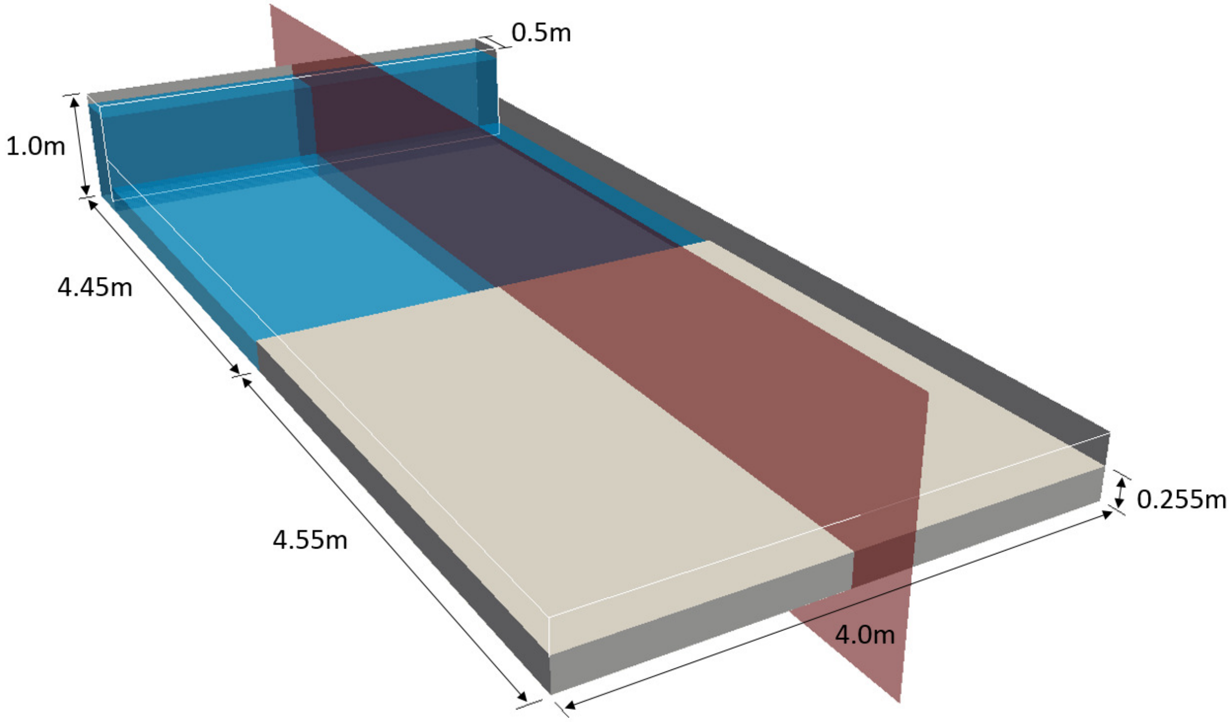

Figure 5.2: Initial configuration for simulating the hydrodynamics of the physical modeling conducted by Stolle et al. (2015). Red plane indicates the two-dimensional cross-section considered for mesh generation.

Numerical output of the model results for visualization purposes (animations, velocity distributions, and pressure fields) was performed at a frequency of 20Hz. However, specific results for comparing data collected at instrumented locations (time-histories of water surface elevation and point velocities at the ECM) was output every 5 time steps (somewhere in the range of 500-1000Hz depending on the maximum Courant Number at that particular time) in order to capture fleeting temporal variations in the field variables.

An image of the computational mesh used to perform the simulations is shown in Figure 5.3. The flow of the liquid phase was of primary interest, the mesh was extruded to remove as many grid cells near the top of domain that contained only the gaseous phase over the time frame considered. Using this a general rule of thumb, the height of the mesh in the hydraulic chamber was set equal to the target depth corresponding to the value used during the physical testing. In order to avoid adverse interaction between the liquid phase and the chamber boundary at the top of the domain, a single row of mesh cells was added to maintain the separation. The vertical piece of sheet metal that comprises the front face of the hydraulic chamber required special treatment below the elevation of the mesh in the harbour area immediately downstream. As can be seen in the magnified portion of the mesh shown in Figure 5.3, the front face of the hydraulic chamber was recreated by removing a single column of grid cells terminating at an elevation of 10cm above the basin floor. The remaining gap between the face of the hydraulic chamber and basin floor represents the outlet, through which the impounded volume of water exits upon opening the pneumatic valves. Based on numerical simulations performed on coarser meshes, the calculated maximum heights along the line of propagation were used to consecutively remove redundant grid cells along the top of the domain. As the waves reaches and overtops the quay wall separating the harbour and dry land, it undergoes a brief moment of shoaling which required local heightening of the mesh in this region. However, once the wave breaks and surges over the dry land, the bore becomes relatively shallow allowing a progressive thinning of the mesh moving from the quay wall to the basin outlet. To reduce the computational load, only the portion of dry land containing WG3 and WG4 was included in the discretized domain.

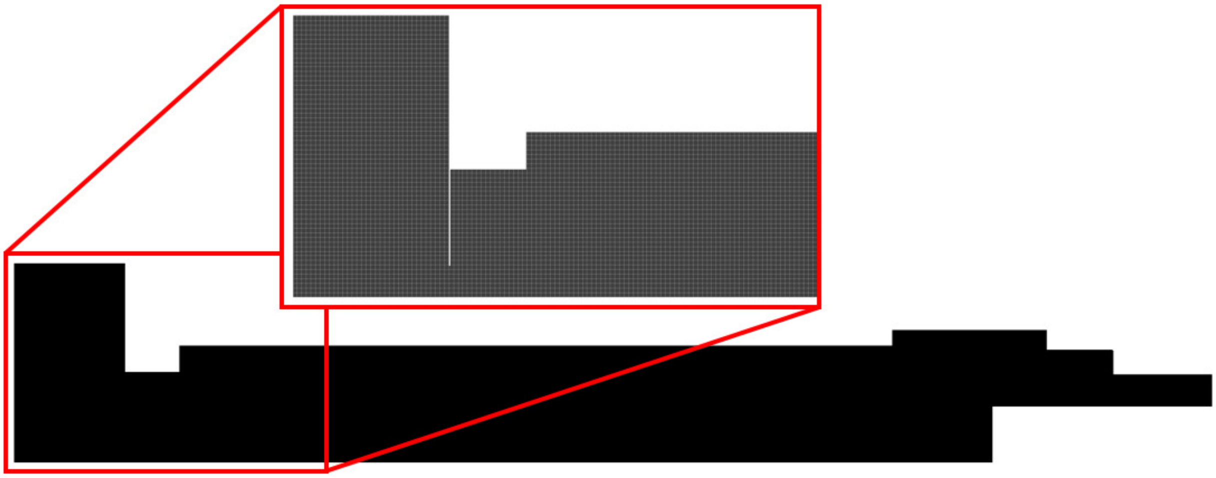

Figure 5.3: Optimized two-dimensional computational mesh generated for the TWB.

5.2.2 Initial conditions

Prior to releasing the water stored inside the hydraulic chamber, the system is at rest and so the choice for the starting conditions is straightforward. The internal fields for velocity and dynamic pressure are both set to zero. The initial distribution of the phase fraction was set to correspond to the depth of water in the hydraulic chamber and harbour area used during the physical test runs. Unless otherwise specified, the upstream and still water depth were set to h_u = 0.90m and h_d = 0.23m, respectively.

Convergence of the turbulent quantities can be accommodated by selecting reasonable initial values for the internal field. However, the solution for the turbulent quantities will converge to a given value independent of the initial guess, so the choice is not crucial. In this case, the turbulent kinetic energy $[m^2/s^2]$ and dissipation $[m^2/s^3]$ (for instances where a variant of the $k-\epsilon$ model is applied) are prescribed a small value of 0.1.

5.2.3 Boundary conditions

The *fixedFluxPressure* condition is applied to update the pressure field along the external boundaries representing the basin walls (*i.e.*, solid and impermeable surfaces). This formulation adjusts the spatial gradient of the pressure so that the flux along the boundary is consistent with the conditions prescribed for velocity. In this case, a no-slip condition ($\mathbf{U}$ = 0 m/s) is applied and the *fixedFluxPressure* condition is reduced to ensuring that the surface-normal pressure gradient is equal to zero. A *zeroGradient* condition is applied to the phase fraction along all boundaries. Turbulence parameters at solid boundaries are calculated using a smooth wall function based on law of the wall (*kqRWallFunction* and *epsilonWallFunction*).

The atmospheric (excluding the upper boundary inside the hydraulic chamber) and outlet boundaries are treated similarly. In both cases, the *totalPressure* boundary condition is applied on cell faces where a fixed value for total pressure equal to zero is prescribed. The *pressureInletOutletVelocity* is applied to these boundaries for calculation of the velocity field. This is essentially a *zeroGradient* condition imposed on the velocity that switches between explicit and implicit solution depending on the direction of the flow. At cell faces where the velocity is directed out of the domain, the solution is implicit and value for the velocity on the cell face is iteratively solved in the PISO loop (see Chapter 3). If the flow is directed inwards, the velocity is given explicitly as the value from the previous time step of the internal field normal to the inlet.

The treatment of the upper boundary inside the hydraulic chamber is a special case. Owing to the incompressible treatment of the gaseous phase, the pneumatic valves could not be modeled directly. The reason for this is because the air pressure inside the hydraulic chamber is, in reality, allowed to drop below atmospheric. As the water surface begins to fall, the volume of air inside the chamber is increased. Since, however, there is resistance imposed by the size of the valve openings, this change in volume is not necessarily balanced by an equal inflow of air, causing a reduction in air density (and thus pressure). When treating the air as an incompressible media (*i.e.*, changes in density are not permitted), it is not possible to simulate this behaviour directly. To model this behaviour, the pressure inside the tank can be imposed directly as a boundary condition in the form of a time-history. This feature will be used to calibrate the model to the experimental results and is further explored in section 5.3.2.

Finally, phase fraction is computed at inlets and outlets using an *inletOutlet* boundary condition. If the flow is directed out of the domain, the phase fraction is calculated using a *zeroGradient* condition. Conversely, if the flow is directed into the domain, the phase fraction is given a fixed value of zero (*i.e.*, only air enters through cell faces that behave as an inlet).

5.3 Calibration of Numerical Parameters

5.3.1 Maximum Allowable Courant Number and Mesh Resolution

In this section, the numerical model is tested for sensitivity to changes in the maximum allowable Courant Number (Co_{max}) and mesh resolution. Since the model applies the user-specified value of Co_{max} for adaptable time step control, varying Co_{max} is essentially just another way of testing the model sensitivity to temporal discretization. For a detailed description of the adaptable time step control, the reader is referred to Chapter 3. The findings in this section will be used to calibrate these numerical parameters to achieve mesh- and time step-independent results. In many cases, mesh resolution and time step sensitivity analyses are performed independently. As will be shown, however, achieving mesh-independent results is often dependent on the value of Co_{max}. Likewise, the ideal time step can vary depending on grid node spacing. For these reasons, it was decided to provide the analyses on both mesh resolution and Co_{max} in a combined section.

In Figure 5.4, temporal variations in water surface elevation at WG1 are displayed for a set of various Co_{max} values with a uniform mesh resolution of 0.25cm. Simulations were performed by starting at a maximum allowable Courant Number of $Co_{max} = 2$ and was progressively divided in half until any further decreases would render the computational time unreasonable. The comparison provided in Figure 5.4 reveals numerous effects that the temporal discretization has on the results. Firstly, it is noticed that the generated wave arrives at earlier times for decreasing values of Co_{max}. At first, the translation of the signal toward the temporal origin is quite substantial. However, as Co_{max} approaches the smaller of the considered values, the difference in arrival time become less pronounced. As a result of the increased wave celerity, the rise and fall of the water surface during passage of the wave becomes more sudden. In addition to the increase in wave celerity, there appears to be a positive correlation between Co_{max} and wave amplitude. Although not as substantial as the observed changes in wave celerity, a 2.5-3% reduction in amplitude is observed with each successive reduction in Co_{max}. Unlike the changes in wave celerity, however, the reductions in wave amplitude

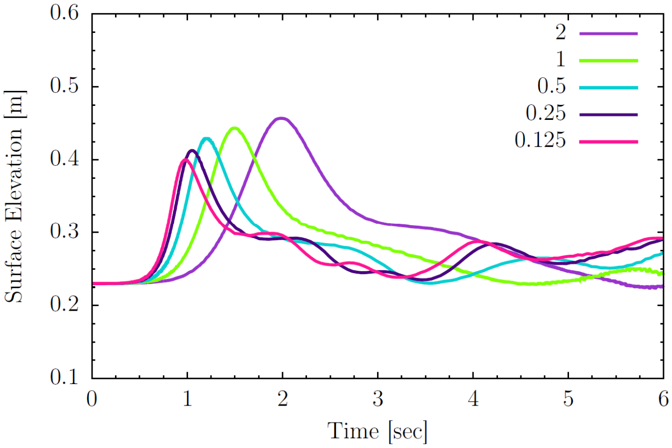

Figure 5.4: Comparison of time-histories of surface elevation at WG1 for various maximum allowable Courant Numbers at a uniform mesh resolution of 0.25cm.

Mesh Resolution (cm)	Co_{max}	No. Grid Cells	Computational Time (hours)
0.25	2	540,400	3.75
0.25	1	540,400	5.82
0.25	0.5	540,400	9.33
0.25	0.25	540,400	22.94
0.25	0.125	540,400	34.81

Table 5.1: Computational details of simulations performed for Co_{max} calibration. Simulation time = 6 seconds.

remained more or less constant with the changes made to Co_{max}. Computational details on the simulations performed to gauge sensitivity of the model to Co_{max} are provided in Table 5.1.

Based on the increasing computational effort accompanied with decreases in Co_{max}, it was decided to carry the insight gained from the previous tests to gauge sensitivity of the model to mesh resolution. Using a similar approach, grid node spacing of Δx = Δy = 1cm was considered first and was progressively divided by two (in each direction) until it was deemed that any further reductions would result in unacceptable computational times. By the time this condition was met, simulations were performed on three different meshes with varying grid node spacing. The influence of grid the node spacing on water surface elevations at WG1 is evident in the time-histories provided in Figure 5.5. In Figure 5.5-a, the results from the three different meshes at a maximum allowable Courant Number of Co_{max} = 1 are displayed. Here, it is observed that decreasing the grid node spacing tends to have the opposite effect of decreasing the value of Co_{max}. When the mesh becomes more refined, the amplitude of the first wave arriving at WG1 is increased. Moreover, the arrival of the crest tends to occur at a slightly time. Although there is evidence to suggest that the amplitude is converging (smaller difference between Δx = 0.5cm and Δx = 0.25cm than Δx = 1cm and Δx = 0.5cm), the shift in arrival time does not appear to show the same behaviour. This is in precise contrast to what was observed while varying Co_{max}.

When the same sensitivity analysis on mesh resolution is performed at a Co_{max} = 0.125, the contrasting tendencies that are observed when varying these two parameters tend to balance each other out. Evidence of this is provided in Figure 5.5-b where the influence of mesh resolution is strikingly less perceptible. As a result of the ideal temporal discretization, the grid node spacing no longer influences the arrival time of the first wave. Changes in the wave amplitude are still visually perceptible between the two most extreme cases (Δx = 1cm and Δx = 0.25cm), however, between the two more refined cases the difference is less than 2%.

Thus, a high degree of confidence is had in achieving mesh- and time step-independent results by applying the mesh with grid node spacing of Δx = Δy = 0.5cm in combination with a maximum allowable Courant Number Co_{max} = 0.125. In making this selection, the substantial jump in computational time from 6.81 hours to 34.81 hours is avoided (see Table 5.2) while still maintaining the assurance of obtaining reliable results.

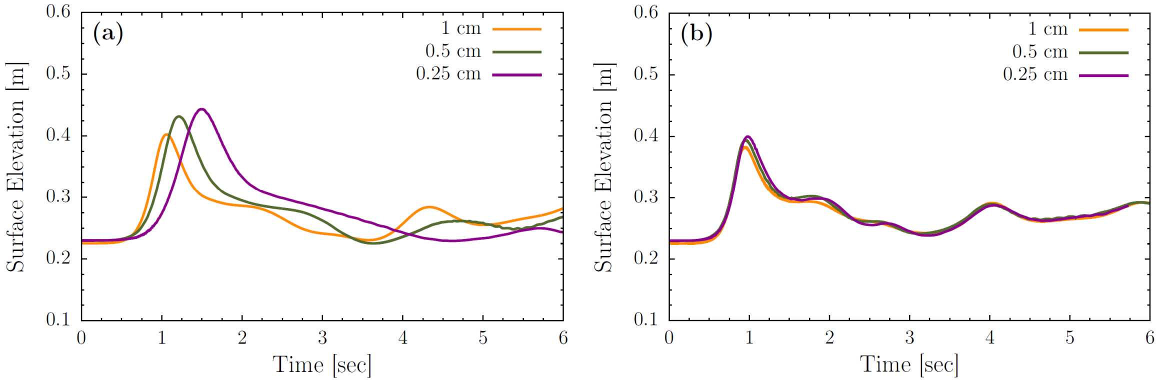

Figure 5.5: Comparison of time-histories of surface elevation at WG1 for various uniform mesh resolutions with a maximum allowable Courant Number of (a) Co_{max} = 1 and (b) Co_{max} = 0.125.

Mesh Resolution (cm)	Co_{max}	No. Grid Cells	Computational Time (hours)
1	1	32,420	0.04
0.5	1	139,400	0.43
0.25	1	540,400	5.82
1	0.125	32,420	0.30
0.5	0.125	139,400	6.81
0.25	0.125	540,400	34.81

Table 5.2: Computational details of simulations performed for mesh resolution calibration. Simulation time = 6 seconds.

5.3.2 Chamber Pressure Boundary Condition

As mentioned above in the section regarding boundary conditions, it was not possible to directly simulate the effect of the pneumatic valves installed along the top of the hydraulic chamber. Wave generation via the pneumatic principle is driven by two counteracting forces. The first one is gravity, acting to equalize the differential water levels between the hydraulic chamber and wave propagation section. The second force, counteracting the gravity, is the subatmospheric pressures generated inside the tank as an indirect result of the resistance of airflow into the tank (controlled by valve opening settings). Although the change in pressure induced by the resistance cannot be directly simulated, the pressure inside the tank can be controlled by assigning appropriate boundary conditions to the roof of the hydraulic chamber. Since no pressure measurements were taken inside the chamber during experimental test runs, the modeler is left to speculate on how the pressure behaves over time. Fortunately, the start and end values for the pressure can be known with certainty. In order for the pneumatic pump to draw a column of water such to create a hydraulic head of 0.67cm (h_u = 0.90m and h_d = 0.23m), the generated vacuum must exert a pressure (relative to atmospheric) of $p = -0.67$m * 9810 N/m^3 = −6.573 kPa. At some point after the release, the differential pressure between the inside and outside of the chamber will eventually equalize to a final value of p = 0 kPa, relative to atmospheric. The two unknowns, however, remain to be:

- The length of time required for the pressure to equalize, and
- The behaviour of the pressure between the start and end points.

Although both could be used a calibration parameter, the number of possible combinations to consider would be too numerous for testing. In a previous study conducted by Allsop et al. (2014), a hyperbolic tangent function was applied to model the pressure inside the tank of their second generation tsunami simulator. In order to reduce the number of unknowns, this concept was borrowed and applied to the current numerical work and the length of time required for the pressure to equalize was adopted as the calibration parameter. Including the freefall case (roof of hydraulic chamber is completely open to the atmosphere), the time-histories of pressure considered for the hydraulic chamber boundary condition (pBC) are provided in Figure 5.6.

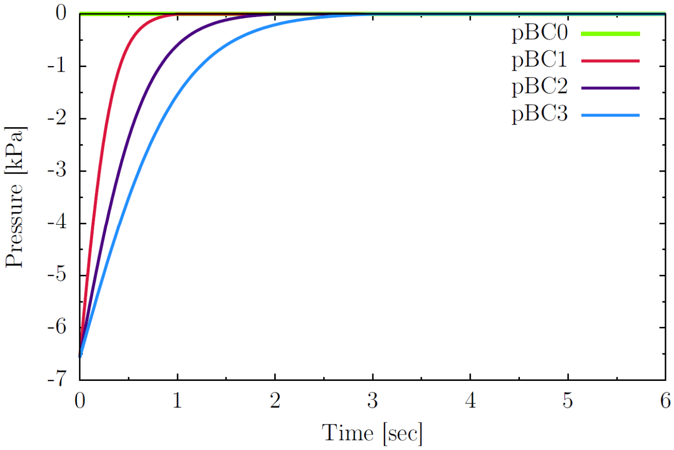

Figure 5.6: Time-histories of the pressure boundary condition (pBC) applied along the roof of the hydraulic chamber.

The calibrated hydraulic chamber pBC was selected by comparing numerical wave heights to experimental data collected at WG2. A comparison of the temporal variations in surface elevation at this location (see Figure 5.1) for the four hydraulic chamber pBCs considered is given in Figure 5.7. As expected, the subatmospheric pressure induced inside the tank reduces the initial wave height and causes a delay in the wave arrival time. This effect appears to be compounded with increasing length of time for the pressure between the tank and atmosphere to equalize. As mentioned in section 5.2.1, the temporal origin of the experimental data was not referenced to any distinguishable event, making comparisons of numerical and experimental wave arrival times (at least at WG1) futile. Rather, the numerical time-histories are compared to the target wave height alone (derived from the experimental data at WG2) in order to select the ideal hydraulic chamber pBC before temporally referencing the experimental data. From the visual comparison, it is clear that the wave height produced by applying pBC3 is in near-perfect agreement with the target wave height. Thus, hydraulic chamber pBC3 was selected to be applied for subsequent simulations.

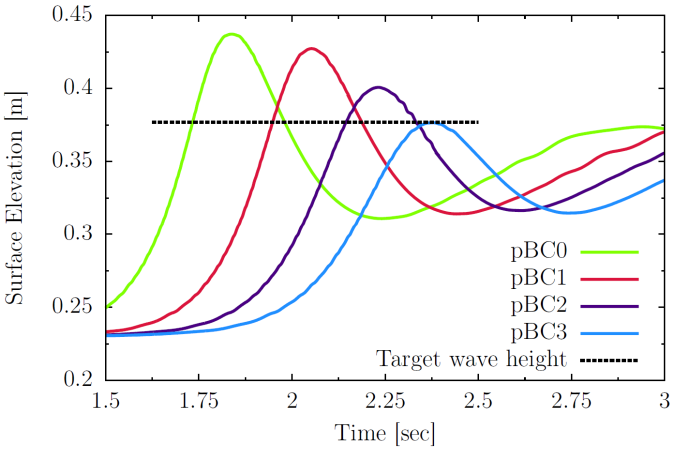

Figure 5.7 Time-histories of water surface elevation at WG2 for various the various pressure boundary conditions applied to the hydraulic chamber.

It is important to note, however, that this pBC is only calibrated to results obtained from a specific experimental setup. If one were to apply any numerical modifications, for example, to the outlet dimension or hydraulic head, recalibration of the pBC would be required. However, since experimental data is only available for a very limited number of setups, recalibration is not feasible in most cases. Thus, in cases where numerical modifications are made that may influence the rate at which the water level changes inside the tank, pBC0 is applied. In any case, the pBC applied to the hydraulic chamber will be explicitly stated in the discussion.

5.3.3 Turbulence model

In order to quantify the effects of turbulence treatment on the results, the standard, realizable and RNG $k-\epsilon$ models were considered. In Figure 5.8, the computed time-histories of surface elevation at WG2 using the three different turbulence models are compared to the experimentally-measured data. The first disparity noticed is a slight change in the initial wave height. Since the standard $k-\epsilon$ model was used during calibration of the pBC, it is of no surprise that it agrees most with the experimental data. However, because it is simple to backtrack and adjust the chamber pBC, the agreement of the initial wave height is neglected in selecting an appropriate turbulence treatment. Of more interest in the comparison is the agreement between the finer details of flow which are revealed in the experimental time-history. In particular, the distinguishable secondary wave (just before $t = 3$ seconds) that appears to trail by after passage of the initial wave. In the case of the standard and realizable $k-\epsilon$ model, there is no evidence that this secondary wave is being produced. The RNG $k-\epsilon$ model, on the other hand, appears to recreate this behaviour, albeit not as pronounced as it appears in the experimental data. Since there were no major discrepancies between the numerical and experimental time-histories that would have been reason to preclude any one turbulence treatment in particular, the RNG $k-\epsilon$ model was selected based on its ability to reproduce the secondary wave.

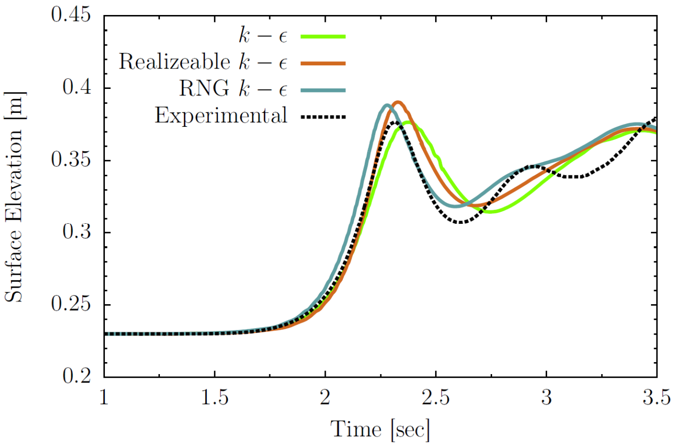

Figure 5.8: Comparison of experimental and numerical time-histories of water surface elevation using various turbulence models.

5.4 Comparison of Experimental and Numerical Results

5.4.1 Water Surface Elevation

Full simulations were performed using the calibrated numerical parameters for comparing the computed and experimental results. Over the course of numerous physical test runs, a certain degree of natural variability was noticed in the measurements. The cause of the variability is likely the compound effect of several different sources. In between several sets of the measurements taken, the water in the TWB was drained for instrument recalibration, modification to testing configurations, or simply to prevent water damage over several days of dormancy. The cycle of draining and filling sometimes lead to small variations in the total volume of water contained in the basin. Consequently, the still water depths in the harbour region for propagating the wave to the shoreline included an approximate error of ±0.01m. Moreover, perturbations to the initial conditions (residual motion in the tank, synchronization of pump shut-off with valve opening, etc.) may also add to the variability. In each case, basic statistics on the experimental measurements are performed. Where applicable, the mean value along with the lower and upper bounds representing the most extreme measurements taken at that time are plotted.

In Figure 5.9, temporal variations in the water surface elevation are compared at the four wave gauge locations (see Figure 5.1). Although WG2, WG3, and WG4 are located in a different longitudinal plane as WG1, it is thought that three-dimensional and sidewall effects are minimal in the basin. Thus, the cross-basin location (y-direction) at which the measurement is taken should not bear too much influence on the outcome. It is for this reason that it is assumed valid to compare the two-dimensional numerical results to the physical measurements at corresponding longitudinal locations.

With the exception of the arrival time of the reflected wave occurring at $t = 4.5$ seconds in Figure 5.9-a, reasonable agreement is observed between the simulated and experimental results. Up until shortly after passage of the wave crest, the waveform closely resembles that of a solitary wave described by Munk (1949). However, as the wave progresses toward the shore, the water exiting the hydraulic chamber ceases to continue building the initial wave. Until the differential head is reduced to zero, the additional water entering the harbour area gets deposited at an increasing distance behind the initial wave. After a short time following passage of the initial wave crest, the waveform begins to trail off and decline at a substantially slower rate than that observed during the initial increase. The resulting waveform can be characterized as a solitary-like leading wave with a long trailing tail.

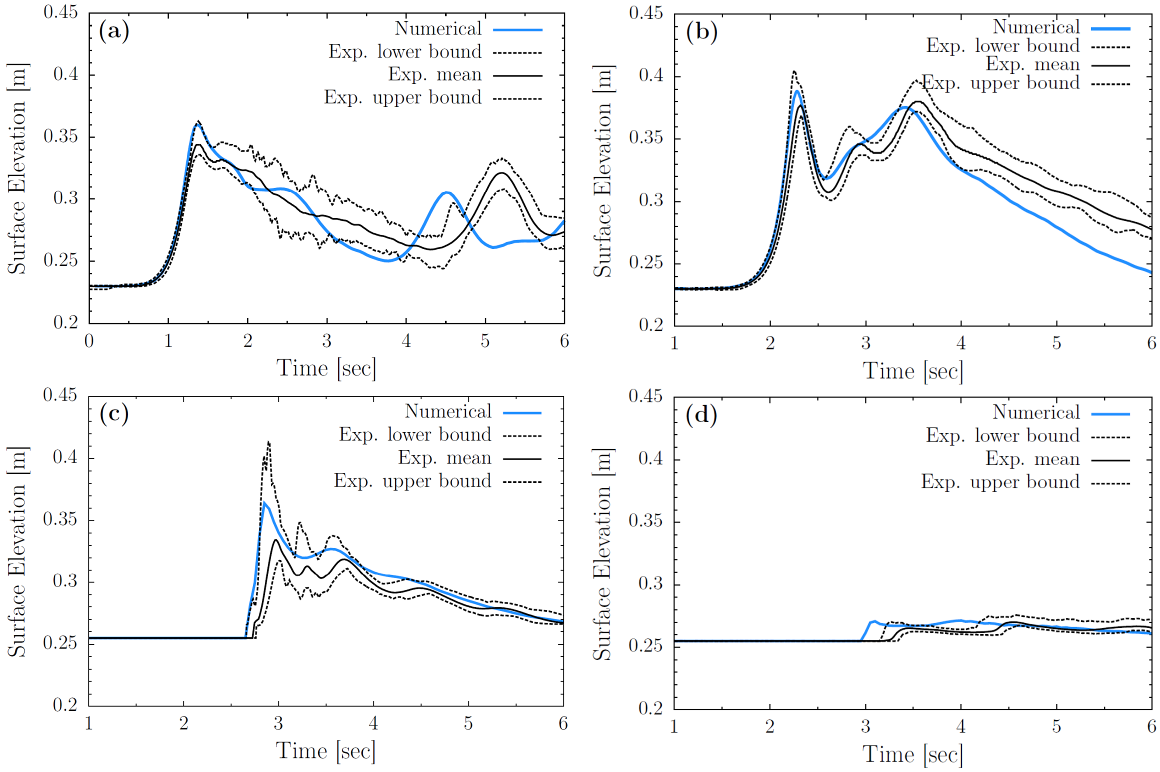

Figure 5.9: Comparison of experimental and numerical time-histories of water surface elevation at (a) WG1, (b) WG2, (c) WG3, and (d) WG4.

Although comparison of the arrival time of the initial wave at WG1 is not possible due to the required temporal referencing, the same translation was performed on the data at WG2, WG3, and WG4, making celerity comparisons possible. It can be seen at WG2 in Figure 5.9-b that the numerical and experimental waves arrive at approximately the same time and have increased in amplitude by a small amount since passing WG1. It appears also that the leading solitary wave is beginning to separate from its tail, leading to a more pronounced crest. However, since WG2 is much closer to the quay wall than WG1, the length of time separating the passage of the incident and reflected wave is substantially reduced. In fact, the reflected wave begins to pass WG2 before the tail even arrives such that when it does it is nearly imperceptible in the time-history. The only visible evidence of the tail in the temporal variations at WG2 is the secondary wave with the crest passing just before $t = 3$ seconds. As described earlier, the RNG $k - \epsilon$ model was selected based on its ability to reproduce this detail, however, it is clear that the physical secondary wave is more prominent. The amplitude of the reflected wave occurring in the simulation at approximately $t = 3.5$ seconds appears to be in good agreement with the experimental mean value, although it arrives at WG2 about 0.15 seconds earlier. After the crest of the reflected wave moves beyond WG2, a relatively smooth and consistent decline in surface elevation is observed. Beyond $t = 4$ seconds, the numerical surface elevation appears to fall below the lower bound of the experimental data and declines at a slightly quicker rate, resulting in an increasing discrepancy over time.

The simulated water levels at the first gauge that the wave encounters on dry land (WG3, Figure 5.9-c) tends to show a similar trend that is displayed in the experimental data. First, a sharp increase in the water level is observed in association with the leading solitary-like wave overtopping the quay wall. Following passage of the initial crest, an equally steep decline in the surface elevation occurs until the secondary wave arrives and causes another brief moment of increasing inundation depth. Although the occurrence of the secondary wave was unintended, the evidence at WG3 suggests that it may influence phenomenon being studied on the initially dry land, such as the motion of debris fields. Good agreement between the numerical and experimental surface elevations is observed during the subsequent decline in water levels after the secondary wave has passed.

In Figure 5.9-d, at the furthest inland point at which surface elevations were measured, the bore is fully collapsed and displays relatively smoother variations in water depth over time. It is seen that the leading edge of the numerical bore reaches WG4 approximately 0.25 seconds earlier than that observed during the physical tests. This indicates perhaps the numerical surface imposing slightly less resistance to advancement of the bore than the marine plywood-constructed false floor used for the experiments. The maximum inundation depths at this physical location are relatively minimal, reaching only 1.5-2cm in the case of both the numerical and experimental measurements. Once the leading edge of the wave arrives, the water levels remain relatively constant with only minor fluctuations visible until the end of the simulation. Again, evidence of the secondary wave is seen at the 4 and 4.5 second mark for the numerical and experimental data, respectively, indicating potential influence on inland processes.

Since the wave transformation over the quay wall may play an important role in setting up the dynamics during inland intrusion, a qualitative comparison of this process is provided in Figure 5.10. For each of the three rows of panels, a two-dimensional pressure field in the liquid phase is given along with a corresponding still-frame of a video taken during the physical test when the wave was at a similar position. In the experimental still-frame, the outline of the initial wave is traced in yellow to enhance the clarity of its shape as it overtops the quay wall. In first set of still-frames (Figure 5.10-a and Figure 5.10-d), the wave crest is approximately 0.20m seaward of the quay wall and has begun to spill over onto the dry land. At this point, the waveform begins to evolve as the orbital velocities are halted against the quay wall, compressing in length and growing in height.

The wave reaches its maximum amplitude and steepness when the crest is approximately overhead of the vertical drop, captured in Figure 5.10-b and Figure 5.10-e. Just prior to this instant, the face of wave occurring in the physical basin becomes nearly vertical. In the experimental still-frame provided, the wave begins to collapse and displays a concave profile from the leading edge to the crest. The computed wave does not appear to become quite as steep and maintains its predominately convex profile as it surges over the wall. A region of subatmospheric pressure develops near the edge of the quay wall on the landward side of where the boundary layer separates from the vertical face.

Although made clearly evident in the computed pressure field, this feature is also visible in the experimental still-frames as a tube of entrapped air extending along the edge of the false floor. The fluid velocities contained in the small vortex must have entrained the air when the leading edge began to overtop the wall and were strong enough to suspend it in place before the wave completely collapsed.

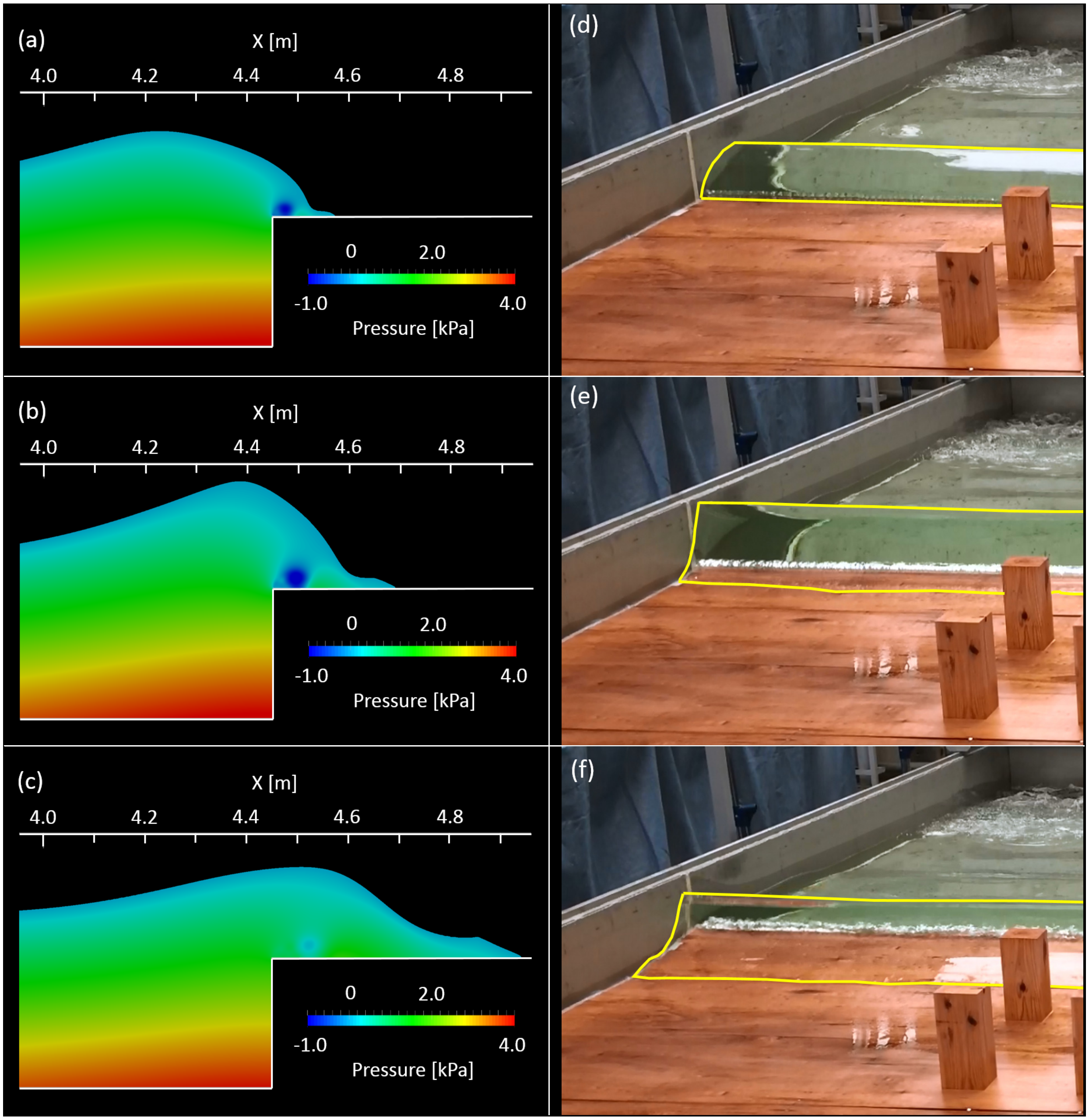

Figure 5.10: Qualitative comparison of numerical and experimental wave transformation over the quay wall: (a) Time: 2.55 seconds, (b) Time: 2.65 seconds, and (c) Time: 2.8 seconds after release. (d, e and f) correspond to a similar stage of the wave transformation given in (a, b, and c), respectively. (Photographs couresty of Dr. Ioan Nistor)

By the time shown in Figure 5.10-c and Figure 5.10-f, the surge front has increased in depth by a significant amount as a result of the initial wave nearing complete collapse. The rotational velocities contained inside the small vortex at the edge of the quay wall have weakened, evidenced in Figure 5.10-c by the relatively higher pressure and in Figure 5.10-c by the gradual breaking up of the entrapped tube of air. Shortly after the still-frames shown, the initial wave further spreads out and begins to run off the downstream end into the catch basin. Overall, with respect to the experimental observations, the numerical model is able to reproduce the wave transformation process over the quay wall reasonably well.

5.4.2 Velocity

Velocity data collected by the ECM located in the harbour area approximately 0.80m seaward of the shoreline is compared to the simulated values in Figure 5.11. In general, the numerical model appears to be capable of reproducing the temporal variations captured by the ECM with reasonable accuracy. The initial rise, peak, and beginning of the decent of the numerical stream-wise velocities are observed to be in almost perfect agreement with the experimentally-measured values. At approximately t = 2.75 seconds, the velocity measured during the experiments appears to undergo a second momentary increase as the crest passes over the ECM. Although the numerical signal does show the same tendency, the secondary wave was less distinguishable and hence its effect on the velocity at the instrumented location was relatively weaker.

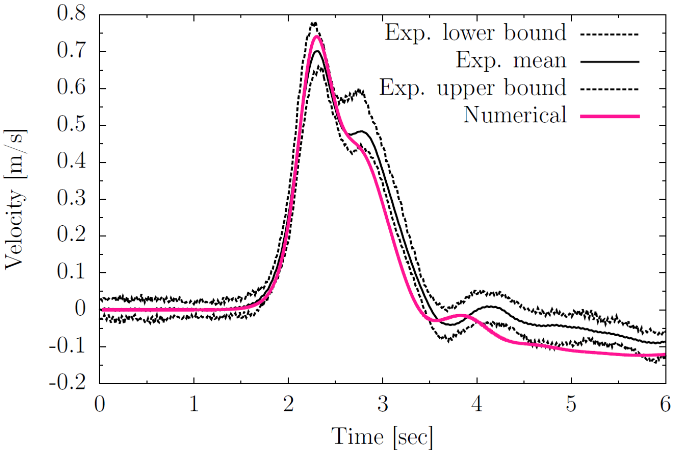

Figure 5.11: Comparison of numerical and experimental time-histories of x-velocity at ECM1.

At approximately the same time that the crest of the reflected wave arrives at the ECM, the shoreward transport of water is reversed and a return flow towards the hydraulic chamber is initialized. The arrival of the reflected wave is characterized by the dip in velocity occurring at approximately t = 3.5 and 3.75 seconds in the case of the numerical and experimental results, respectively. After passage of the reflected wave, the velocity appears to continue increasing by small amounts towards the hydraulic chamber as the wave proceeds through its draw back phase. Eventually, the seaward transport of water observed near the end of the simulation causes another set up of water levels in front of the hydraulic chamber, albeit smaller than the preceding one occurring at the shoreline. This, in turn, creates an oscillatory motion inside the harbour known as a seiche. After a few cycles, the long wave reflecting between the hydraulic chamber and quay wall dissipates and the system comes to a rest.

In Figure 5.12, the wave formation process is visualized through a temporal sequence of velocity fields plotted near the upstream end of the wave basin. To make the features of the process more easily discernible, the results shown here were generated by allowing the contents of the chamber to drain without any resistance imposed by subatmospheric pressures inside the tank (*i.e.*, pBC0 is applied to the hydraulic chamber). It takes approximately half a second for the water level inside the chamber to drop its first 0.1m by which time a single, symmetrical wave has formed inside the harbour area (seen in Figure 5.12-a). The high velocity jet of water exiting the chamber dissipates quickly and transfers its momentum to the initially still water. For a short while, the jet continues to feed the initial mound of water that develops in front of the tank. As the roughly symmetrical wave begins to move shoreward under the influence of gravity, however, the jet cannot continue to deliver water to the main body of the wave. Since it can only reach so far before dissipating, the wave tends to elongate through the addition of water to its back end, seen in Figure 5.12-b. The observed elongation of initial wave may also be exacerbated by the tendency of the main wave to disperse into spectral components (soliton fission), forming a train of waves. This tendency has also been documented by other researchers employing similar techniques for long wave generation (*e.g.*, Lukkunaprasit et al., 2009 and Allsop et al. 2014). At the same time, the currents generated at the back end of the wave appear to begin influencing the behaviour of the jet. In Figure 5.12-b, the jet appears to get pinched or cutoff beneath the trough trailing behind the initial wave. Consequently, the elongated wave becomes severed from the supply line of additional water stemming from the hydraulic chamber. Since it has not finished emptying by this time, another, smaller mound of water begins to form at the mouth of the outlet. Further evidence of the dispersiveness of the initial wave is observed in Figure 5.12-c, where two distinct wave crests are visible which used to be parts of the initial coherent mound. Since the leading wave, with its larger wavelength and amplitude, travels with a greater celerity, the distance separating the first from the second and third waves continues to grow, evidenced by the profile given in Figure 5.12-d.

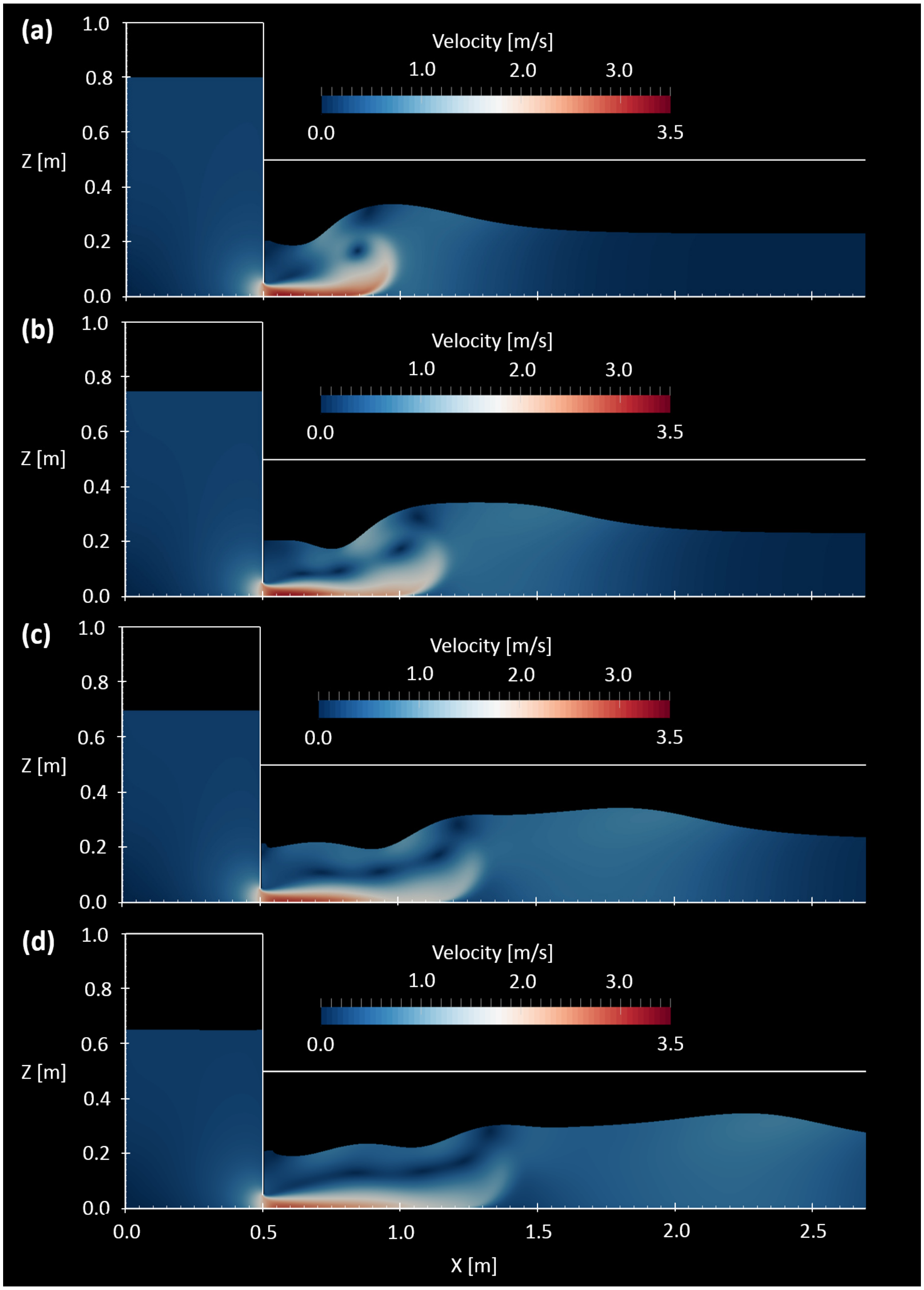

Figure 5.12: Velocity fields during long wave generation at (a) Time: 0.5 seconds, (b) Time: 0.75 seconds, (c) Time: 1.0 seconds, and (d) Time: 1.25 seconds.

5.5 Results of Numerical Experiments

5.5.1 Influence of Chamber Outlet Dimensions

In this section, the height of the outlet (h_o) connecting the hydraulic chamber to the harbour area is modified to gauge the influence it has on the numerical results. Both a smaller (h_o = 0.05m) and larger (h_o= 0.15m) value relative to the existing value h_o = 0.10m are considered. Since the rate of change in surface elevation inside the chamber is likely to be influenced by the outlet dimensions, ideally, a different pBC for the roof of the tank should be selected for each case. However, in the absence of the experimental data with the same configuration, it was not possible to calibrate new pBCs for a given pneumatic valve setting. Instead, simulations were performed assuming the chamber roof was completely open to the atmosphere and that no resistance was imposed to the inflow of air. As such, the air pressure inside the chamber was maintained at atmospheric over the duration of tests for all cases considered (*i.e.*, pBC0 is applied).

Changes in the behaviour of the fluid inside and exiting the hydraulic chamber in response to the outlet height adjustments are captured in Figure 5.13. In particular, Figure 5.13-a compares the time-histories of surface elevations for each case inside the hydraulic chamber. It is observed that at the instant the column of water inside the chamber is released, the water levels begin to decline at an approximately linear rate. Not surprisingly, the rate of volume transfer from the chamber to the harbour area is reduced when the outlet is made smaller, evidenced by the slower rate of decline in surface elevation for h_o= 0.05m. Contrarily, the rate of decline is increased when the outlet is made larger relative to existing. Despite the two additional outlet sizes tested being equidistant (±0.05m) from h_o = 0.10m, the reduction of the outlet height appears to have a disproportionately larger influence on water levels in the chamber.

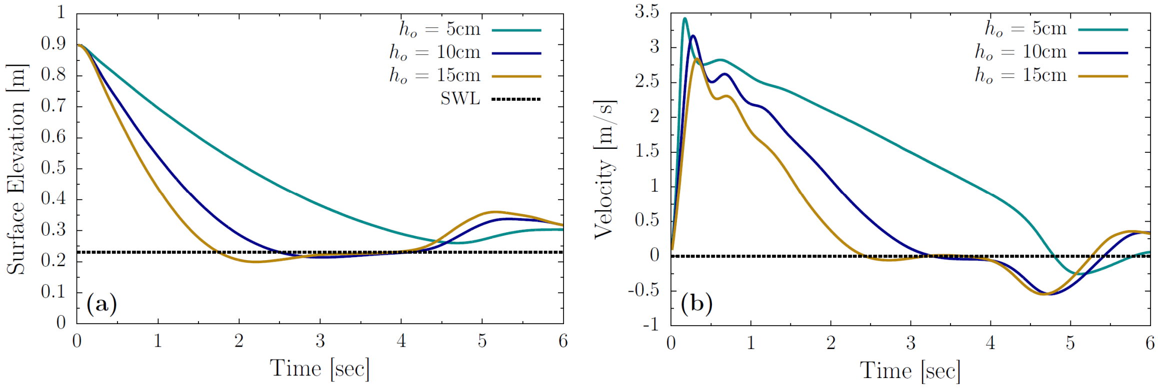

Figure 5.13: Influence of outlet dimensions on time-histories of (a) water surface elevation inside the hydraulic chamber and (b) flow velocity through the outlet. SWL = still water level.

In the case of h_o = 0.10 and 0.15m, the momentum of the collapsing water column causes the surface elevation inside the chamber to drop momentarily below the still water level (SWL), seen between t = 1.75 and 3.5 seconds. It is also observed that the flow velocity exiting the chamber becomes slightly negative a short time after the surface elevations dip below the SWL in Figure 5.13-b. At some point after t = 4.5 seconds, the return flow back into the chamber becomes strongest when the crest of the reflected wave arrives at the upstream end of the basin. Afterwards, an oscillatory behaviour in the outlet velocity is established, jumping between positive and negative values until the continuously reflected wave dissipates.

Just prior to when the initial wave begins to feel the presence of the quay wall, the water surface profiles revealing the waveforms generated using the three different outlet heights are provided in Figure 5.14. Although the profiles exhibit similar trends, the main differences lie primarily within the characteristics of the leading wave. Due to the relatively higher discharge leaving the chamber in the case of h_o = 0.15m, the jet is able to supply the leading wave with a greater volume of water before the distance separating the two becomes too large. In Figure 5.14, it is clear that a majority of the additional volume of water contained in the waveforms for the larger outlet heights is contained in the leading wave. The elevation difference between the two initial wave crests for the two extreme outlet heights is roughly 0.11m. At no other point in the profiles does the elevation difference come even close to this value. Take, for example, the trailing tails behind the initial wave. In all three cases, the difference in elevation is extremely minimal. The most notable difference, initial wave amplitude aside, is perhaps the secondary wave occurring just before x = 1.5m. In this case, the amplitude of the secondary wave appears to be reduced with decreasing outlet height. In fact, the secondary wave in the wave profile generated using h_o = 0.05m shows only minimal deviation from the tail connecting it to the leading wave.

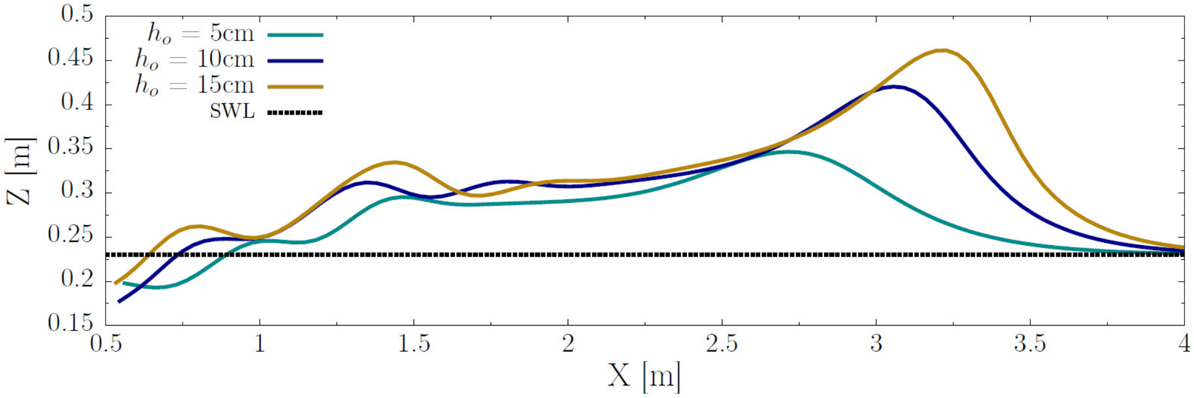

Figure 5.14: Comparison of wave profiles at t = 1.5 seconds for three different chamber outlet heights.

5.5.2 Influence of Still Water Depth

By maintaining all other aspects of the configuration, numerical experiments were conducted to investigate the effect of still water depth on propagation and inundation characteristics. Since the hydraulic head was preserved for each of the simulations, the rate in decline of surface elevations inside the chamber is assumed to be minimally effected. In this way, the pBC that was calibrated to the physical results could be confidently applied to control the pressure inside the chamber. Thus, the results presented here should be physically relevant given the same pneumatic valve setting used during the experimental testing.

In Figure 5.15, wave profiles are compared at three different times for still water depths of h_d = 0.23 (existing), 0.40, and 0.60m. In the first comparison (Figure 5.15-a), the wave profiles are shown at a time just before they begin to inundate the coast. It is clear from the superposition of the elevation profiles at this time that the still water depth has a significant effect on the wavelength of the initial disturbance. The wave crests seen at approximately x = 2.75m all appear to be in good alignment, suggesting the wave celerity is largely unaffected. In the case of still water depth h_d = 0.23m, the water surface directly adjacent to the quay wall (drawn as the solid black line) remains at the initial SWL. At the other extreme (h_d = 0.60m), however, water levels are seen to have already risen to point to where overtopping of the quay wall begins. The reason for this observed discrepancy can likely be attributed to depth-limited propagation speed at which the initial disturbance tries to spread out. Neglecting the influence that the secondary wave has on the steepness of the profiles on the leeside of the initial crest, the differences are fairly minimal. Since, however, the disturbance is propagating in the direction of the shore, the crest tends to lose less distance to the toe of the wave compared to the heel. As a result, the increasing bottom friction for shallower still water depths causes a steepening of the front face of the wave. Since the wave steepness is such a crucial aspect to consider in the modeling of tsunamis (Heitner and Housner, 1970), careful consideration should be given to the selection of the still water depth.

By the time the wave crests arrive at the quay wall (see Figure 5.15-b), in all three cases, the wave fronts have steepened considerably. Since, however, in cases with deeper still water depths, the toe of the wave overtops the wall at an earlier time and so the surge has advanced further inland. Seward of the wave crests, the profiles of the two longer waves remain at higher elevations than the in the case of the shorter wave, potentially foreshadowing longer inundation periods.

Quickly following the movement of the wave over land, the initial crests collapse and the profiles take on a smoother definition. Since this collapse process is entirely driven by gravity, the bore fronts that were generated from initially higher crests (smaller h_d's) have a higher celerity. As a result, the distance between the bore fronts seen in Figure 5.15-b is closed and they become collocated by the time depicted in Figure 5.15-c. Due to the additional turbulence generated in the faster-moving bores, the front celerities tend to equalize after a short distance and move together at a similar pace. In addition, the various still water depths considered do not appear to influence other bore characteristics such as the surge depth or steepness, at least after the initial wave has fully collapsed.

A noteable difference observed between Figure 5.15-b and Figure 5.15-c seaward of the quay wall (2.75m $< x <$ 4m) is that the order of the different cases in terms of surface elevation appear to have been reversed. In fact, the reason for this is directly related to wave reflection off of the quay wall. In cases with waves of higher amplitudes and short wavelengths (decreasing h_d), a greater portion of the wave energy is reflected. This is particularly visible in Figure 5.15-c for the still water depth of 0.23m where the crest of the reflected wave is at approximately x = 3m. Shortly after the time shown in Figure 5.15-c, the water levels just seaward of the quay wall are restored to the order seen in the preceding frame (Figure 5.15-b).

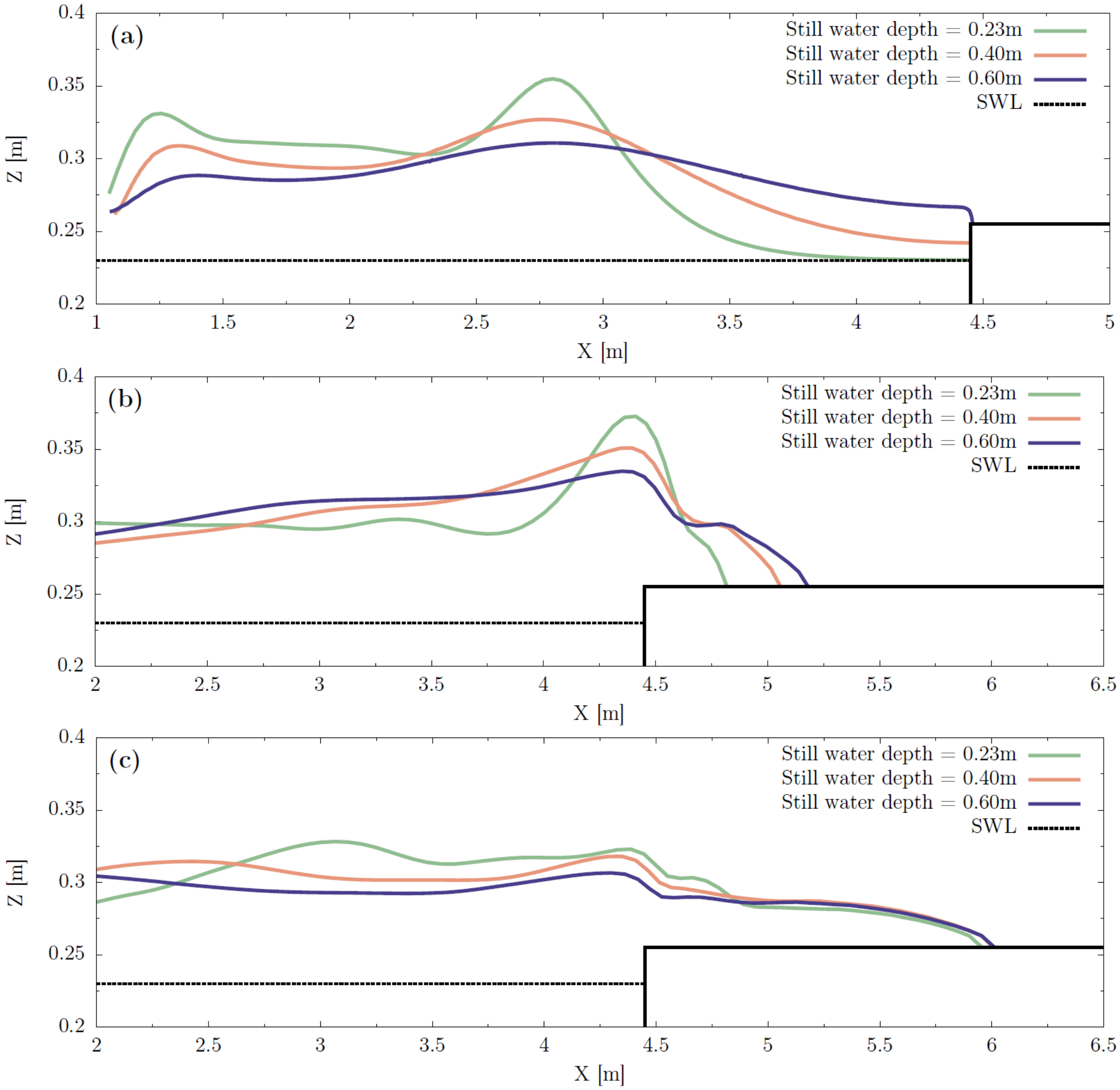

Figure 5.15: Comparison of wave profiles for three different still water depths at (a) Time: 1.5 seconds, (b) Time: 2.5 seconds and (c) Time: 3.5 seconds.

The temporal variations in surface elevation at WG2, as shown in Figure 5.16-a, captures a few of the abovementioned effects that different still water depths have on the results. For instance, at the beginning of the time-history, water levels begin to rise much earlier and at slower rates for deeper still water depths. Although the initial crest heights are effected in a small way, the most remarkable difference is related to the rates of rise and fall of the surface. In the case of h_d = 0.23m, the initial wave passes WG2, almost entirely, before the reflected reaches the same location (seen as the relatively deep trough occurring between t = 2 and 3 seconds). The temporal change in surface elevation between these two events is reduced substantially when the still water level is increased. This is the result of both a reduction in the reflected energy but becomes further obscured by the increased wave lengths. In this case, the incident wave is still passing WG2 at the time the reflected wave arrives, effectively reducing the appearance of its true size in the time-history. Interestingly, the time-histories of water levels at WG4, shown in Figure 5.16-b, do not appear to show any substantial differences at all. The only visible difference to point out is that the arrival time of the secondary wave appears to be shifted to later times for increasing still water depths. It is surprising, however, to not find that the inundation length was reduced for the shorter wave lengths (in particular the case of h_d = 0.23m). An important aspect to note at this point is that there may have been some secondary effects in the basin that are causing increased inundation lengths independent of the wavelength. A quick calculation shows that the additional water added to the harbour area by releasing the contents of the chamber is sufficient to fill the harbour area to the rim of the quay wall, plus an additional ~2.5cm of water covering the entire surface area of the basin (including the dry land). This water has nowhere else to go except to flow over the land and into the catch basin at the downstream end. Consequently, the influence of the wavelength on aspects such as the timescale of inundation may be overridden by the fact that this additional water is going to evacuate the basin over the initially dry land. Ideally, the timescale of inundation would be controlled directly by the form of the wave and not by these secondary effects. Consideration should be given to this for future physical tests.

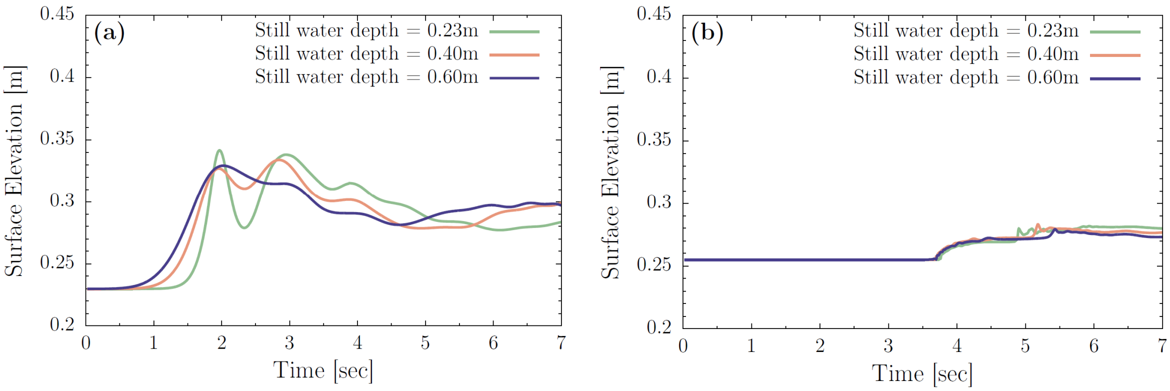

Figure 5.16: Influence of still water depth on time-histories of surface elevation at (a) WG2 (x = 3.65m) and (b) WG4 (x = 6.15m).

To gain insight as to how the overland flow velocities may be indirectly effected by changes to the still water depth, time-histories of the streamwise current are plotted at x = 5.0 and 6.15m in Figure 5.17-a and Figure 5.17-a, respectively. At locations closer to the seawall (Figure 5.17-a), fluid velocities contained inside the bore front are influenced by the collapse of the initial wave. Since waves with greater amplitude (caused by shallower still water depths) contain within them greater amounts of gravitational potential energy, the resulting kinetic energy caused by their collapse is proportionately increased. The greatest difference in fluid velocity is observed at the instant the bore arrives at the probed location. Between the two most extreme cases, the difference is upwards of 0.5m/s which is relatively substantial when considering the absolute values. If the waveforms are being used to create hydrodynamic forcing on structures or initiating debris motion, these differences in bore front velocity may play an important role. The difference in bore velocity for the three different cases tends to converge just after t = 3 seconds for a brief moment before the second soliton arrives. Because the fission process was strongest in the case of the shallowest still water depths, a corresponding increase in velocity is observed upon its arrival just before $t = 4$ seconds. Following passage of the secondary wave, the trends appear to be similar, except in the case of $h_d = 0.60$m. The momentary increase observed in the velocity after $t = 5.5$ seconds is seemingly caused by the arrival of a reflected long wave off the face of the chamber. Since the celerity of the reflected wave is reduced for shallower water depths, it arrives later for the other two cases and thus does not appear in the timeframe provided. Similar to that observed in the water levels at WG4, the velocities (seen in Figure 5.17-b) do not show substantial deviation for the three still water depths considered. Although the changes induced to the waveforms were expected to have a visible impact on the timescales of the inundation depths and velocities, it is suspected that the secondary effects of harbour overflow (described previously) were dominant at this location. Thus, the general pattern in inundation characteristics at this location were not affected in a meaningful way by the still water depths considered here.

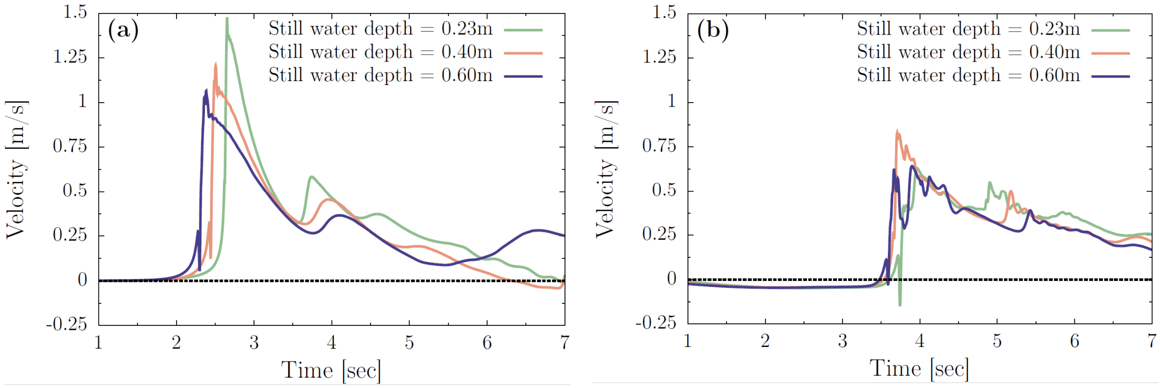

Figure 5.17: Influence of still water depth on time-histories of fluid velocity at (a) $x = 5.0$m and (b) $x = 6.15$m, 1.5cm above the basin floor.

6 Conclusions and Recommendations for Future Work

6.1 Conclusions

In this work, a numerical investigation of bore-structure interaction and pneumatic long wave generation was performed. The most important conclusions drawn from the extensive analysis are subdivided into the two major results sections and are summarized in the following.

6.1.1 Bore-Structure Interaction

- Chanson's (2009) analytical solution for a dam-break wave profile displayed good agreement with the computed profiles. Given the proper selection of the Darcy-Weisbach friction factor (f) for the friction-dominated wave tip, the depth, steepness and celerity of the surge front can be predicted with reasonable accuracy, particularly after the bore has become fully developed.
- For three-dimensional structures, the runup collapse force, caused by the weight of the initial runup (splash) collapsing down onto the incoming flow, appears to be significant at smaller scales but becomes increasingly less so as the model approaches full scale.
- The comparison of experimentally-measured and computed values for the impulsive load suggests that the compressibility of the air entrained in the leading edge of the wave during the physical tests did not have a significant influence on the magnitude of the load occurring at initial impact.
- The compressibility of the air did, however, have a large influence on the magnitude of the runup collapse force occurring at later stages. Since the numerical model treated the air as incompressible, the pocket of air trapped during the runup collapse produced a larger shock pressure (relative to the experiments) and therefore overestimated the resulting force, particularly for larger initial impoundment depths.
- It was observed that the peak hydrodynamic load occurs when water levels reach 90-95% of the maximum recorded inundation depth and when the velocities were approximately 55% of the maximum recorded value. This was consistent for all three initial impoundment depths considered.
- Drag force coefficients corresponding to peak hydrodynamic load for the three different initial impoundment depths ranged from 1.71-1.92 and, in general, showed a tendency to decrease with increasing initial impoundment depth. This suggests that the FEMA P646 (FEMA, 2012) recommended value of C_D = 2.0 may lead to overly-conservative predictions for the peak hydrodynamic load.
- The analytical formula to estimate the impulsive load given by FEMA P646 (FEMA, 2012) overestimated the corresponding computed values by approximately 2.5-4 times, depending on the initial impoundment depth (h_u). The overestimation was observed to be more extreme for the smaller bores.
- Small nonzero values for initial downstream depth significantly increased the depth of the bore front, extending the near-vertical face to greater heights. However, further increases in downstream depth did not appear to significantly influence bore front depth or steepness.

- Observed reduction in bore front celerity as a result of increasing initial downstream depths was not found to be as significant as suggested by other studies (*e.g.*, Leal et al., 2006 and St-Germain et al., 2012) for similar relative downstream depths (h_d/h_u). It is possible that the exchange of momentum between the bore and underlying layer was underestimated by the model.
- Increasing initial downstream depth (h_d) was shown to cause a more rapid closing of the wake behind the column. This reduced the differential pressure between the upstream and downstream side of structure, alleviating some of the net load, especially at the timing of peak hydrodynamic load.

6.1.2 Numerical modeling of Pneumatic Long Wave Generation

- Good agreement between the numerical and physical wave height and period was achieved by applying a hyperbolic tangent function to model the air pressure inside the tank.
- Although all three variants of the $k - \epsilon$ model showed promising results, the ReNormalized Group (RNG) $k - \epsilon$ was best suited to reproducing the finer details of the amplitude dispersion occurring in the primary wave.
- The agreement of the model results with the spatial and temporal variations of surface elevation and velocity show a high potential for the tool to be used to aid the design process of new similar devices or to provide support in analyzing the results of existing devices in greater detail.
- The analysis of the wave formation process showed that, for a short while, a high-velocity jet exiting the chamber builds a mound of water that becomes the leading wave. As it propagates away from the chamber, the jet can no longer continue to deliver water to the main wave. At this point, the wave begins to grow an elongated tail through the addition of water to its back end. Most likely owing to the large ratio between wave amplitude and still water depth, the leading wave was observed to separate into a primary and secondary wave. The latter was left behind in the elongated tail with a smaller amplitude and celerity than the former.
- For smaller outlet sizes, the amplitude of the initial wave was reduced and was accompanied with a corresponding reduction in the wave steepness. The profile of the trailing tails behind the initial wave was not significantly affected by the outlet size.
- The initial still water depth in the harbour or propagation section had remarkable influence on the wavelength of the initial wave. Although the wave crests arrive at the shore concurrently, the leading edge begins to inundate the coast at much earlier times for deeper still water depths. Furthermore, the shallower still water depths lead to more severe shoaling and as a result higher amplitude and steepness. Upon breaching the shore, the collapse of the higher waves lead to faster flow velocities especially close to the shore. Further from the shore, the velocities for each still water depth tended to converge to the same values.
- The deeper still water depths also cause the celerity of the reflected wave inside the basin to increase. Design of the experiments should take this into consideration so that the measurements of the phenomenon of interest can be taken before basin effects begin to have an influence

6.2 Recommendations for Future Work

Throughout this work, several aspects were identified that could be explored to help create a more comprehensive understanding of the broader issues presented in this thesis. The suggestions for future work are subdivided into the two major results sections presented in this thesis and are proposed as follows:

6.2.1 Bore-Structure Interaction

- In order to properly analyze the runup collapse force, a model that is capable of simulating compressible air should be considered.
- Establishment of the threshold at which the drag force coefficient (C_D) becomes independent from scaling effects.
- Investigations aimed at elucidating the influence of surrounding structures on local flow conditions and resulting forces. This would include both the concentration of wave energy through gaps or shielding provided by proximal structures. In addition, the effect of mitigation structures such as seawalls and dikes may be of interest.
- How various turbulence models (RAS, LES, DNS) affect interaction and momentum exchange between bores propagating over an initially still water layer. Capturing realistic shear and turbulence generated in the layer separating the bore and initially quiescent downstream layer is crucial to accurately simulating the effect it has on bore front characteristics (celerity, depth, steepness and air entrainment).

6.2.2 Numerical modeling of Pneumatic Long Wave Generation

- Investigating more complex hydraulic chamber pressure boundary conditions to generate target tsunami wave forms (e.g. trace signals gathered from field measurements) and to develop corresponding valve-opening time-series
- If the computational resources are available, performing a three-dimensional simulation with a large eddy model may better capture the turbulent behaviour involved, particularly near the mouth of the outlet during wave generation and also transformation process of the wave from deeper water to overland flow.
- By applying a numerical model capable of treating the air as a compressible media, it should be possible to model the valves at the top of the hydraulic chamber directly. This way, the pressure boundary condition would not have to be calibrated to specific experimental results.

References

[1] Al-Faesly, T., Palermo, D., Nistor, I. and Cornett, A. (2012). Experimental modeling of extreme hydrodynamic forces on structural models, International Journal of Protective Structures (IJPS), 3(4), 477-505.

[2] Allsop, W., Chandler, I., and Zaccaria, M. (2014). Improvements in the physical modelling of tsunamis and their effects. HR Wallingford Technical Report, Wallingford, UK.

[3] Allsop. W., Chandler, I., and Zaccaria, M. (2014). Improvements in the physical modelling of tsunamis and their effects. Techinal Report, HR Wallingford, Wallingford, UK.

[4] Ansys. (2015). Ansys ICEM – CFD meshing software. Available at: http://www.ansys.com/Products/Other+Products/ANSYS+ICEM+CFD.

[5] Árnason, H. (2005). Interactions between an incident bore and a free-standing coastal structure. Doctoral dissertation, Univ. of Washington, Seattle, WA.

[6] Berberović, E. (2010). Investigation of free-surface flow associated with drop impact: Numerical simulations and theoretical modeling. PhD Thesis, TU Darmstadt, Darmstadt, Germany.

[7] Brackbill, J.U., Kothe, D.B., and Zemach, C. (1992). A continuum method for modeling surface tension. Journal of Computational Physics, 100, 335-54.

[8] Briggs, M.J., Synolakis, C.E., Harkins, G.S. and Green, D.R. (1995). Laboratory experiments of tsunami runup on a circular island. Pure and Applied Geophysics, 144(3-4), 569-593.

[9] Bullock, G.N., Obhrai, C., Peregrine, D.H., and Bredmose, H. (2007). Violent breaking wave impacts, Part 1: Results from large-scale regular wave tests on vertical and sloping walls. Coastal Engineering, 54, 602-617.

[10] Chan, I. and Liu, P.L. (2012). On the runup of long waves on a plane beach. Journal of Geophysical Research, 117, 1-17.

[11] Chanson, H. (2006). Tsunami surges on dry coastal plains: application of dam break equations, Coastal Engineering Journal, Japanese Society of Civil Engineers (JSCE), 48(4), 355-370.

[12] Chanson, H. (2009). Application of the method of characteristics to the dam break wave problem. Journal of Hydraulic Research, 47 (1), 41-49.

[13] Charvet, I. (2012). Experimental modelling of long elevated and depression waves using a new pneumatic wave generator. PhD thesis, University College London, London, UK.

[14] Chinnarasri, C., Thanasisathit, N., Ruangrassamee, A., Weesakul, S. and Lukkunaprasit, P. (2013). The impact of tsunami-induced bores on buildings. Proceedings of the Institution of Civil Engineering (ICE), Maritime Engineering, 166, 14-24.

[15] Chock, G., Carden, L., Robertson, I., Olsen, M., and Yu, G. (2013). Tohoku tsunami-induced building failure analysis with implications for U.S. tsunami and seismic design codes. Earthquake Spectra, 29(1), 99-126.

[16] Choudhury, D. (1993). Introduction to the Renormalization Group Method and Turbulence Modeling. Fluent Inc., Technical Memorandum, TM-107.

[17] Cross, R.H. (1967). Tsunami Surge Forces. Journal of Waterways and Harbors Division, 93, 201-231.

[18] FEMA (2008). Design and construction guidance for breakaway walls. Technical bulletin 9, Washington, D.C., USA.

[19] FEMA P646. (2012). Guidelines for design of structures for vertical evacuation from tsunamis. Federal Emergency Management Agency, Washington, D.C.

[20] Ferziger, J.H. and Perić, M. (2002). Computational methods for fluid dynamics. Springer-Verlag, Berlin.

[21] George, W.K. (2013). Lectures in turbulence for the 21st century. Lecture notes, Imperial College, London, UK. Available at: http://www.turbulence-online.com/Publications/Lecture_Notes/Turbulence_Lille/TB_16January2013.pdf

[22] Ghobarah, A., Saatcioglu, M. and Nistor, I. (2006). The impact of the 26 December 2004 earthquake and tsunami on structures and infrastructure. Engineering Structures, 28 (2), 312-326.

[23] Goring, D.G. (1979). Tsunamis – the Propagation of Long Waves Onto a Shelf. Ph.D. thesis, California Institute of Technology, Pasadena, California.

[24] Goseberg, N., Wurpts, A. and Schlurmass, T., (2013). Laboratory-scale generation of tsunami and long waves. Coastal Engineering, 79, 57-74.

[25] Hagen, M. (2014). Detailed Analysis of the 2011 Japan Tsunami – Video Footage, Wave Heights and Damage Imagery. Available at: www.extremeplanet.me.

[26] Hammack, J.L. (1973). A note on tsunamis: their generation and propagation in an ocean of uniform depth. Journal of Fluid Mechanics, 60(4), 769-799.

[27] Heitner, K. and Housner, G. (1970) Numerical model for tsunami run-up. Journal of Waterways and Harbors Coastal Engineering Division, 93(3), 701-719.

[28] Higuera, P., Lara, J.L., and Losada, I.J. (2013). Realistic wave generation and active wave absorption for Navier-Stokes models application to OpenFOAM. Coastal Engineering, 71, 102-118.

[29] Issa, R.I. (1986). Solution of the implicitly discretised fluid flow equations by operator-splitting. Journal of Computational Physics, 62, 40–65.

[30] Jasak, H. (1996). Error analysis and estimation for the finite volume method with applications to fluid flows. PhD thesis, Imperial College, London, UK.

[31] Kitware. (2015). ParaView – Open source dataset analysis and visualization software. Available at: http://www.paraview.org/.

[32] Lauber, G. and Hager, W. H. (1998). Experiments to dam-break wave: horizontal channel. Journal of Hydraulic Research, 36(3), 291-307.

[33] Launder, B.E. and Spalding, D.B. (1974). The numerical computation of turbulent flows. Computer Methods in Applied Mechanics and Engineering, 3(2), 269–289.

[34] Linton, D., Gupta, R., Cox, D., Lindt, J., Oshnack, M. and Clauson, M. (2013). Evaluation of tsunami loads on wood-frame walls at full scale. J. Structural Engineering, 139 (8), 1318-1325.

[35] Lukkunaprasit, P., Thanasisathit, N. and Yeh, H. (2009). Experimental verification of FEMA P646 tsunami loading. Journal of Disaster Research, 4(6), 410-418.

[36] Madsen, P.A., Fuhrman, D.R. and Schäffer H.A. (2008). On the solitary wave paradigm for tsunamis. Journal of Geophysical Research, 113(12), 1-22.

[37] Meier, M., Yadigaroglu, G., and Smith, B.L. (2002). A novel technique for including surface tension in PLIC-VOF methods. European Journal of Mechanics B/Fluids, 21, 61-73.

[38] Menter, F. R. (1994). Two-equation eddy-viscosity turbulence models for engineering applications. AIAA Journal 32(8), 1598-1605.

[39] Munk, W.H. (1949). The Solitary Wave Theory and Its Application to Surf Problems. Annals of the NewYork Academy of Sciences 51, 376–424.

[40] Nistor, I., Palermo, D., Nouri, Y., Murty, T. and Saatcioglu, M. (2009). Tsunami forces on structures. In Kim, Y. C., Handbook of Coastal and Ocean Engineering, World Scientific, pp. 261-286.

[41] Nouri, Y., Nistor, I. and Palermo, D. (2010). Experimental investigation of tsunami impact on free standing structures, Coastal Engineering Journal, JSCE, 52(1), 43-70.

[42] Open Cascade. (2015). Salome – The open source integration platform for numerical simulations. Available at: http://www.salome-platform.org/.

[43] OpenCFD Ltd. (2015a). OpenFOAM User Guide, v. 2.4.0. OpenFOAM Foundation Ltd., Available at: http://foam.sourceforge.net/docs/Guides-a4/UserGuide.pdf.

[44] OpenCFD Ltd. (2015b). OpenFOAM Programmer's Guide, v. 2.4.0. OpenFOAM Foundation Ltd., Available at: http://foam.sourceforge.net/docs/Guides-a4/ProgrammersGuide.pdf

[45] Paczkowski, K., Riggs, R.H., and Robertson, I.N. (2011). Bore impact upon vertical and water-driven, high-mass, low-velocity debris impact. Research report UHM/CEE/11-05, University of Hawaii, Manoa, Hawaii.

[46] Peregrine, D.H. (2003). Water-wave impact on walls. Annu. Rev. Fluid Mech., 35, 23-43.

[47] Pucket, E.G., Almgren, A.S., Bell, J.B., Marcus, D.L., and Rider, W.J. (1997). A high-order projection method for tracking fluid interfaces in variable density incompressible flows. Journal of Computational Physics, 130, 269–282.

[48] Ramsden, J.D. (1993). Tsunamis: forces on a vertical wall caused by long waves, bores, and surges on a dry bed. Ph.D. thesis, California Institute of Technology, Pasadena, California.

[49] Ramsden, J.D. (1993). Tsunamis: Forces on a vertical wall caused by long waves, bores, and surges on a dry bed. Doctoral dissertation, California Institute of Technology, Pasadena, CA.

[50] Renardy, Y. and Renardy, M. (2002). PROST: A parabolic reconstruction of surface tension for the volume-of-fluid method. Journal of Computational Physics, 183, 400–421.

[51] Ritter, A. (1892). Die fortpflanzung der wasserwellen, Vereine Deutscher Ingenieure Zeitswchrift, 36(2), 947-954 (in German).

[52] Robertson, I.N., Riggs, H.R., Paczkowski, K. and Mohamed, A. (2011). Tsunami bore forces on walls. 30th International Conference on Ocean, Offshore and Arctic Engineering, Rotterdam, the Netherlands, June 19-24, 2011.

[53] Rossetto, T., Allsop, W., Charvet, I., and Robinson, D.I. (2011). Physical modelling a tsunami using a new pneumatic wave generator. Coastal Engineering, 58, 517-527.

[54] Rusche, H. (2002). Computational fluid dynamics of dispersed two-phase flows at high phase fractions. PhD thesis, Imperial College, London, UK.

[55] Sarmento, A.J.N.A. and Falcão, A.F.O. (1985). Wave generation by an oscillating surface-pressure and its application in wave-energy extraction. Journal of Fluid Mechanics, 150, 467–485.

[56] Scardovelli, R. and Zaleski, S. (1999). Direct numerical simulation of free-surface and interfacial flow. Annual Review of Fluid Mechanics, 31, 567-603.

[57] Shen, M. C., and Meyer, R.E. (1963). Climb of a Bore on a Beach Part 3: Run-up. Journal Fluid Mechanics, 16, 113-125.

[58] Shih, T.H., Liou, W.W., Shabbir, A., Yang, Z., and J. Zhu. (1995). A new $k - \epsilon$ eddy-viscosity model for high Reynolds number turbulent flows - Model development and validation. Computers Fluids, 24(3), 227-238.

[59] Stansby, P. K., Chegini, A. and Barnes, T. C. D. (1998). The initial stages of dambreak flow. Journal of Fluid Mechanics, 374, 407-242.

[60] Stansby, P.K., Chegini, A. and Barnes, T.C.D. (1998). The initial stages of dam-break flow. Journal of Fluid Mechanics, 374, 407-424.

[61] St-Germain P, Nistor I, Townsend R (2012) Numerical modeling of the impact with structures of tsunami bores propagating on dry and beds using the SPH method. International Journal of Protective Structures 3(2), 221–255.

[62] St-Germain P., Nistor I., and Townsend R. (2012). Numerical modeling of the impact with structures of tsunami bores propagating on dry and beds using the SPH method. International Journal of Protective Structures, 3(2), 221–255.

[63] St-Germain, P. (2012). Numerical modeling of tsunami-induced hydrodynamic forces on free-standing structures using the SPH method. M.A.Sc. thesis, University of Ottawa, Ottawa, Canada.

[64] St-Germain, P., Nistor, I., Townsend, R., and Shibayama, T. (2014). Smoothed particle hydrodynamics numerical modeling of structures impacted by tsunami bores. J. Waterway, Port, Coastal, Ocean Eng., 140 (1), 66-81.

[65] Stolle J., Nistor I., Goseberg N., Matsuba S., Nakamura R., Mikami T., and Shibayama T. (2015). Flood-induced debris dynamics over a horizontal apron. Coastal Structures, Boston, USA, September 9 – 11, 2015.

[66] Synolakis, C. E. (1987). The runup of solitary waves. Journal of Fluid Mechanics, 185, 523–545.

[67] Takahashi, R. and Hatori, T. (1962). A model experiment on the tsunami generation from a bottom deformation area of elliptic shape. Bulletin Earthquake Research Institute, Tokyo University, 40, 873-883.

[68] Takahashi, S., Kuriyama, Y., Tomita, T., Kawai, Y., Arikawa, T., Tatsumi, D. and Negi, T. (2011). Urgent survey for 2011 Great East Japan Earthquake and Tsunami disaster in ports and coasts – part I (tsunami). English abstract of the technical note of the Port and Airport Research Institute (PARI), No. 1231, 9 pp.

[69] Tonkin, S., Yeh, H., Kato, F. and Sato, S. (2003). Tsunami scour around a cylinder. Journal of Fluid Mechanics, 496, 165-192.

[70] Ubbink, O. (1997). Numerical prediction of two fluid systems with sharp interfaces. PhD thesis, Imperial College, London, UK.

[71] Ubbink, O. and Issa, R.I. (1999). A method for capturing fluid interfaces on arbitrary meshes. Journal of Computational Physics, 153(1), 26-50.

[72] Weller, H.G. (2008). A new approach to VOF-based interface capturing methods for incompressible and compressible flow. Technical Report TR/HGW/04, OpenCFD Ltd., 2008.

[73] Wilcox, D.C. (1988). Re-assessment of the scale-determining equation for advanced turbulence models. AIAA Journal, 26(11), 1299-1310.

[74] Wilkie, M.J. and Young, G.A. (1952). Pneumatic tide generator. The Engineer, July 1952.

[75] Yakhot, V., Orszag, S.A., Thangam, S., Gatski, T.B. and Speziale, C.G. (1991). Development of turbulence models for shear flows by a double expansion technique. Physics of Fluids A, 4(7), 1510-1520.

[76] Yeh, H. (2006). Maximum Fluid Forces in the Tsunami Runup Zone. Journal of Waterway, Port, Coastal, and Ocean Engineering, 132(6), 496-500.

[77] Yeh, H. (2007). Design tsunami forces for onshore structures. Journal of Disaster Research, 2(6), 531-536.

[78] Yeh, H., Sato, S. and Tajima, Y. (2013). The 11 March 2011 East Japan Earthquake and Tsunami: Tsunami effects on coastal infrastructure and buildings. Pure and Applied Geophysics, 170, 1019-1031.